Material Characterization and Modification using Helium Ion Microscopy: Various Examples

Vasilisa Veligura • University of Twente • 2014

Material Characterization and Modification using Helium Ion Microscopy: Various Examples

Vasilisa Veligura

Committee members:

Chairman and secretary:
Prof. Dr. Ir. J.W.M Hilgenkamp   University of Twente

Promotor:
Prof. Dr. Ir. B. Poelsema   University of Twente

Assistant promotors:
Dr. G. Hlawacek   University of Twente
Dr. R. van Gastel   University of Twente

Members:
Prof. Dr. A. Gölzhäuser   Universität Bielefeld
Prof. Dr. Ir. P. Kruit   Delft University of Technology
Prof. Dr. F. Bijkerk   University of Twente
Prof. Dr. Ir. H.J.W. Zandvliet   University of Twente

MATERIAL CHARACTERIZATION AND MODIFICATION USING HELIUM ION MICROSCOPY: VARIOUS EXAMPLES

DISSERTATION

to obtain
the degree of doctor at the University of Twente,
on the authority of the rector magnificus,
Prof. Dr. H. Brinksma,
on account of the decision of the graduation
committee, to be publicly defended
on Friday 21 March 2014 at 14:45 hrs

by

Vasilisa Veligura
born on 18 June 1987
in Uralsk, Soviet Union

This dissertation has been approved by:

Promotor: Prof. Dr. Ir. B. Poelsema
Supervisors: Dr. G. Hlawacek
            Dr. R. van Gastel

Contents

1 Introduction

1.1 The path to Helium Ion Microscopy invention

A variety of microscopy techniques is used on a daily basis in science and industry for material visualization and characterization. Microscopy has been developing over centuries and nowadays has branched into several sub-fields such as optical, scanning probe, digital holographic, and charged particle beam microscopies [1, 2]. Microscopy resolution capabilities significantly improved after the idea of the dual character of an electron was formulated by Louis de Broglie in 1924. Already in 1927 the electron wave behavior was experimentally proven independently by C. D. Davisson and L. H. Germer as well as G. P. Thomson. Shortly thereafter, a first electron microscope was invented by M. Knoll and E. Ruska in 1931 [3]. In 1933 the resolution in the electron microscope exceeded the ultimate resolution of an optical microscope at that time.

The creation of a field-ion microscope (FIM) by E. W. Müller in 1951 was another breakthrough in microscopy [4, 5]. In FIM a sharp metal tip is held at a high positive voltage. The electric field at the apex is enhanced at the most protruding atoms and effectively ionizes surrounding noble gas. The noble gas ions are accelerated towards a phosphor-screen forming there an image of the tip. FIM allowed the visualization of individual atoms for the first time in human history. Based on Müller's idea applied in FIM, numerous studies were performed on the creation of a stable gas field ion source (GFIS), improvement of its performance [6–9], and on its application in microscopy [10–13]. The idea of the ion microscope was proposed by M. Knoll and E. Ruska already in 1932 [3], however, it has not been realized for a long time due to technical limitations. The development of electrostatic lenses [14] and the invention of a stable

GFIS with a high brightness and small virtual source size by B. Ward and co-workers enabled the establishment of helium ion microscopy (HIM) in 2006 [15]. HIM was quickly recognized as an outstanding microscopy technique mainly due to its sub-nanometer resolution [16].

1.2 Motivation

From the very beginning HIM has proven itself to be a powerful imaging tool. However, so far HIM lacks useful analytical techniques. The goal of our research was to explore a possibility to use HIM not only for visualization, but also as an analytical technique. One of the applications we investigated was the acquisition of crystallographic information in-situ in the HIM. Electron channeling is a well-known mechanism to obtain grain contrast in scanning electron microscopy (SEM) [17]. The contrast originates from the dependence of the backscatter electron yield on the mutual orientation of the beam and a crystalline sample. The electron backscatter diffraction (EBSD) technique provides full information about grain orientation and is often used in material science and geology [17,18]. Ion channeling can also be used to obtain grain contrast which is often done in focused ion beam (FIB) microscopy [19,20]. Ion channeling contrast can be observed in both secondary electron (SE) and backscattered ion images. In this work we will demonstrate channeling contrast in HIM and a way to use it for crystal orientation mapping.

Soon after the invention of the electron microscope it was also realized that intense charged particle beams can modify a sample [21]. The authors observed the appearance of a carbon film on the sample surface, which points towards the importance of proper vacuum conditions in the sample chamber. Normally undesired effects of sample modification during measurements can be used advantageously for several applications. For example, electron beams are widely applied for lithography [22], while intensive ion beams in FIB are effectively used for micro- and submicrometer-machining or even for material deposition [23]. FIB usually operates with heavy Ga^+ ions which makes FIB imaging damaging, but effective for massive material removal. A He^+ ion beam is expected to be less destructive, however, imaging with HIM is not completely damage free. In this work we are interested in the influence of a He^+ beam on various samples and the physics of the processes occurring during ion irradiation. The extremely small size of the beam in HIM pro-

vides a unique opportunity to look at fundamental ion-matter interaction processes on the nanoscale.

For the investigation of defect formation processes we apply the iono-luminescence (IL) technique. Similar to cathodoluminescence in SEM where light emission from a sample is generated by the electron beam, certain materials emit visible light under ion irradiation [24, 25]. This signal can provide information on both intrinsic or defect related electronic states of a sample. Contrary to SE imaging, the IL signal provides information not only from the surface, but also the bulk.

1.3 Outline of the thesis

The experimental setup and working principles of HIM are described in details in Chapter 2. Chapter 3 is dedicated to the application of the ion channeling phenomenon for acquiring crystallographic information of a sample in HIM. As a sample a {111} textured polycrystalline gold film was used. We describe and apply a simple geometrical model for the identification of the grain orientation. An advantage of using grain contrast in SE over backscattered helium (BSHe) images is also discussed. In addition, an unexpected contrast in BSHe images of light layers on a heavier crystalline substrate is demonstrated and explained in terms of de-channeling in this chapter.

The modification of several samples under He^+ irradiation was investigated in this work. Beam induced changes of a metal surface were studied using a thin gold film. In Chapter 4 we show and discuss the changes of the surface morphology as a function of the beam energy and fluence.

Studies of defect creation in sodium chloride are presented in Chapters 5 and 6. Under the influence of ionizing radiation color-centers are formed in ionic crystals. In Chapter 5 we study how pixel spacing and beam current influence the balance between different types of crystal defects and, therefore, the IL signal intensity. The generation of color-centers with a sub-nanometer He^+ beam allows patterning of luminescent features with a very high precision, which is shown in Chapter 6. In addition, we use patterning for direct IL measurements of the lateral size of the interaction volume of a sub-nanometer He^+ beam with NaCl. Moreover, Monte Carlo simulations were performed for the estimation of the defect concentration needed to create a measurable IL signal.

Finally, in Chapter 7 we discuss the influence of ion irradiation on the luminescence of semiconductor samples. We have examined various semiconductor materials of different geometries: bulk samples, nanowires and quantum dots. We discuss the origin of the observed IL signal and difference in its quenching by the ion beam as a function of the sample's composition and dimensions.

2 Experimental

The experimental details are introduced in this chapter. The experiments were performed with an ultra high vacuum Orion Plus Helium Ion Microscope from Carl Zeiss NTS. It is a modern and powerful tool which provides a sub-nanometer He$^+$ ion beam for sample investigations. Here we introduce the working principle of the helium ion microscope and discuss the nature of the main signals obtained and used in the microscope. We also describe the modifications introduced to a standard system in order to improve its vacuum performance.
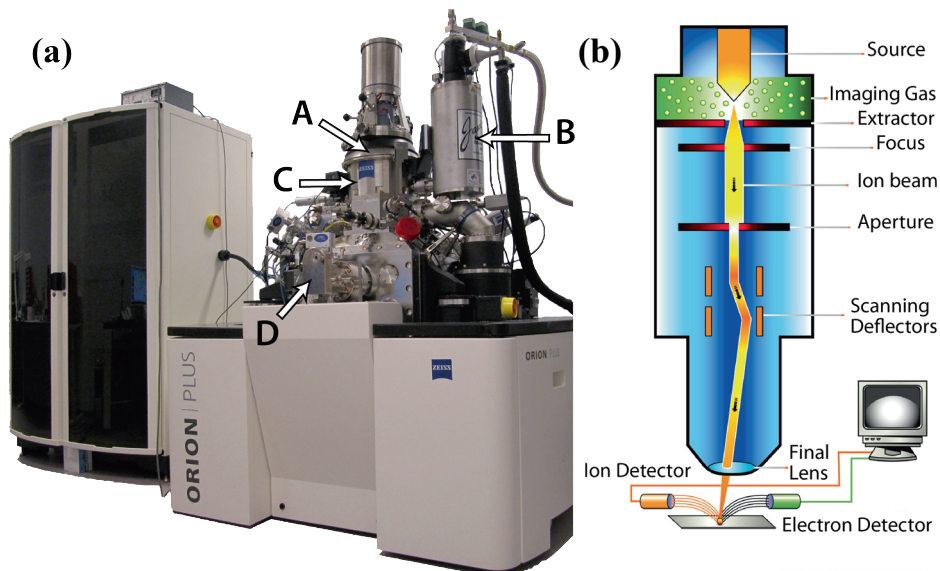
Figure 2.1: (a) Picture of the UHV HIM. The control electronic racks are in the left half. The modified HIM is in the right half of the picture. The ion source (A) is located at the top of the column and is cooled down by solid nitrogen in the dewar (B). The ion beam goes down through the optical column (C) into the main chamber. Samples are introduced into the main chamber through the custom made load lock (D). All three vacuum chambers of the instrument – the source, the ion optics, and the main chamber – have a vacuum pressure in the UHV range. (b) A schematic drawing of the system. The image is taken from Ref. [26].

2.1 Helium Ion Microscopy

The experiments presented in this work were performed with an ultra high vacuum (UHV) Orion Plus Helium Ion Microscope from Carl Zeiss NTS. Helium ion microscopy (HIM) is a modern technique for material characterization and modification which was introduced in 2006 [15]. HIM provides high-resolution imaging capabilities in combination with an extreme surface sensitivity. As opposed to the commonly used scanning electron microscope (SEM), imaging here is based on the interaction of a He^+ ion beam, rather than an electron beam, with a target.

A standard HIM operates using high vacuum (HV) conditions in the main chamber. Several changes were made to the system in order to improve the vacuum conditions. We will discuss them in detail, and the
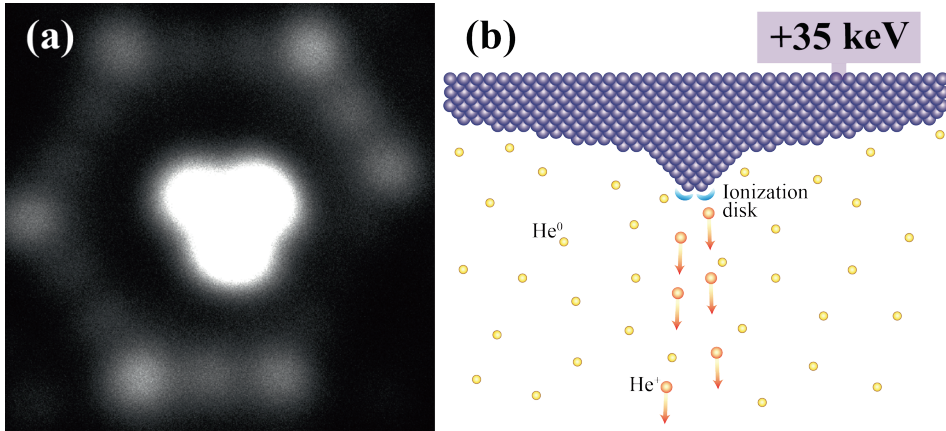
Figure 2.2: (a) Actual SFIM image of a source. The center trimer and the edges and corners of the next crystal plane are visible. (b) Sketch of the GFIS. Ionization predominantly happens at the apex of the tip.

motivation later in this chapter. The modified UHV system is shown in Fig. 2.1(a). A schematic drawing of a HIM is shown in Figure 2.1(b). An ion beam is accelerated from the source and travels down through the optical column towards the sample. HIM is a scanning technique. Scanning deflectors steer the ion beam and raster the sample. Several detectors are used to record the produced signals. In this chapter we describe the operation of the HIM, starting from the beam formation, to the detection of the generated signals.

2.2 Source and interaction volume

The main characteristic feature of the HIM is its Gas Field Ion Source (GFIS). It is an atomically sharp tip, which is held at high positive voltage and liquid nitrogen temperature in the presence of He gas [15]. A so-called "trimer" – a stable configuration of three atoms – is formed at the apex of the tip using high electric fields. A scanning field ion microscopy (SFIM) image of the source is shown in Fig. 2.2(a). The surrounding helium gas is ionized in the electric field at the tip. This process is most effective in the vicinity of the trimer atoms where the electric field is the strongest. A sketch of the ion source can be found in Fig. 2.2(b). An aperture can be placed in the beam path to restrict the emission current to one of the three atoms. Additionally, the short

Virtual source size	$\leq 0.25\,\text{nm}$	estimated
Angular intensity	$0.5\text{--}1\,\mu\text{A}\,\text{sr}^{-1}$	measured
Brightness	$\approx 1 \times 10^9 \text{A}\,\text{cm}^{-2}\text{sr}^{-1}$	calculated
Energy spread	$0.25\,\text{eV}\text{--}0.5\,\text{eV}$ [27]	measured

Table 2.1: Typical helium ion sources parameters [16]

De Broglie wavelength of the helium ions leads to a reduction of the influence of diffraction effects. Thus, the He$^+$ beam can be projected on the sample into a sub-nanometer size spot [26].

The ion beam energy can be varied between $10\,\text{keV}$ and $40\,\text{keV}$. The typical source parameters are listed in Table 2.1. The energy spread of $1\,\text{eV}$ is an upper boundary. Earlier measurements indicate that the values could in fact be lower by a factor 2 to 4 [27]. One of the important consequences of the parameters listed in Table 2.1 is the beam convergence angle α_i. Typical values for α_i are well below $1\,\text{mrad}$. This small beam divergence results in a large depth of field

$$d_f = \frac{\delta}{\alpha_i}. \tag{2.1}$$

Here, δ denotes the minimal feature size that can be resolved in the image. Assuming identical resolutions, the HIM will have a superior depth of field as compared to low voltage SEM with typical α_i values of $8\,\text{mrad}$ [28].

While traveling through matter, helium particles undergo a series of elastic and inelastic collisions with the target electrons and nuclei. A collision with an electron hardly changes the direction of the helium due to their mass difference. The nuclear collisions laterally scatter the beam. However, scattering with target atoms becomes considerable only after the helium particles have significantly slowed down, deeper in the material. As a result, in the vicinity of the surface the beam preserves its nanosized and collimated shape and the interaction volume remains extremely small [15].

8

2.3 Signals

As a result of the He$^+$ beam interaction with a sample, secondary electrons, backscattered helium and, in some cases, photons are generated. Below we discuss the signals available in HIM.

2.3.1 Secondary electrons

In HIM secondary electrons (SE) emitted from the sample can have into two origins: SEs generated directly by the incident He – SE1, and SE2 – the SEs produced by the secondary particles (by SE1 and recoil target atoms). As has been proposed by Bethe [29], the rate of SE generation δ_{SE} (electrons per incoming ion) is proportional to the stopping power of the incident particle $\frac{\mathrm{d}E}{\mathrm{d}s}$ in eV/Å

$$\delta_{SE} = -\frac{1}{\epsilon}\frac{\mathrm{d}E}{\mathrm{d}s} \tag{2.2}$$

where ϵ denotes a scaling constant. It is assumed that at least in the relevant near-surface region atomic collisions do not play an important role and $\frac{\mathrm{d}E}{\mathrm{d}s}$ depends only on the electronic stopping power.

   The generation of the SE1 mainly occurs via kinetic emission (KE) [30] through direct collisions of the incoming ions with outer shell electrons. The other process for the electron generation is potential emission (PE) via Auger neutralization. In this process a positive incident ion gets neutralized via electron tunneling. The released energy is transferred to another electron, which later can be emitted. However, PE becomes a dominant process only for low ion energies below 5 keV [31]

   SE2 generation does not play an important role in HIM. This becomes clear when looking at the maximum energy of the SE1 which is taken equal to the energy loss of the impinging helium for a head-on collision [30]

$$\Delta E = 2m_e \left(v + (v_F/2)\right)^2. \tag{2.3}$$

Here, m_e is the electron mass, v the ion velocity, and v_F denotes the Fermi-velocity. The cross section for such a collision is the highest if the ion velocity ($v \approx 1.3 \times 10^6$ m/s in the case of 35 keV ions) matches the Fermi-velocity of the electrons in the material. For gold and 35 keV He this yields a maximum SE1 energy of 45 eV. However, this energy is approximately equal to or even below the effective energy needed for

secondary electron generation by electrons in many materials [32]. Thus, the size of the electron collision cascade is restricted. Additionally, recoil atoms will contribute to KE when they are fast enough and their speed matches the Fermi-velocity of the target material.

Once electrons have been generated, they still need to escape from the solid. As originally suggested by Salow [33] this process can be described as a diffusion process. The effective diffusion length of SE is of the order of 1 nm for nearly all materials [31]. This means that only the first few nanometers of material play a role for the achievable SE yield. As a result the probe volume is extremely small – it is a cylinder with a diameter of approximately 0.5 nm and length of a few nm. Finally, to be emitted the electrons also have to have a sufficiently high energy to emerge from the sample into the vacuum. Measurements of the SE yield in HIM show variations between 1 – for carbon – and up to 8 electrons per ion – for platinum [34].

Formation of the topography contrast in HIM is similar to that in SEM. The following secans law usually describes the dependence of the SE yield on the specimen tilt with respect to the incoming beam:

$$\delta_{SE}(\theta) = \delta_{SE}(0) \sec \theta. \tag{2.4}$$

However, experimental studies showed that the actual measured SE yield at the detector deviates from the expected secant behaviour [35]. The deviations lead to a more linear response curve which in turn should reduce the strong edge effect known from SEM. Nevertheless, a very strong edge effect has been observed in thin layers [36, 37].

2.3.2 Backscattered helium

HIM allows the acquisition of qualitative element distribution maps by collecting the backscattered helium. The majority of the helium which leaves the sample is in the neutralized state [38]. Therefore, we refer to the backscattering signal as backscattered helium (BSHe), without specifying the helium's charge state. The BSHe signal contains composition information, but provides a poor topographic contrast compared to SE

images [39]. The contrast obtained in BSHe images can be understood by examining the scattering cross-section

$$d\sigma = \left(\frac{e^2 Z_1 Z_2}{4E_0}\right)^2 \frac{d\Omega}{\sin^4 \frac{\theta}{2}}, \tag{2.5}$$

where e is the elementary charge, and Z_1 and Z_2 denote the atomic number of impinging and target particles respectively, E_0 is the energy of the impinging particle, $d\Omega$ is an arbitrary element of solid angle, and θ is the scattering angle. The target atom is assumed to be at rest. Thus, at fixed Z_1 (incident helium ions) and energy, the backscattering probability increases with increase of the mass of the target atom, and scales with the atomic number as Z_2^2. A more detailed analysis of the scattering cross-section reveals a dependence on the structure of the periodic table of elements. This is related to the change in screening along the rows of the periodic table. In contrast to the previously described SE signal, BSHe represents a bulk signal. Depending on the target material and the energy of the He ions, the probing depth can vary from a few tens up to a few hundreds of nm. Lowering the ion energy increases the backscatter efficiency. However, it also decreases the beam penetration depth.

2.3.3 Photons

Generally speaking, ionoluminescence (IL) is the phenomenon of light emission due to the optical transitions of an electronic system which has been excited by an ion beam. Three main stages can be distinguished in the luminescence process [40]:

1. energy absorption and excitation of the electronic system;
2. system relaxation and energy transfer to the emission centers;
3. transition of the system into the ground state by photon emission.

During sample bombardment with He^+ ions, light can be obtained from the excited backscattered neutral He [41, 42], excited sputtered atoms and molecular complexes [24, 43, 44], or from the material itself [24, 45]. For the case where emission originates from the species, that have left the sample in an excited state, the spectrum consists of discrete Doppler-broadened lines. These lines correspond to the optical transitions within atomic (or molecular) orbitals. This light is usually observed at a distance of up to a few millimeters from the target surface [24]. Since in our

experiments the detector focus is at the sample surface, we do not expect to detect any signal from the sputtered species or from the neutralized helium.

For the investigation of materials properties we are mainly interested in the luminescence from the solid itself. The physics of the emission processes is usually described by considering the sample's electronic band structure or by using configuration coordinate diagrams [40]. According to its origin, there are two general types of luminescence: *extrinsic* and *intrinsic* [46]. In the case of extrinsic luminescence, the light generation is related to the presence of impurity atoms or ions (so-called *activators*) in the sample material.

Intrinsic luminescence on the other hand, is emission from the sample material itself. Here, two cases can be distinguished. First, optical transitions from delocalized states: the recombination of free electrons from the conduction band with holes in the valence band. This includes direct and indirect transitions. Additionally, the radiative recombination of free excitons also falls in this category. Second, optical transitions from localized states can be attributed to intrinsic luminescence as well. This includes the following processes: recombination of excitons trapped at the defect sites (so-called self-trapped excitons [47]); emission from the excited defects – known as color-centers (e.g. nitrogen-vacancy centers in diamond [48]); and transitions of charge carriers from delocalized into localized states. The shape and width of the emission peaks and bands strongly depend on electron-phonon interaction and thermal effects. A strong electron-phonon interaction leads to a Stokes shift and peak broadening. As a result, it is desirable to perform ionoluminescence measurements at cryogenic temperatures, which has not been done to date in HIM.

Since IL is in many aspects similar to the cathodoluminescence (CL) phenomenon often observed in SEM, databases of CL studies can be employed for the interpretation of IL spectra. However, ionoluminescence studies are significantly complicated by the fact that an ion beam not only induces light emission, but also directly influences the luminescence properties of the target due to defect creation [49,50]. Ion irradiation can lead to target coloration (e.g. in ionic crystals [Chapters 5 and 6]), as well as quench the luminescence (e.g. semiconductor materials [Chapter 7])
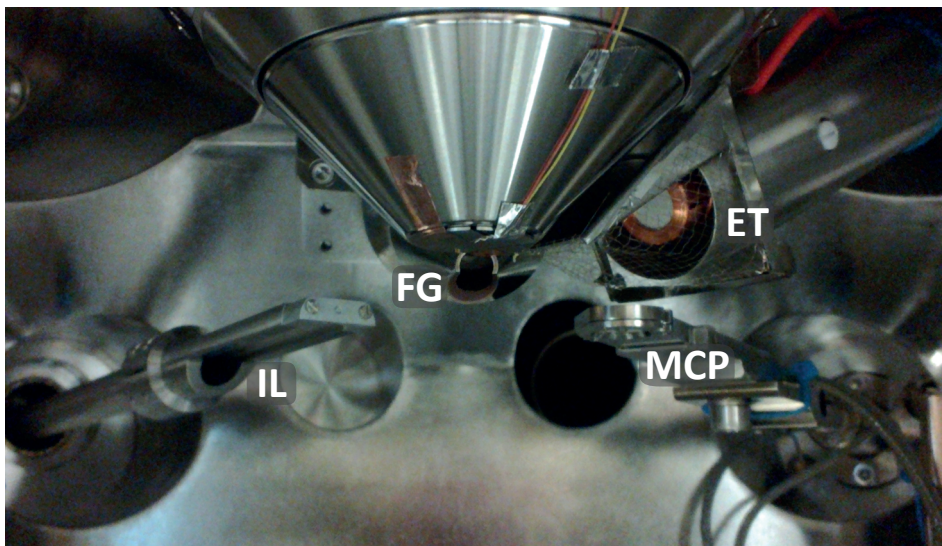
Figure 2.3: A picture of the detectors inside of the UHV chamber. IL – parabolic mirror of the ionoluminescence system, FG – electron flood gun for surface charge compensation, MCP – microchannel plate for collection of BSHe, ET – Everhart-Thornley detector for collection of SEs.

2.4 Detectors

The detectors inside of the main chapter are shown in the picture in Fig. 2.3. In the standard imaging mode in HIM an image is acquired by collecting SEs using an Everhart-Thornley (ET) detector [51]. SEs emission and neutralization of the positive helium ions with material electrons lead to a positive surface charging of insulating materials. This charge can be neutralized with low energy electrons. For imaging of insulating samples the ET detector can be used in an interleaving way with an electron flood gun [39]. Thus, no conductive coating is required for the imaging of insulating samples. The charge compensation is synchronized with the ion beam scanning, allowing neutralization in a frame by frame or line by line manner.

A microchannel plate (MCP) is used for recording BSHe images [52]. The MCP can be inserted between the sample and the objective lens in the primary beam path. A hole in the center of the detector allows the ion beam to reach the sample. This configuration maximizes the solid angle and consequently the collection efficiency of the detector.
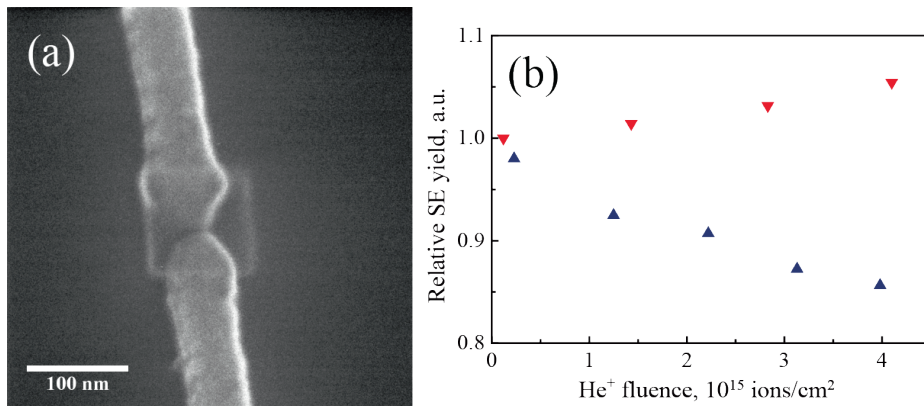
Figure 2.4: (a) HIM SE image of Au electrodes with a few nm gap. The square in the center of the images is caused by the carbon deposition during the high-resolution imaging with the He^+ beam. FOV is $2\,\mu m$, He^+ beam primary energy is $28.5\,keV$. (b) Change of SE yield with He^+ ion fluence in case of UHV (▼), and non-UHV (▲) chambers.

For an IL image, the emitted photons are detected with a Gatan MonoCL4 Elite system. A retractable parabolic mirror is used for the collection of the light emitted from a sample. The mirror can be placed between the objective lens and the sample. An aperture in the mirror allows the focused He^+ to pass through and scan the sample. The collected light is then directed by a light guide into a spectrometer. A panchromatic IL image is recorded by collecting the signal with a Hamamatsu Photomultiplier Tube (PMT) R943-02, with a spectral response of 160–930 nm. A CCD detector PIXIS:100 from Princeton Instruments can be used for a parallel spectrum acquisition. For this purpose the emitted light is sent through slits onto a diffraction grating. Then the angularly-distributed spectrum is projected on the CCD. A spectrum can be acquired in the 200–1100nm wavelength range.

2.5 Ultra High Vacuum

A focused ion beam may very effectively decompose or cross-link residual hydrocarbons present in the instrument vacuum or at the sample surface. Figure 2.4(a) shows a SE image of two Au electrodes with a gap of a few nanometers, after a high-resolution image of the gap was taken. A carbon layer was deposited in the previously scanned area, changing the

contrast and sample topography. A number of changes were introduced to the standard Orion Plus setup to improve the vacuum performance of the machine [53].

The majority of the modifications were made to the sample chamber. Nickel plated steel has been replaced by stainless steel as the chamber material to achieve the best possible vacuum conditions. All non-UHV compatible materials and low vapor pressure lubricants inside of the chamber were replaced by UHV compatible ones. All seals are implemented using conflat style flanges with Cu gaskets. The pumping speed was increased by an additional $5000\,l/s$ using a Ti sublimation pump at back of the main chamber. In addition, halogen lamp heaters were placed inside the chamber to allow a simple bakeout of the main chamber. The standard load-lock has been replaced. A small volume, turbo pumped load-lock chamber was designed and built. A magnetic pushrod used for inserting the sample into the main chamber acts as the seal of the load-lock during the sample transfer and is replaced with a simple blank-off plate while measuring. The last step is necessary to minimize vibrations otherwise coupled into the system via the pushrod.

All the modifications allow the pressure to be kept in the $10^{-10}\,$mbar range during HIM measurements. The effect of the vacuum conditions on SE yield with increasing He^+ fluence is presented in Fig. 2.4(b). A plasma cleaned polycrystalline Au film was exposed to the He^+ beam in non-UHV and UHV setups. All relevant imaging parameters were identical and kept constant during the measurements. In the case of the non-UHV machine, the signal decreases with ion fluence as a result carbon deposition, whereas the SE yield slightly increases in the case of the UHV chamber due to an increase in surface roughness.

3

Channeling in HIM

As in other techniques that make use of a charged particle beam, channeling through of the bulk of a crystalline material can occur in helium ion microscopy (HIM) as well. Here, we demonstrate how this bulk phenomenon affects secondary electron (SE) images that predominantly contain surface information. We will discuss the origin of the channeling contrast observed in SE images, illustrate this with experiments and develop a simple geometric model to predict channeling maxima. Secondary electron images can further be used to extract crystallographic information from bulk samples as well as thin surface layers in a straightforward manner. Channeling also allows visualization of ultra thin organic layers on heavier element substrates with backscattered He particles (BSHe). Suppression of ion channeling into crystalline matter by adsorbed thin films leads to the unanticipated contrast appearance in BSHe images. That phenomenon further highlights the importance of proper vacuum conditions for channeling based experimental methods.

3.1 Introduction

Information on the crystalline texture of a sample is important for material characterization. That type of information can be obtained in helium ion microscopy (HIM) utilizing channeling. This well known process has been studied extensively in the past in the context of ion scattering methods such as Rutherford backscattering (RBS) and medium and low energy ion scattering. Like many ion scattering phenomena it is well understood for very high energies of several hundred keV up to MeV that are used in RBS. Although energies in HIM are different and typically range between 5 keV and 40 keV, the existing theories can in fact describe the channeling phenomena with sufficient precision.

Here, we highlight the importance of channeling in image formation in HIM. By the example of {111} textured gold, we show how the secondary electron (SE) yield can vary by a factor of two. Judicious use of this knowledge allows for an efficient optimization of signal and contrast in HIM images. An experimental procedure to accurately obtain crystallographic information in HIM is described in this work. The strong dependence of channeling on the angle of incidence of the beam is used to perform crystal orientation mapping. This procedure provides information that is comparable to electron backscatter diffraction (EBSD). We also show that a full fledged scattering calculation is not necessary to access this information. Simple geometric considerations are in fact sufficient.

Another application of the channeling phenomenon in HIM is demonstrated on the example of ultra thin surface layers. Channeling provides an unexpected contrast of a lighter elements material on top of a heavier element substrate in backscattered helium (BSHe) imaging. HIM already provides superior surface sensitivity in SE based images. The contrast mechanism described below for BSHe images extends this capability to backscatter images.

3.2 Experimental

All images were recorded using an ultra high vacuum (UHV) Orion®Plus Helium Ion Microscope from Carl Zeiss NTS [53]. The microscope is equipped with an Everhart-Thornley (ET) detector to record SE images. A microchannel plate that is placed in the beam path below the last lens

is used to record BSHe images. The base pressure of 2×10^{-9} mbar allows for extended exposure of the same sample area to the He ion beam. The near absence of hydrocarbons in the sample chamber effectively reduces carbon build-up in the investigated sample area as compared to the standard instrument. High resolution images have been recorded using the ET detector and a typical primary energy of 33 keV. To enhance the channeling contrast, some of the data has been recorded with a lower ion beam energy of 15 keV. This increases the scatter probability and results in a better signal to noise ratio for ion channeling contrast images.

Commercially available polycrystalline gold {111} films on glass with a chromium interlayer have been flame annealed for 5 minutes using a hydrogen flame. The primarily {111} textured surface orientation of the grains was confirmed by X-ray diffraction measurements. Orientations of the grains were found to have a 3.5° wide angular distribution. The samples were cleaned for 15 min in the load lock using a 10 W air plasma.

Patterns of self-assembled monolayers (SAM) have been created using a PDMS stamp and gas phase silanization. Orthogonal stripes with an identical width of 4 μm of (3- Mercaptopropyl) trimethoxysilane (MS: $C_6H_{16}O_3SSi$) and Triethoxy(1H,1H,2H,2H-tridecafluoro-n-octyl)silane (PFS: $C_{14}H_{19}F_{13}O_3Si$) were formed on the native oxide present on Si {001} wafers [54]. The thickness of the layers corresponds to the length of the molecules which are 7 Å and 11 Å for MS and PFS, respectively.

Para-sexiphenyl (6P) thin films were grown on Si{001} wafers covered by a native oxide in an UHV system with a base pressure of 1×10^{-10} mbar. Prior to thin film growth the substrate has been flashed to 500°C. 6P was deposited at room temperature from a Knudsen cell [55, 56].

To obtain a measure for the backscatter probability, angle dependent projections of the crystal lattices have been calculated using a simple geometric model of the crystal slab. In the model of the gold crystal, the atom radius has been fixed to 0.68 Å and the lattice parameter is 4.08 Å (density 6×10^{22} cm^{-3}). To speed up the calculations, the thickness of the crystal slab was restricted to 14 layers. This corresponds to a thickness of 3.06 nm and is greater or equal to the information depth in SE images. The latter depends on the escape depth of SEs in HIM [31]. The crystal slab was tilted and rotated with respect to the (111) surface plane and the [1$\bar{1}$0] direction, and the blocked area fraction (opacity) of the projection calculated. To avoid lateral finite size errors, an area of

$14\,nm^2$ has been used for averaging and border atoms were included with their corresponding area fraction.

Projections of the silicon crystal lattice were calculated with and without a graphene like carbon overlayer on top of the silicon slab. Atom radii have been fixed to $0.42\,Å$ and $0.30\,Å$ for silicon and carbon, respectively. Lattice constants of $5.43\,Å$ and $2.46\,Å$ have been used for silicon and carbon, respectively. To speed up the calculations the thickness of the crystal slab has been restricted to 24 layers or 6 unit cells, this thickness equals $3.3\,nm$. The crystal slab was rotated and tilted with respect to the [001] direction and the projected blocked area fraction (opacity) was calculated for the area of one unit cell – or in other words eight neighboring channels. Due to the mismatch in unit cell size the carbon adatom positions were different in these eight channels. To average over many possible configurations for the overlayer atoms, the adlayer has been shifted across 25 different positions relative to the bulk.

SRIM [57] calculations to assess the backscatter probability and the range of the helium particles were performed using SRIM-2011 and the quick Kinchin-Pease formalism [57, 58]. To ensure a sound statistical result 1×10^5 He ions with the selected energy have been traced in appropriately thick slabs of the bulk material.

3.3 Channeling in Helium Ion Microscopy

3.3.1 Channeling phenomenon

In Fig. 3.1 measured SE images of a polycrystalline gold film with a {111} texture are shown. The images with a field of view (FOV) of $10\,µm$ were recorded using a sample tilt (polar angle) of 35°, a beam energy of $15\,keV$ and an ion dose of $4.9\times10^{14}\,cm^{-2}$. In Fig. 3.1(a) individual grains with an average size of $1\,µm^2$ can easily be distinguished not only by their distinct shape, but also through the different gray levels. In Fig. 3.1(b) and Fig. 3.1(c), HIM images are presented that show the same area but for different stage rotation angles (sample rotation is about the [111] surface normal). The gray level of the highlighted grain changes from dark gray to a brighter shade and finally back to a medium shade of gray. The gray level of the other grains changes in an identical sequence, but with different starting points. As we will show below this allows us to identify the orientation of the individual grains.
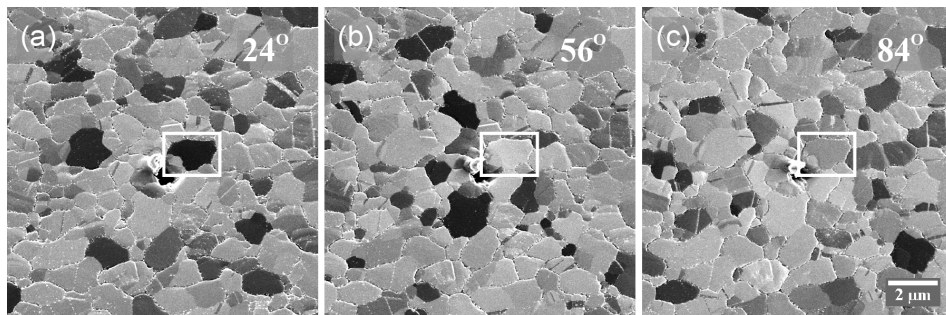
Figure 3.1: HIM SE images of the hydrogen flame-annealed polycrystalline Au{111} film taken with a primary energy of 15 keV and an ion dose of 4.9×10^{14} cm^{-2}. Relative sample rotation angles around the surface normal are 24°, 56° and 84°. The polar angle is fixed at 35°. FOV: 12.5 µm.

A BSHe channeling contrast image recorded with the MCP detector is presented in Fig. 3.2. Although, there is excellent contrast at the selected acceleration voltage of 20 keV and the mild dose of 1.11×10^{15} cm^{-2}, the signal to noise ratio is considerably worse compared to the SE images presented above. The reason for this is rooted in the low number of ions used per pixel. In the present case only 2375 ions are used per pixel, of which roughly 20% are backscattered according to SRIM calculations. However, not all of these 500 ions will be counted by the detector. Different to the SE images, BSHe images contain information on the bulk crystallography. The achievable information depth will depend on acceleration voltage and elemental composition of the specimen. However, for gold and 20 keV it is of the order of a few tens of nanometers, and consequently higher than the SE information depth of 2 nm to 3 nm [31].

The stability of the contrast in the SE images is quite remarkable. In this study 34 images of the same area were recorded, which corresponds to a fluence of 1.6×10^{16} cm^{-2}. This value is well below the fluence needed to induce significant modifications of the sample (see Chapter 4).

In Fig. 3.3(a) the average SE yield of several grains is plotted versus the azimuthal angle for two different primary energies. The SE yield of individual grains has been normalized with respect to the maximum intensity and data for the individual grains has been aligned using the position of the strongest peak. We can understand the angular dependence of the SE yield when we view it as a direct result of the fcc structure of the crystallites in the Au{111} film. The insets in Fig. 3.3(a) are models of the Au crystal structure. For a given thickness of the sample slab,
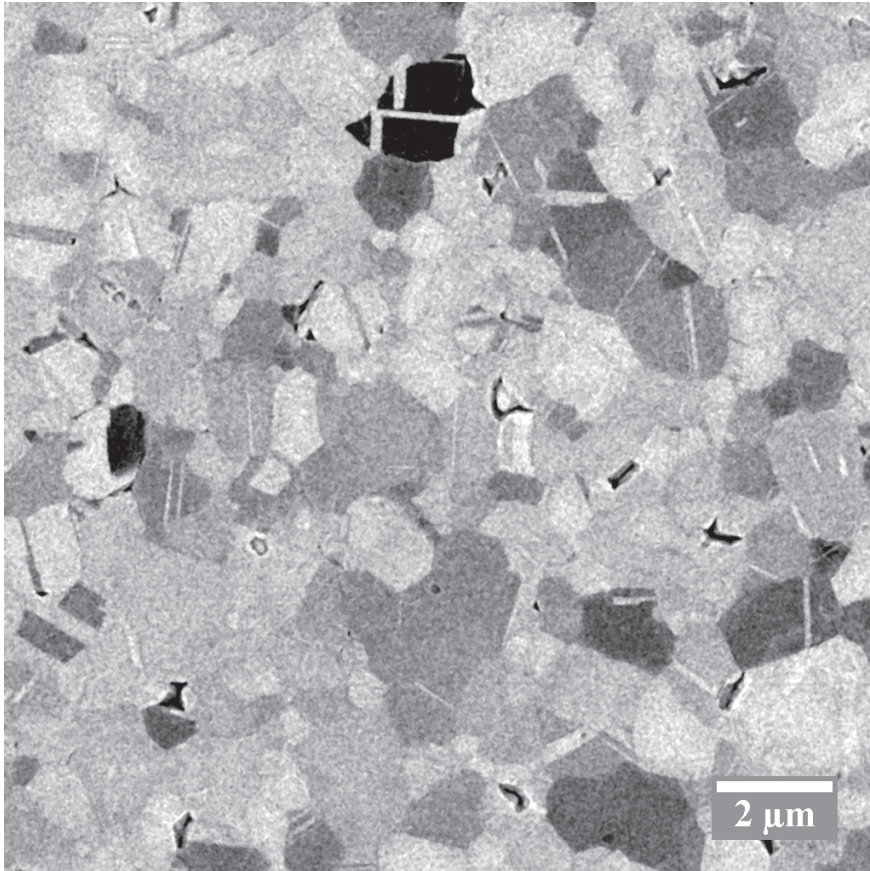
Figure 3.2: HIM BSHe images of the hydrogen flame annealed polycrystalline Au{111} film. A beam energy of $20\,\mathrm{keV}$ and an ion dose of $1.11\times10^{15}\,\mathrm{cm}^{-2}$ have been used. The stage tilt was 0°. FOV: $15\,\mathrm{\mu m}$.

different fractions of the projected view of the crystal will be occupied by Au atoms. As a result, helium atoms traveling in a direction perpendicular to the projected plane will experience a different channeling probability. If a {111} oriented fcc crystal is tilted by 35° with respect to the incoming beam, for a specific azimuthal orientation the {110} planes will be parallel to the trajectory of the incoming helium. For symmetry reasons, this configuration can be found every 120°. Particles traveling along the low index <110> directions will undergo a series of small angle collision with the atoms of the crystal. This results in a focusing action that will allow the particles to travel along the channel [59]. However, to excite electrons in the inner shells of the lattice atoms hard collisions are necessary. Subsequently, a low number of SE is generated under this conditions [60]. For the images presented in Fig. 3.1 all grains have their {111} plane parallel to the substrate surface. However, the in-plane orientation is random. Consequently, only some grains will be oriented in a channeling direction, while others are not. As a result, a strong grain contrast can be achieved [61, 62], where dark grains are viewed along a channeling direction, while bright crystallites have a blocking orientation. For the marked grain in Fig.3.1 the stage rotation angles correspond to the azimuth angle around [111] measured with respect to the [1$\bar{1}$0] surface direction.

Figure 3.3(b) is the result of a simple channeling simulation. A gold fcc crystal slab has been tilted by 35° with respect to the (111) plane and rotated around [111] with respect to the [1$\bar{1}$0] direction. The opacity has been calculated for different azimuthal angles. When compared to the experimental data in Fig. 3.3(a) it is obvious that the peak positions are reproduced correctly. The shoulders at 75° and 105° are artefacts from the limited crystal slab thickness. In our calculation the fraction of the opaque projected area is directly related to the SE yield measured in the experiment in a qualitative way. In accordance with the experimental results, the calculation predicts minima in the opaque area fraction for the [$\bar{1}$4$\bar{1}$] and [$\bar{1}$10] crystal directions.

The depth and width of the minima will depend on the diameter of the simulated atoms. This diameter corresponds to the cross section for scattering and will in turn depend on the actual collision parameters, in particular the primary energy of the incoming particles. The effect of the latter can be seen from Fig. 3.3(a): the channeling minima are wider and deeper for the lower energy. The maximum critical angle is determined by the maximum transverse energy [59]. Thus, in case of lower ion energies
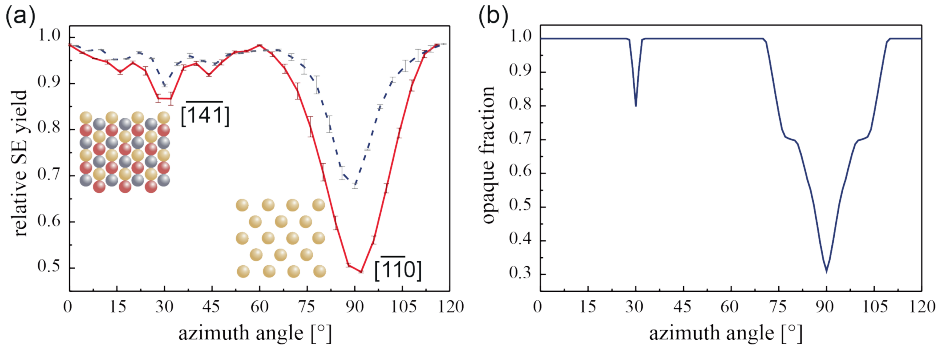
Figure 3.3: SE yield and opaque fraction for a polar angle of 35° with respect to the (111) plane. The azimuthal angle around the [111] direction is measured with respect to the [1$\bar{1}$0] direction. (a) Experimentally obtained SE yield dependence on the azimuthal angle. He$^+$ primary energies are 15 keV (—) and 33,6 keV (- - -). The insets present the view of the crystal along the two indicated directions. The color code is as follows: gold: 1st layer, silver: 2nd layer, and red: 3rd layer. (b) Calculated opacity of a gold crystal lattice (14 atomic layers). The used effective atom diameter is 0.68 Å.

the opening angle is bigger and, as a result, more incident ions can be trapped in the channel. Therefore, the lower energies will result in a higher contrast of SE images.

3.3.2 Orientation mapping with channeling

The results that we have presented demonstrate that it is possible to obtain crystallographic information directly from SE images in HIM. This information is also accessible from BSHe images, however the usage of SE has several advantages. First, the required ion dose for a high quality image with a good signal to noise ratio is significantly lower. This is in particular important for light bulk materials. The gold sample that has been used here has a comparatively large backscatter probability for helium atoms. The situation changes however for many technologically relevant materials like aluminum, iron and silicon. Second, the small information depth of the SEs enables the probing of adlayers and coatings with a thickness in the nanometer range.

In Fig. 3.4 we show the calculated positions of channeling minima of a fcc crystal for imaging with SEs. No exhaustive channeling calculation is necessary to obtain this plot. A simple geometric projection of the first

few layers along the beam direction suffices. Despite the fact that the orientation map in Fig. 3.4 resembles a typical stereographic projection of channeling minima [63] or a Laue map [64] for crystal orientations, we briefly highlight the differences. Low index orientations such as the <110> directions are located in the nodes visible in the map. Different to a typical stereographic projection of channeling directions, the nodes are connected by a continuous minimum with only small depth undulation. The presence of these shallow lines is directly related to the limited slab thickness used in the calculation. An increase of slab thickness reduces the width and depth of the channeling minima. While stereographic projections give measures for the depth of channeling minima, this information has to be carefully reviewed in the present projection of the opaque crystal fraction map. The width and depth of the minima also depends on the ratio of the nearest neighbor distance and effective atom radius. In this case we have simply used the ionic radius of gold and a hard wall potential, without stopping effects. However, the parameters that were used create an excellent match between the experimental and simulated data (see Fig. 3.3). In particular, the presence of the zone lines allows for an an easy alignment of experimental maps to calculated data and the successive identification of crystal orientation.

The map presented in Fig. 3.4 has been used to index several grains. A color coding representing the different orientations has been used to illustrate the different in-plane orientations of the grains. Such a color coded map is shown in Fig. 3.5. Figure 3.5 shows the orientation for the images of Fig. 3.1. The grain that is highlighted in Fig. 3.1 is darkest for a 24° rotation angle. This corresponds to a yellow-green color in Fig. 3.5. The color scale ranges from a 0° to 120° azimuthal rotation around [111]. Consequently, the color of an individual grain corresponds to the azimuthal angle for which a <110> direction in this gold grain is parallel to the beam. For the marked in Fig. 3.1 grain the stage rotation angle for this condition is 24°.

Figure 3.4: Calculated map of channeling directions for an fcc crystal. The lines connecting the nodes at low index direction in the polar plot represent channeling directions in the used thin slab of an fcc crystal. The color coding (opaque fraction) allows a qualitative interpretation of the width and depth of the scattering minima.
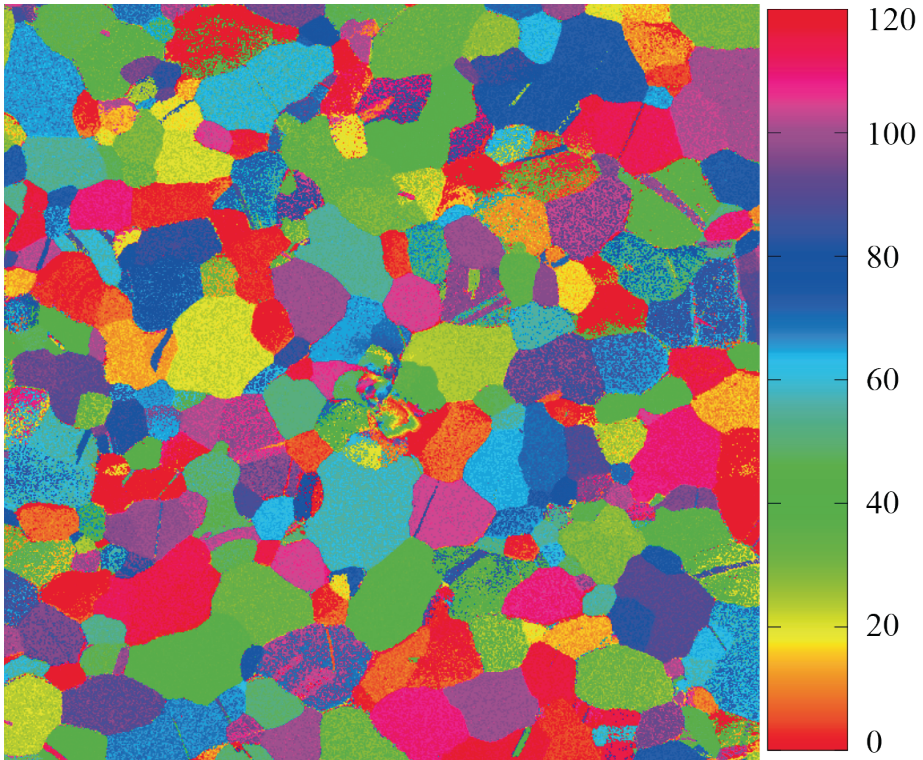
Figure 3.5: Color coded orientation map of a polycrystalline gold film. The colors indicate the azimuthal angle around the [111] surface normal for a 35° sample tilt at which a <110> direction is aligned with the incoming helium ion beam. Parts of the dataset used are presented in Fig. 3.1.

3.4 Imaging ultra thin layers with Helium Ion Microscopy

3.4.1 Thin organic layers

In Fig. 3.6 HIM images of a network of two SAMs – MS and PFS – are presented. The images were recorded with a beam energy of 15 keV and an ion dose of 2.46×10^{16} cm^{-2} at normal beam incidence. Fig. 3.6(a) has been obtained using the ET detector. SEs in HIM originate from near surface regions. The characteristic escape depth of SEs in carbon is 1 nm [31]. The high contrast between the different patches – and the high lateral resolution – are a result of this characteristic of the SEs in HIM. All the SEs contributing to the different contrast patches are generated under identical conditions, nearly exclusively within a thin surface layer of the relevant material (SiO$_2$, PFS, or MS). However, we assign the bright structureless areas to the uncovered SiO$_2$/Si substrate. It is understood that because of the relatively low work function of SiO$_2$ these areas are brightest. The work function of PFS and MS are 6.6 eV and 5.3 eV [65], respectively. The value for PFS has been extrapolated from a shorter fluorinated alkanethiol [66], and should be treated as an estimate. We can therefore identify the medium light gray areas below and above the Si patches as MS covered. The medium dark areas to the left and the right of the Si patches are covered by the higher work function PFS layer. The remaining square is covered by an unknown mixture of both – MS and PFS. A clear statement on the work function or the contrast mechanism for this remaining patch is therefore difficult.

Figure 3.6(b) shows the simultaneously recorded BSHe image. Interestingly, the SAMs are not only discernible but can also be distinguished. In addition, small details at the edge of the vertical SAM stripes are clearly visible. The relative average backscattered He yields with respect to SiO$_2$/Si (BSHe yield: 1) are 1.58 and 1.45 for PFS and MS, respectively. We will discuss the underlying contrast mechanisms below, however, we first highlight another example of an ultra thin surface structure that was made visible in BSHe images.

In Fig. 3.7 HIM images of single layer high ($\approx$2.6 nm) 6P islands on native oxide covered Si{001} wafers are shown [55,56]. Figure 3.7(a) is an ET image of such an island. The FOV is 11 µm, the primary energy was 20 keV and an ion dose of 3.21×10^{15} cm^{-2} has been used. The ramified
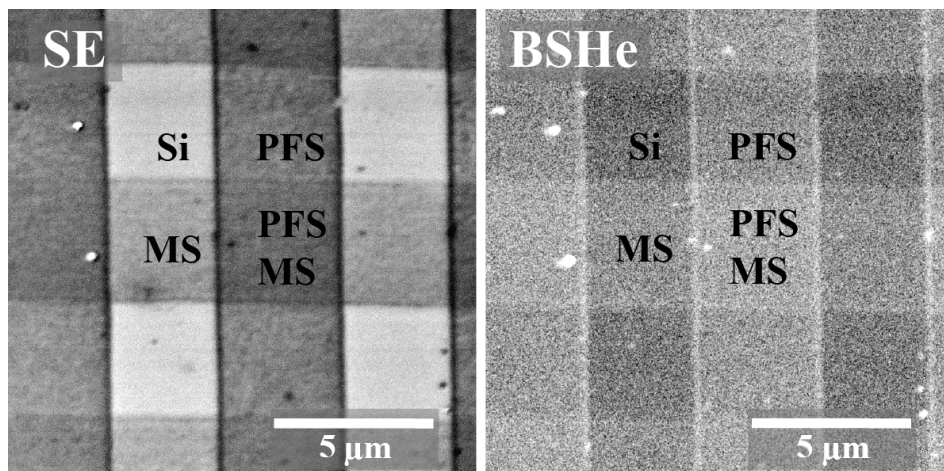
Figure 3.6: HIM images with a FOV of 20 µm of thin organic layers on Si{001}. Data was recorded with 15 keV beam, and an ion dose of 2.46×10^{16} cm^{-2}. (a) ET image of stripes of PFS (vertical) and MS (horizontally). The different areas and their termination are indicated. (b) BSHe image recorded simultaneously with (a). The different surface terminations can be distinguished.

shape of the island (dark) is clearly visible against the bright silicon substrate. Figure 3.7(b) is the simultaneously recorded BSHe image. The shape of the island (bright) can easily be distinguished against the darker background of the silicon substrate. Figure 3.7(c) shows a different island recorded with a sample tilt of 10°, but otherwise unchanged conditions. The corresponding BSHe image presented in Fig. 3.7(d) does however not show a signature of the island. We note that the overall gray level in Fig. 3.7(d) is found to be higher than for the bare silicon in Fig. 3.7(b) and close to that of the 6P island in Fig. 3.7(b).

3.4.2 De-channeling mechanism

As we have seen above, BSHe images can be used to obtain information on ultra thin surface structures on crystalline substrates. In this context, the last part of the previous sentence is important. We now discuss the role of channeling in the underlying crystalline substrate for obtaining the above presented BSHe images.

In both experiments a thin layer of a lighter elements has been deposited on top of a heavier substrate. Different to the ET images where
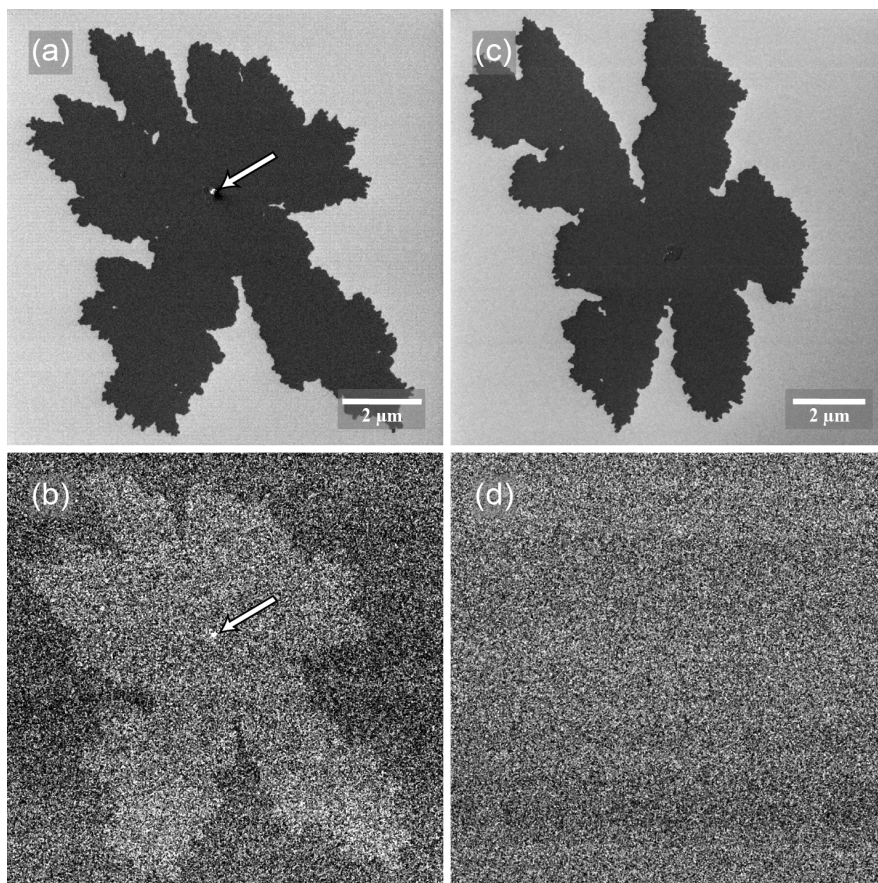
Figure 3.7: HIM images of single layer 6P islands on Si{001}, recorded with 20 keV beam and an ion dose of 3.21×10^{15} cm^{-2}. (a) ET image with a FOV of 11 µm recorded under normal incidence. The island and a small second layer island (bright spot in the center and marked by an arrow) can be seen. (b) Corresponding BSHe image. The island and the second layer island (marked by an arrow) can be seen. (c) ET image with a FOV of 12 µm recorded under identical conditions as (a,b) but with an incidence angle of 10°. The island can be seen clearly. (d) In the corresponding BSHe image the island is invisible.

SEs are generated in surface near regions, the backscattering of He is a bulk effect. For a layer of heavy elements on a lighter substrate one expects an increased BSHe yield for the following two reasons. (1) The heavier element has a larger cross section and will therefore add to the BSHe yield. (2) The adlayer decreases the energy of the primary beam, thereby increasing the backscatter probability and reducing the range of helium in the material. The increased scattering will lead earlier – in terms of energy and depth – to hard collisions with large scattering angles and result in a larger deviation from the initial particle trajectory. We will discuss this in more depth in the next paragraph. For the present case where a light adlayer (carbon) covers a heavier substrate (silicon) (1) does not play a significant role and (2) will be weak in general.

To underline the above statement, SRIM calculation were used to obtain a generic view of the expected processes. Artificial silicon samples with a thickness of $1\,\mu m$ and a $10\,nm$ adlayer of either heavy (Pb) or light (Li) elements, and without adlayer were compared. 1×10^5 He$^+$ ions with a primary energy of $35\,keV$ under normal incidence were used to perform the calculation. The results are summarized in Table 3.1. As expected, the backscatter yield for Pb/Si (1.9%) is higher by a factor of two compared to the other two combinations (0.9% for both cases). While the light adlayer does not affect the lateral range and straggle of the He, the heavy adlayer induces an 8% larger lateral range and a 10% increased lateral straggle. Here, straggle is defined in accordance with the SRIM software to be the square root of the second moment of the range distribution [57]. Although these values represent averages which are dominated by the ions stopped deep in the sample, a comparable relative change will occur closer to the surface for the helium particles that will eventually be backscattered. This will have a negative influence on the lateral resolution that can be achieved in BSHe images. SE images will not be affected since the SEs are generated in the first few nanometers of the sample where the beam is still sharply focused.

For the case of the SAMs on SiO$_2$ (Fig. 3.6), SRIM calculations have been performed to estimate the backscatter probability from the different layers. Bulk samples of SiO$_2$, MS, and PFS have been created and exposed to 5×10^5 He$^+$ ions with a primary energy of $15\,keV$. The backscatter probabilities obtained are 1.73% for SiO$_2$, and 0.7% for MS and PFS. In this model calculation SiO$_2$ has the highest backscatter probability and should appear brightest in BSHe images. Keeping in mind the considerations in the previous paragraph and the calculated backscatter

Sample	BSHe	Direction	Range [Å]	Straggle [Å]
Pb/Si	1863	long.	3095	952
		rad.	1567	782
Li/Si	881	long.	3261	918
		rad.	1443	712
Si	979	long.	3190	917
		rad.	1446	714

Table 3.1: Scattering process dependence on adlayer material as obtained by SRIM. For each adlayer/sample combination the number of backscattered helium atoms and the longitudinal and radial ion ranges (in Å) are given. 1×10^5 He ions with a primary energy of 35 keV under normal incidence were used in the calculation.

probabilities, no additional contribution is to be expected from the MS or PFS covered areas. However, a detailed analysis of the image data reveals that relative to SiO_2/Si the backscatter probabilities are higher by a factor of 1.45 and 1.58 for MS and PFS, respectively.

As we have demonstrated in Fig. 3.7, the polar angle of the incident He beam is critical for the contrast in BSHe images. In Fig. 3.8 we show the result of calculations of the opaque area fraction for a silicon {001} crystal. The graphs show the opaque fraction of the crystal, which is proportional to the backscatter yield. For normal beam incidence (Fig. 3.8(a)) 15% of the area is blocked (blue dashed line). Adding a single carbon overlayer increases the opaque fraction to 29% (dark solid line). At normal incidence, this corresponds to an increase in the blocked fraction by 93%, independent of the azimuth angle. Tilting the incident beam with respect to the surface normal increases the overall backscatter probability, but reduces the expected contrast ratio between a clean Si crystal and one that is covered by a single adlayer. The increased yield of backscattered He is evident by comparing Fig. 3.7(b) and Fig. 3.7(d). The BSHe yield has increased substantially for the uncovered surface areas. The expected contrast depends on the azimuthal angle and varies between 26% and 4% with a mean value of 8% for a 10° beam tilt. The insets in Fig. 3.8 show the model crystal slabs with carbon adlayer that were used, illustrating the reduced transparency for the tilted cases. Despite the simplicity of this model it nicely confirms the physics involved in the decrease in contrast between areas with and without an adlayer when the sample is tilted. For thicker adlayers this effect is going to
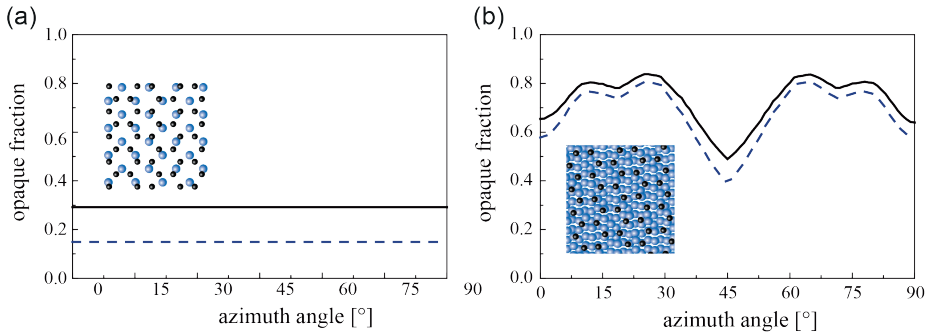
Figure 3.8: Simulation of dechanneling contrast for clean and carbon covered Si. The graphs show the opaque fraction of the projected crystal lattice. Blue dashed lines are obtained for a clean Si(001) crystal while the black lines are obtained with a thin carbon layer added. (a) Normal incident. The opaque projected area fraction is 15% and 29% for the clean and carbon covered surface, respectively. There is no azimuthal dependence for this incident angle. (b) The same calculation but for a 10° sample tilt. The average opaque projected area fractions are 68% and 73% for the clean and carbon covered surface, respectively. A clear dependence on the azimuth angle exists.

be more pronounced because the channels in the underlying crystal are more effectively blocked. In fact, the amount of backscattered He due to the thin 6P adlayer in Fig. 3.7(b) is comparable to the amount for the uncovered, but tilted, area in Fig. 3.7(d).

The results presented in Fig. 3.6 and Fig. 3.7 are based on the angle dependent channeling probability described above. In both cases the surface is covered by a native oxide. We assume it to be amorphous and have a thickness about 2 nm. This will cause a partial blocking of the underlying channels in Si{001} However, the effectiveness of the dechanneling will depend on the thickness of the overlayer. A local increase in thickness of the amorphous overlayer will increase the contrast because more He is backscattered. This can be seen in the organic overlayer in particular for the rims of the vertical stripes of PFS in Fig. 3.6(b). The edges of the stripes are thicker [54], and lead to an increased chance for an ion to be deviated from the initial trajectory. Consequently this results in more backscattering of He due to the enhanced dechanneling. A similar effect can be observed for the small second layer island on top of the 6P island in Fig. 3.7(a,b).

3.5 Conclusions

We have demonstrated the importance of channeling in HIM using polycrystalline gold films with a <111> texture. To quantitatively explain the orientation dependent changes in contrast it is not necessary to perform a full calculation of the scattering process. A straightforward projection of the crystal lattice is sufficient to identify low index channeling directions. Such a map has been calculated for an fcc lattice and used to determine the orientation of all gold crystallites in the FOV. The effect is observed in both types of HIM images. It is, however, particularly useful in combination with SE images. Because of the limited information depth of SE ion channeling contrast images, crystallographic data from thin adlayers can be obtained. BSHe ion channeling contrast images on the other hand yield similar bulk crystallographic information. This adds a new capability to helium ion microscopy. The possibility to obtain crystallographic information on a per pixel basis strengthens the materials characterization applicability of HIM.

Besides the possibility to obtain crystallographic information, channeling can also be used to obtain information on ultra thin organic and

inorganic layers. We demonstrated that even a submonolayer coverage thin layer can be detected in BSHe images. The enhanced backscattering is a result of changes in the channeling probability and, qualitatively speaking, does not depend on the mass of the participating film or bulk atoms. As an unanticipated result, even light adlayers on heavy substrates can be imaged. We emphasize that this contrast mechanism is purely based on changes in the crystallography of the sample.

Finally, we want to stress the point that this is a clear hint for the importance of good vacuum conditions during HIM measurements. From our geometrical projection based calculation, we conclude that already a single monolayer of carbon can result in a 66% contrast loss. This does not only affect the general performance of the imaging technique but will in particular affect channeling based contrast mechanisms.

Metal surface modification with a He$^+$ beam

Helium ion microscopy (HIM) was used to investigate the interaction of a sub-nanometer He$^+$ ion beam with energies of several tens of keV with metals. HIM is usually applied for visualization of materials with extreme surface sensitivity and resolution. However, the use of high ion fluences can lead to significant sample modifications. We have characterized the changes caused by a sub-nanometer He$^+$ ion beam at normal incidence to the Au $\{111\}$ surface as a function of ion fluence and energy. Under influence of the beam a periodic surface nanopattern develops. The periodicity of the pattern shows a power-law dependence on the ion fluence. Simultaneously, helium implantation occurs. Depending on fluence and primary energy porous nanostructures or large blisters form on the sample surface. The growth of the helium bubbles responsible for this effect is discussed.

4.1 Introduction

The helium ion microscope allows the projection of a He$^+$ beam of several tens of keV with a diameter of 0.4 nm [16] onto a sample. This makes HIM an attractive tool for surface patterning and nanofabrication [67–71]. As helium ions are light particles, sputtering processes are much less effective with HIM as compared to other focused ion beam (FIB) techniques that typically use gallium ions. Nevertheless, helium ion beam imaging can lead to considerable sample – and in particular (near) surface – modifications. The implantation of He – and the associated possible structural and chemical changes – can create substantial problems in experiments where prolonged imaging or high ion doses are required.

The effect of the He$^+$ ions on the target depends as much on the ion beam characteristics as on the properties of the imaged material itself. Existing publications on damage by a sub-nanometer He$^+$ beam mostly concentrate on the interaction of ions with semiconductor materials like silicon [72–75]. In this chapter we investigate the interaction of a He$^+$ beam with metals. Previously, the effect of a low energy He$^+$ ion beam on an atomically flat gold surface was observed by scanning tunneling microscopy (STM) [76,77]. Mounds with a spacing of a few nm were formed. In the current work we have studied the He$^+$ ion induced modifications of crystalline gold samples due to sputtering, helium implantation and defect formation, as a function of ion fluence and energy.

4.2 Experimental

The experiments were performed with an ultra high vacuum (UHV) Orion®Plus Helium Ion Microscope from Carl Zeiss NTS [53] at room temperature. The images were recorded using an Everhart-Thornley (ET) detector. During the measurements the ion current was kept at 0.7 pA. Brightness and contrast settings were kept constant, and the beam was oriented perpendicular to the surface. Three primary ion energies were used in the experiments: 15 keV, 25 keV and 35 keV. The images were recorded with a 0.68 nm pixel spacing, 2 µs dwell time and 32 lines averaging, giving an ion dose per image of 6×10^{16} cm^{-2}. The chamber base pressure during imaging was in the low 10^{-9} mbar range.

The samples were polycrystalline gold specimens, which are commercially available 200 nm thick Au {111} films on a glass substrate with a

Cr interlayer. The textured samples were prepared by hydrogen flame annealing for 5 minutes. As a result of the annealing process, grains with an average size of a few micrometers were formed. X-ray diffraction measurements confirmed the primarily {111} textured surface orientation of the grains with a 3.5° wide angular distribution. The grains have random azimuth orientations. In order to remove carbon contamination, all samples were exposed to a 10 W air plasma for 15 minutes immediately before loading the samples into the main chamber. After ion implantation the topography of the samples was measured with an Agilent 5100 atomic force microscope (AFM) in intermittant mode. The cantilever was a Mikromasch NSC silicon probe, with a guaranteed tip radius of less than 10 nm, and a typical resonance frequency of 150 kHz. The scan size was $2{\times}2$ µm^2.

4.3 Au {111} surface modification

We have recorded sequences of images of sub-micron size to study the evolution of the Au {111} surface under a sub-nanometer He$^+$ beam as a function of fluence. Ion energies of 15 keV, 25 keV, and 35 keV were used to gauge the influence of the beam energy. The same sample area was exposed to the beam several times with a constant ion dose per scan. The final state of the surface after a fluence of $8.4{\times}10^{17}$ cm^{-2} is shown in Fig. 4.1(a) and (c): at 15 keV primary energy a porous structure is formed on the surface (Fig. 4.1(a)), while in the case of a 35 keV beam a sub-surface helium blister is formed (Fig. 4.1(c)).

We emphasize that due to the low background pressure, the present setup does not suffer from the problem of carbon deposition in the imaged area. This is a common problem in conventional non-UHV HIM and scanning electron microscopes (SEM) [53,78]. The absence of the carbon layer that is normally present, allows us to obtain detailed information on the surface structure and how it evolves during repeated imaging of the same area.

Figure 4.2 shows several images of the gold surface after exposure to identical ion fluences, but with different primary energies. Under the influence of the 15 keV beam a regular nanopattern develops. The topographic contrast increases and the surface pattern becomes more pronounced with each subsequent scan of the same area, which indicates an increase of the corrugation of the pattern. Although the feature spacing
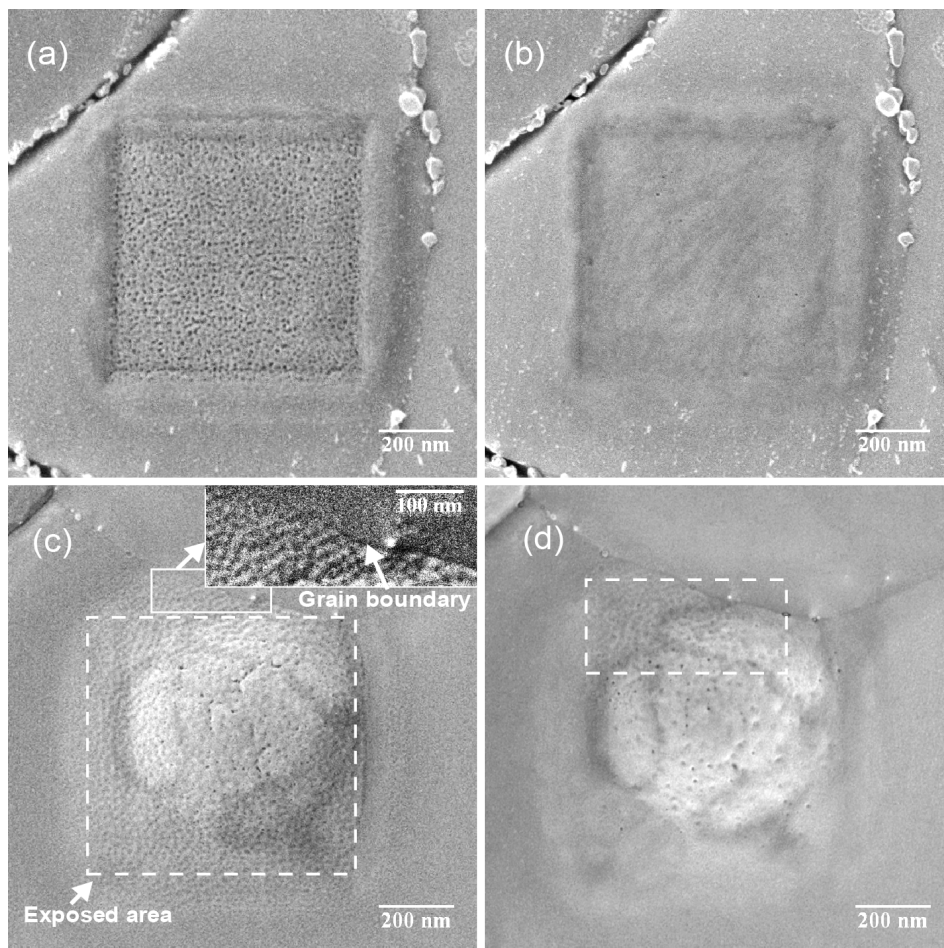
Figure 4.1: HIM SE image of a Au {111} surface, exposed to a He$^+$ beam with a fluence of 8.4×10^{17} cm^{-2} at different energies. The field of view (FOV) is 1.25 μm, pixel spacing is 1.5 nm. (a) Porous structure formed by a 15 keV He$^+$ beam. (b) The same area as in image (a) after 6 weeks storage under dry atmospheric conditions. The surface has partly self-annealed. (c) Blister formed by a 35 keV beam. The area exposed to the beam is marked by a dashed line. The surface has developed a periodic pattern. The influence of the beam is easily visible outside the marked area as well, but does not extend on the neighboring grain (see inset). (d) The same area as in (c), imaged after 16 weeks storage under dry atmospheric conditions. The surface of the blister has partly self-annealed, except the marked area in the vicinity of the grain boundary.
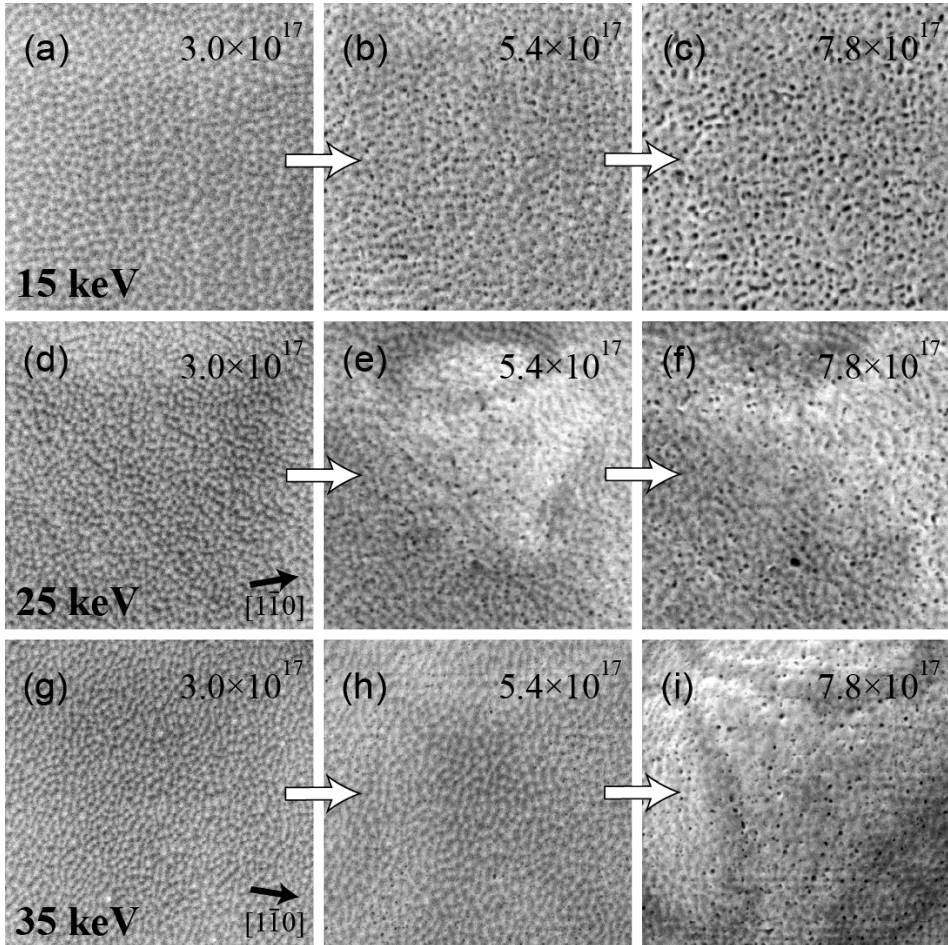
Figure 4.2: HIM SE images of the pattern that develops on the Au {111} surface as a function of ion fluence. Numbers indicate the ion fluence in helium ions× cm^{-2}. Arrows in (d) and (g) indicate the azimuth directions of the grains. The He^{+} beam energies are 15 keV, 25 keV and 35 keV. FOV is 500 nm, pixel spacing is 0.68 nm.

increases with increasing ion fluence, the shape of the features remains almost unchanged and the features do not coalesce. After a fluence of 3×10^{17} cm^{-2} a uniform distribution of holes starts to appear on the surface (see Fig. 4.2(a). With a further increase of the fluence the porous structure gets more pronounced (Fig. 4.2(b) and (c)). In the case of 25 keV primary ion energy the surface modification initially looks similar to the one at 15 keV (Fig. 4.2(d)), but at a fluence of 4.8×10^{17} cm^{-2} a blister forms, which is shown in Fig. 4.2(e). The blister formation leads to bending of the surface and the appearance of bright areas in the images. For larger fluences pores start to appear on the surface of the blister (see Fig. 4.2(f)). A beam with a primary energy of 35 keV initially induces a comparable nanopattern formation process (Fig. 4.2(g)). Higher fluences result in blister formation (Fig. 4.2(h)) and eventually the formation of a large sub-surface helium blister at a fluence of 6×10^{17} cm^{-2} (Fig. 4.2(i)). We also observe some pores on the surface of the blister.

In Fig. 4.3(a) two blisters on grains with different azimuthal orientation are shown. Although, severe damage is done to the surface and bulk of the gold grains, their crystalline nature is still evident. The blisters have equilateral triangles on top. The same triangles are also observed in the BSHe images, hinting at the channeling nature of the contrast. We attribute these dark triangles and rings to channeling along the $\{11\bar{1}\}$ planes of the fcc crystal. The crystalline shell of the blister is bent (see Fig. 4.5(b)) due to the high internal gas pressure. As a consequence the $\langle 111 \rangle$ surface vector locally tilts. This leads to a local channeling condition with the $\{11\bar{1}\}$ planes along sections of the blister, resulting in the dark bands on the blister surface. The contrast changes with variation of the beam incidence angle – the channeling condition is no longer fulfilled and the dark stripes move or even vanish entirely. The orientations of the sides of the triangles in Figs. 4.2(e) and (i) help to determine the azimuthal orientations of the grains. Since we used a [111] oriented fcc crystal, the ions are expected to channel along $\{11\bar{1}\}$ planes (see Chapter 3), which cross the (111) surface along $\langle 1\bar{1}0 \rangle$ directions. Hence, the sides of the triangles are oriented along $\langle 1\bar{1}0 \rangle$, which is indicated with arrows in Figs. 4.2(d) and (g).

The polycrystalline nature of the samples influences the pattern formation as well. First, the pattern propagation is stopped by grain boundaries as can be seen in the inset in Fig. 4.1(c): no pattern or rising of the surface level is observed on the neighboring grain. Second, the pattern orientation depends on the underlying crystal and thus on the orientation
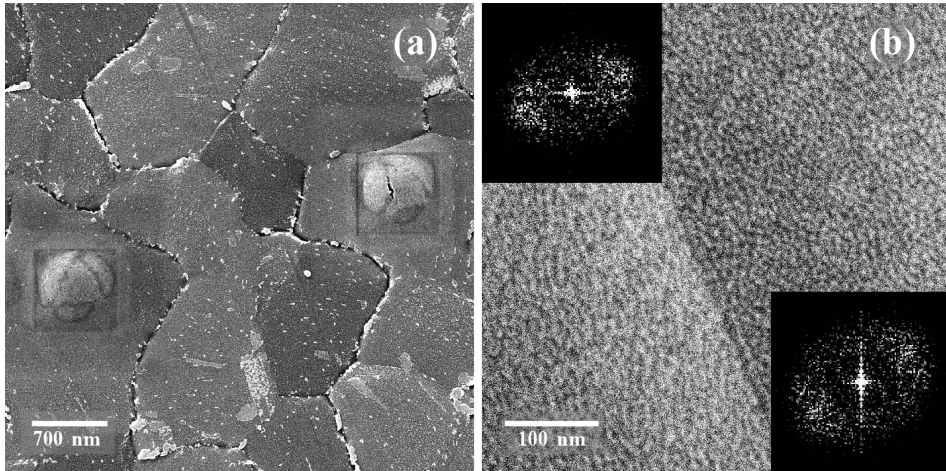
Figure 4.3: (a) Two blisters created by the 35 keV He$^+$ beam on grains with different azimuthal orientation. FOV is 4 μm. (b) HIM SE image of a Au {111} textured polycrystalline film. The insets are 2D FFTs to demonstrate the relation of the patterns with the orientation of the two grains. He$^+$ beam energy is 35 keV. FOV is 500 nm.

of the grain. Figure 4.3(b) displays patterns on two neighboring grains. The patterns are rotated relative to each other on the two different grains, as is also visible from the 2D FFT, shown in the insets.

The average pattern periodicity was extracted from the images by analyzing 2D autocorrelation functions (ACF). The dependence of the nanopattern periodicity on the He$^+$ fluence for different primary energies is shown in Fig. 4.4. The periodicity does not show a significant energy dependence and increases from 8.3 ± 0.3 nm to a maximum of 16.9 ± 0.4 nm, showing a power-law dependence on the ion fluence with a coarsening exponent of 0.26 ± 0.01. The same scaling with a time factor of 0.27 ± 0.02 was obtained by Ramana Murty et al. [77]. The authors studied the surface morphology of Au{111} during sputtering with 500 eV Ar$^+$ ions incident at 45° by real-time X-ray scattering. At 20-60°C temperatures they observed the formation of mounds with a characteristic spacing. A similar pattern was also observed on Cu{110}, sputtered by 1 keV Ar$^+$ ions at 320 K and normal incidence [79]. The corresponding scaling factor was 0.26 ± 0.02. To a certain extent, sputter erosion and atom deposition are similar processes. A continuum model for the mound formation in molecular beam epitaxy (MBE) predicts a coarsening exponent of 0.25 [80], which is very close to the measured values.
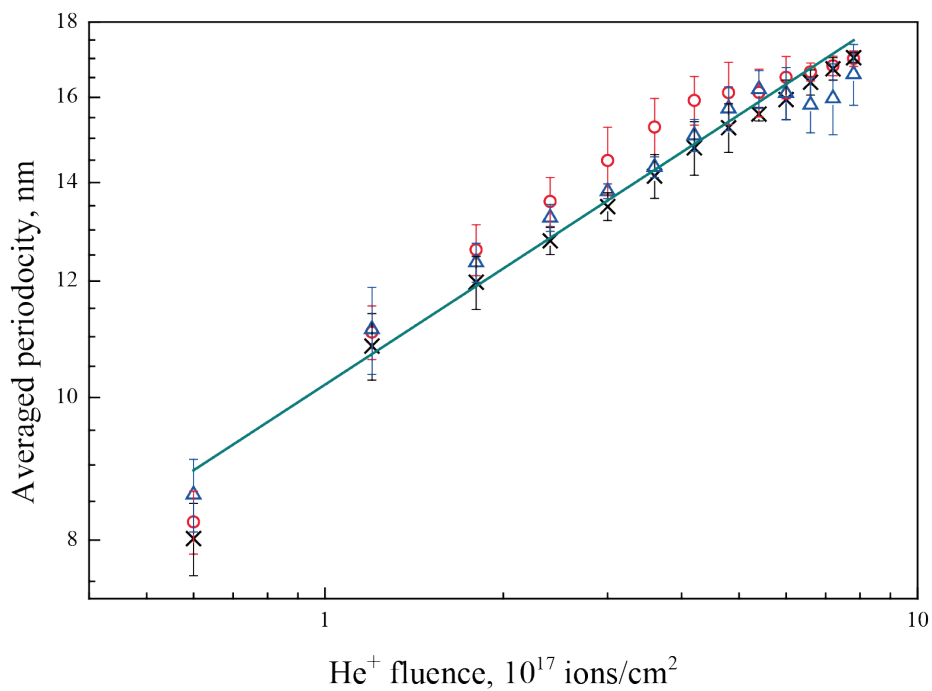
Figure 4.4: Dependence of the Au {111} average pattern periodicity on helium fluence for 15 keV (○), 25 keV (×) and 35 keV (△) He$^+$ beams.

The pattern exhibits a preferential orientation along the $\langle 1\bar{1}0 \rangle$ direction (Fig. 4.2(d) and (g), as well as the 2D FFTs in Fig. 4.3(b)). This suggests, that the pattern formation is governed by diffusion processes of gold adatoms and surface vacancies. Together with the sputtering processes it leads to surface roughening and the development of a periodic pattern. Although the sputtering rate is low, it cannot be completely neglected. As He$^+$ ions impinge on the surface at normal incidence, the sputtering of gold atoms by the direct energy transfer from incoming helium is unlikely. Furthermore, the energy transfer from light helium ions to gold atoms in general is limited because of the unfavorable mass ratio. The sputtering is mainly caused by short-range gold recoils and backscattered helium [81, 82]. The presence of the pattern outside of the irradiated area (Fig. 4.1(c)) is additional evidence of the sputtering by gold recoils. Additionally, the gold interstitials themselves are a source of adatoms on the surface. Gold interstitials are able to travel a few tens of nanometers outside the exposed area, but they cannot cross grain boundaries.

The pattern orientation along a specific crystallographic direction can be explained by considering its formation as a result of the suppression of interlayer diffusion by the step edge or Ehrlich-Schwoebel barrier [77, 79, 83–87]. The activation energy for vacancy diffusion on Au{111} is much higher than the one for adatoms [88], hence we can suppose that at room temperature adatoms are dominantly responsible for the pattern formation. The presence of a step edge barrier along $\langle 1\bar{1}0 \rangle$ does not allow the adatoms to descend the $\langle 1\bar{1}0 \rangle$ step, and produces a net uphill flow. As a result, mounds are formed along a $\langle 1\bar{1}0 \rangle$ direction. However, one would expect a homogeneous distribution of all three possible pattern orientations due to the symmetry of the {111} surface [87]. The out-of-plane orientation of the grains has some angular distribution. Hence, the surfaces are not atomically flat and have a local miscut. The step edges run in one of the three high symmetry directions that become preferential for the pattern orientation on any one grain.

The exposed areas were imaged again after several weeks. Samples were stored under dry ambient conditions between the experiments. As can be seen in Fig. 4.1, the surface has a tendency to self-anneal over time. In Fig. 4.1(b) the same area as in Fig. 4.1(a) – which was initially exposed to a 15 keV He$^+$ beam – is presented, but after 6 weeks. The blister, formed by the 35 keV beam and presented in Fig. 4.1(c), was imaged again after 16 weeks. The image is shown in Fig. 4.1(d). In both cases the pattern has almost completely vanished, except in areas close

to the grain boundary (inset in Fig. 4.1(c)), which apparently acts as an efficient sink for adatoms and interstitials. Thus it hinders the smoothing of the surface in the vicinity. The surface is smoothed, but after a few repetitive scans, the pores, hidden deeper in the substrate, open again. The blister shell self-anneals over time, indicating a possibility to heal the defects. That process may be enhanced by in-situ heating of a sample during ion bombardment.

We mention, that the surface modification depends not only on the final fluence, but also on the speed at which it was generated. With an increase of the dose per scan, the modifications occur more swiftly and are more severe.

4.4 Helium implantation

Helium implantation occurs during sample irradiation. Since HIM SE images do not contain height information, we have used AFM to directly measure the volume that is occupied by the implanted helium. As a result of the low background pressure of hydrocarbons in the UHV HIM we can exclude false volume estimations due to carbon contamination.

The change of the surface profile with ion fluence for a primary energy of 35 keV is shown in Fig. 4.5(a). After a fluence of 4.2×10^{17} cm^{-2}, the surface is still comparatively flat (dashed line), but already for a slightly larger fluence a subsurface blister develops. The profile of a growing blister at 4.8×10^{17} cm^{-2} is shown by the dash-dotted line. At 6×10^{17} cm^{-2} a blister with a stable shape has developed (solid line).

After an initial dose of 6×10^{16} cm^{-2} the exposed area is eroded by 1 nm–1.5 nm with respect to the unirradiated surface. This is the result of sputtering of a few gold layers. The signature of this sputtering related indentation remains discernible in all subsequent images. After doubling the dose to 1.2×10^{17} cm^{-2}, helium implantation has a noticeable effect: the surface of the exposed square and also the unexposed area adjacent to it, starts to rise with increasing ion fluence. The influence of the helium implantation extends as far as 144 ± 12 nm (15 keV), 162 ± 6 nm (25 keV) and 181 ± 7 nm (35 keV) away from the exposed area. In Fig. 4.5(b) the increase of blister volume due to helium implantation is presented as a function of ion fluence. The volume depends linearly on the fluence up to 4.2×10^{17} cm^{-2}. After this total dose, the volume occupied by ions implanted at 15 keV stagnates at $15.8 \pm 0.3 \times 10^6$ nm^3.
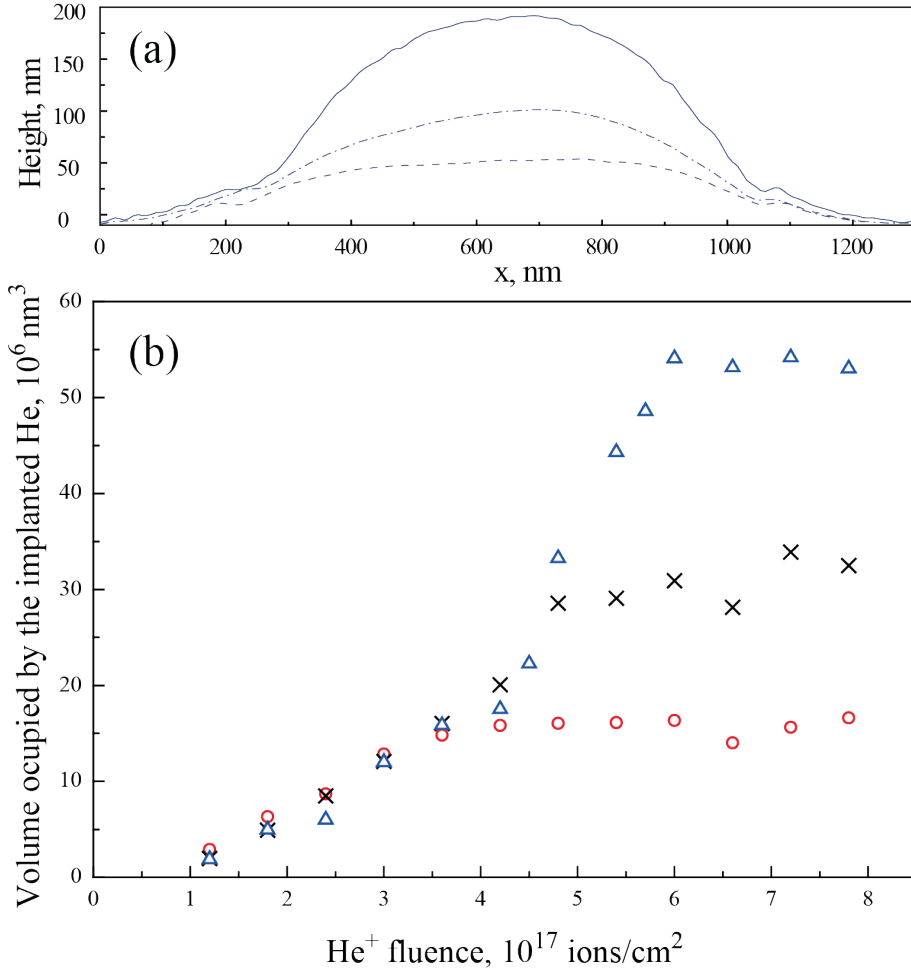
Figure 4.5: (a) Surface profiles after different ion fluences delivered by a 35 keV beam. The surface is evenly raised after 4.2×10^{17} cm^{-2} ($---$). $-\cdot-$ line shows the profile of a blister that starts to form after a fluence of 4.8×10^{17} cm^{-2}. After 6×10^{17} cm^{-2}, the blister develops a stable shape (—). (b) Volume occupied by the implanted helium as a function of helium fluence. The beam primary energies are 15 keV ($\circ$), 25 keV ($\times$) and 35 keV ($\triangle$).

In the case of 35 keV ions, after a fluence of 4.2×10^{17} cm^{-2} a more rapid expansion begins. Later, when the fluence reaches 6×10^{17} cm^{-2}, the volume saturates at $54.2\pm0.4\times10^6$ nm^3. For the energy of 25 keV the rapid expansion sets in at the same fluence, but saturates at an intermediate level of $30.5\pm0.9\times10^6$ nm^3.

In the review by Donnelly [89], surface swelling of several materials (Er, Nb and Ni) under helium irradiation is compared. The general trend of the expansion is similar to the one described in this work. The initial linear expansion was found to be energy independent as well. In the work of Terreault et al. [90], the authors studied helium trapping in Cu, which has similar physical properties as Au. In this case blistering was observed after a fluence of 4.0×10^{17} cm^{-2}.

As is seen from Fig. 4.5(b), there is a negative volume offset, which is attributed to two effects. First, sputtering of the surface will result in material loss. Secondly, at low ion fluences helium ions can occupy existing crystal defects and inter-atomic positions without causing a substantial volume increase. The subsequent fluence increase leads to the creation of helium nanobubbles in the bulk gold. The formation of voids in metals due to He$^+$ ion bombardment is a well-known phenomenon [91–93]. After entering the crystal, an energetic He$^+$ ion creates vacancy-interstitial pairs. These vacancies can aggregate into bigger voids. Since helium is hardly solvable in metals, it is effectively trapped at open-volume defects and has a tendency to agglomerate into nano sized bubbles [94,95]. That leads to deformations, which cause the initial linear volume increase in the graph in Fig. 4.5(b). At these fluences (up to 4.2×10^{17} cm^{-2}) the volume change does not depend on the primary energy of the implanted ions.

As more helium ions are implanted, the cavities expand. The helium nanobubbles are highly over-pressurized. Up to a certain bubble size the excess pressure is relieved by loop punching. This bubble growth mechanism was first suggested by Greenwood et al. [96] and later on discussed by Evans [97]. As bubbles grow, several neighboring bubbles eventually create enough local stress to create a crack in the crystal and coalesce. At higher fluences the different stopping powers of gold and – high pressure – helium become relevant. At low energies helium is implanted in a near-surface region. This near-surface helium volume is an effective stopping material for more helium. As a result, a rapid expansion sets in until the bubble reaches the surface. The above described porous structure develops (Fig. 4.1(a)). At higher energies these processes occur deeper

in the material and more helium is incorporated, and as a result a blister develops. The blister formation mechanism by inter–bubble fracture, has been suggested by Evans [98]. However, also at these high energies helium will start to leak to the surface and the blister growth saturates. The steep part of the graph at 35 keV in Fig. 4.5(a) corresponds to the blister formation and growth process. At 25 keV that stage of the damage development was not resolved and only the volume of the already formed blister was measured.

We have made rough estimations of the pressure in the nanobubbles, and the pressure in the final blister at 35 keV. Not all of the incident helium is trapped in the bubbles: a part of it is backscattered, and some diffuses into the bulk or out of the material. SRIM-2011 [57] has been used to assess the percentage of backscattered helium. A gold slab with a thickness of 200 nm and 10^5 ions have been used in the calculations. According to these simulations 16% of the incident helium is backscattered at 35 keV. Attributing 4% to other loss mechanisms we used 80% of the fluence for our further calculations. Two approaches were used for the pressure estimation. In the first approach, the pressure was calculated using the virial equation of state:

$$PV_m/RT = 1 + B/V_m + C/V_m^2, \tag{4.1}$$

where P and T are the helium pressure and temperature respectively, V_m is the helium molar volume, R is the universal gas constant, B and C are the second and third virial coefficients. The values of B and C for He at room temperature were taken from [99] and [100]. This gives a lower estimate of 2.1 GPa for the pressure in the nanobubbles just before the start of the rapid expansion. Another assessment was done by applying a relation used by Evans [97], which is based on the work of Rowlinson [101]:

$$P[\text{Pa}] = 4.83 \times 10^7 exp\left(5.15 \times 10^{\text{-}2} \times \rho\right), \tag{4.2}$$

where ρ is the helium density in units of atoms/nm^3. In this case the calculated pressure is 6.1 GPa. Please note that these two estimates only give an idea of the order of magnitude of the He pressure inside the nanobubbles. As the bubbles grow in size the material can not support such high pressures, and the bubbles merge. In the case of the final blister grown with a primary energy of 35 keV, both models yield similar values of 437 MPa and 442 MPa, respectively.

4.5 Conclusions

Exposure to high He$^+$ ion fluences has a dramatic influence on a crystalline sample, which strongly depends on the energy of the incident beam. Sample modifications are mainly caused by helium implantation producing surface deformations. After the initial formation of nanobubbles filled with helium in the GPa pressure range different scenario's evolve. At low energies the bubbles quickly reach the surface and release the helium and a sponge-like surface develops. At high energies the initial nanobubbles form deeper in the material due to the greater range of the helium ions. Consequently, bubble coalescence leads to the formation of a large blister that continues to grow. The final size before the shell leaks depends on the primary energy and thus the implantation depth.

During irradiation with He$^+$ ions at normal beam incidence also a periodic nanopattern develops on the surface at room temperature. The pattern is oriented along the $\langle 1\bar{1}0 \rangle$ direction and its periodicity scales with the ion fluence with a coarsening exponent of 0.26 ± 0.01. The observed features do not coalesce and preserve their shape. An important observation is that the beam influences not only those areas, that are directly irradiated by the beam, but also the neighboring regions.

Ionoluminescence of NaCl

Helium ion microscopy has been used to investigate the ionolumines-cence of NaCl. A 35 keV, sub-nanometer He$^+$ ion beam was used to generate ionoluminescence. The interaction of ionizing radiation with alkali halides leads to the formation of various crystal defects, in partic-ular so-called color-centers. Their subsequent recombination with charge carriers leads to the emission of visible light. Broad peaks at 2.46 and 3.05 eV were measured. We have also investigated the dynamics of de-fect creation as a function of the beam scanning parameters (current and pixel spacing). The resolution and detection capabilities of ionolumines-cence in helium ion microscopy are sensitive to both sample properties and scanning parameters.

5.1 Introduction

A focused He^+ beam with a spot diameter of 0.4 nm [16] and an energy of several tens of keV is used for sample imaging in the helium ion microscope (HIM) [102]. The interaction of a He^+ beam with matter generates secondary electrons (SEs), backscattered He, and in some cases also photons. The latter is referred to as ionoluminescence (IL). It is similar to the cathodoluminescence (CL) phenomenon in scanning electron microscopy (SEM). The possibility for IL studies using HIM was previously demonstrated by Boden et al. [50] and Ogawa et al. [103]. Ionoluminescence is a result of the radiative relaxation of target electrons that have been excited by the incident beam. However, an ion beam can not only induce light emission, but may also cause target coloration due to the formation of specific types of defects, so-called color-centers [25]. Alkali halides are well-known to exhibit crystal coloration under ionizing radiation [104, 105]. A Frenkel pair of F- and H- centers is the simplest defect that is created during irradiation. The F- center is a well understood crystal defect that consists of a halide ion vacancy, filled with an electron, see Fig. 5.1 [105–107]. A neutral halide atom together with a neighboring halide ion forms an H- center [107, 108]. When an F- center loses an electron, an α- center is formed. It is basically a negative ion vacancy [109]. Another kind of primary defect is a self-trapped hole (V_k- center), which is a (halogen)$_2^-$ molecular ion that occupies two adjacent anion sites along the $\langle 110 \rangle$ direction [110–112]. Prior to F - H defect formation via electronic excitations, self-trapped excitons (STEs) are created [104, 107, 112]. An STE can be referred to as a V_k- center with a bound electron [111–114]. High defect concentrations lead to clustering and the formation of more complex defects.

In previous IL studies of alkali halides the luminescence peak position was found to vary between samples. There is no clear agreement on the nature of the observed light emission [115–118]. Although damage of alkali halides by various types of ionizing radiation has been studied for decades, the picture of the processes that occur is not complete. The combination of mechanical, thermal, electronic and optical processes induced by the irradiation complicates the interpretation of the observed results. In contrast to all prior IL work where broad ion beams were applied, we have used a sub-nanometer, 35 keV He^+ ion beam. Since HIM is a scanning technique, we have been able to investigate the formation of defects using various scanning parameters. A balance between the dif-
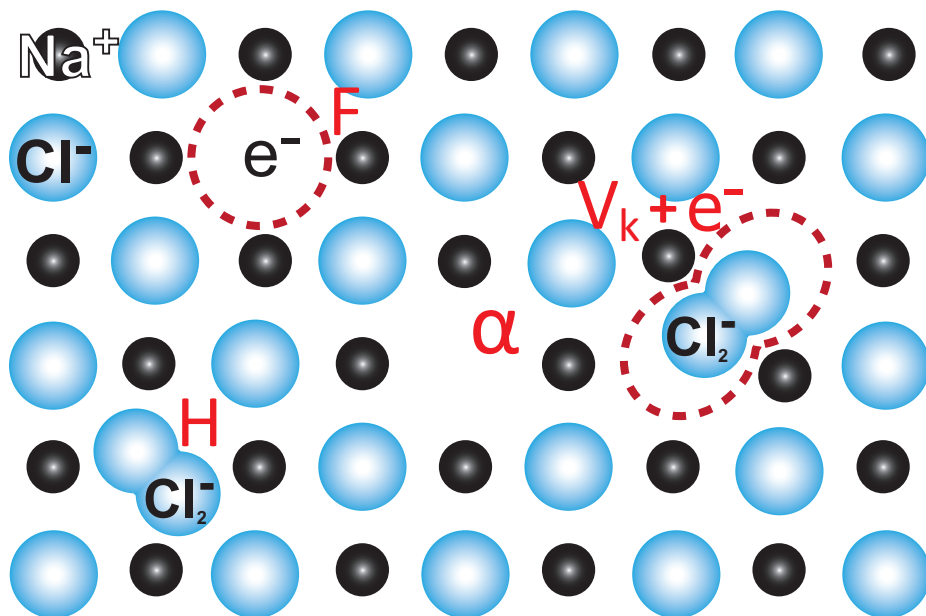
Figure 5.1: Model of the simplest defects in alkali halides: F-, H-, α-centers and a self-trapped exciton in an on-center configuration.

ferent defects that are created determines the IL emission behavior. We have also investigated the use of IL for imaging.

5.2 Experimental

The experiments were performed in an ultra high vacuum (UHV) Orion Plus Helium Ion Microscope from Carl Zeiss [53]. The samples were imaged simultaneously using two detectors. First, an image was formed by collecting SEs with an Everhart-Thornley (ET) detector. For IL imaging, the emitted photons were collected with a Gatan MonoCL4 Elite system. A retractable parabolic mirror was used to collect the light emitted from the sample. The mirror can be placed between the objective lens and the sample. An aperture in the mirror allows the He^+ beam to pass through and scan the sample. The collected light is then directed into a spectrometer housing by a light guide. A panchromatic IL image is recorded by collecting signal with a Hamamatsu Photomultiplier Tube (PMT) R943-02, with a spectral response in the 160-930 nm range. A CCD detector PIXIS:100 from Princeton Instruments was used for par-

allel spectrum acquisition. For that purpose the emitted light is sent through slits onto a diffraction grating. Then the angularly distributed spectrum is projected on the CCD. A spectrum can be acquired in the 200-1100 nm wavelength range.

The samples were commercially available NaCl crystals of 99.99 % purity. For the resolution test small NaCl crystals were grown from water solution on a highly ordered pyrolytic graphite (HOPG) substrate. In the experiments a He^+ ion beam with a primary energy of 35 keV was used. It was oriented perpendicular to the sample surface. The beam current was varied between 0.5 and 5.5 pA. The images were recorded with a 1024×1024 pixel resolution and 100 μs dwell time. The dependence of the total IL intensity on He^+ fluence was measured by integrating the IL signal with the PMT detector for 1.5 s per data point, including 0.2 s dead time, while the beam was scanning the sample with a 5 μs dwell time and 512×512 pixel resolution. Thus, each data point corresponds to the signal collected during a single full image scan. For the acquisition of each curve, a fresh, not previously irradiated area was selected. The collected spectra were background corrected and corrected for the MonoCL4 Elite optical system response. The chamber pressure during the measurements was in the low 10^{-9} mbar range. All measurements were performed at room temperature.

5.3 Ionoluminescence of NaCl

NaCl crystals exhibit ionoluminescence in HIM, see Fig. 5.2. In order to check the resolution and sensitivity that can be achieved in IL imaging, a sample with NaCl crystals on an HOPG substrate was used. The size of the NaCl crystals varies from several tens to a few hundreds of nanometers. A comparison of SE (left in Fig. 5.2) and IL (right in Fig. 5.2) images shows that a minimum crystal volume is required to detect an optical signal. The images presented in Fig. 5.2 were recorded at an ion dose of $5.6×10^{15}$ cm^{-2}. The smallest NaCl crystal, that was detected by IL at the given pixel spacing and ion dose, has a lateral size of 50 nm × 50 nm, and it is fair to assume that the crystal also has a height of approximately 50 nm. We also observed that the minimum detectable crystal size depends on the ion dose that is applied during imaging. However, there is an upper limit for the allowed ion dose in each particular experiment. At
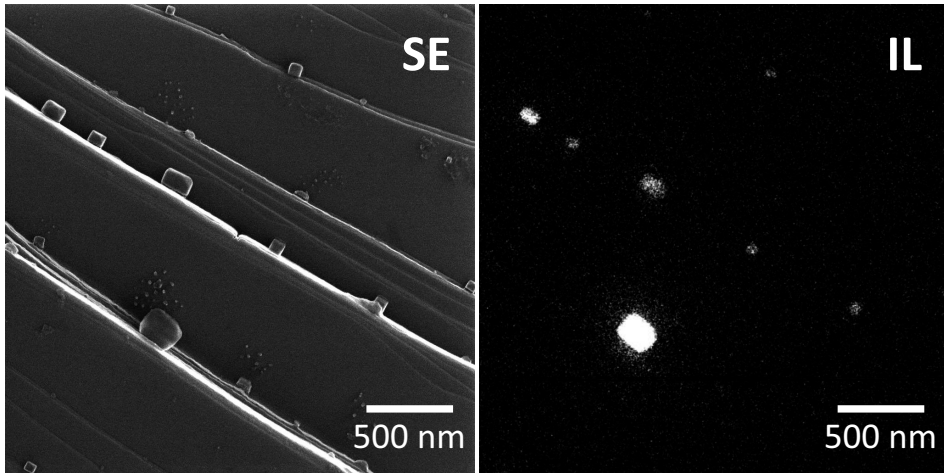
Figure 5.2: SE (left) and IL (right) images of NaCl crystals on an HOPG substrate. The strength of the IL signal depends on the crystal volume. The smallest detectable crystal has a size of $50\,\text{nm} \times 50\,\text{nm}$. The beam primary energy is $35\,\text{keV}$ and current is $2.5\,\text{pA}$. Field of view is $2.7\,\mu\text{m}$.

high ion fluences, imaging may become destructive (see Chapter 4) and severely modify the small crystals, even before they are detected with IL.

A characteristic spectrum of the emission from NaCl crystals is shown in Fig. 5.3. The spectrum was obtained by scanning a $50\,\mu\text{m} \times 50\,\mu\text{m}$ area of a NaCl single crystal using a $35\,\text{keV}$ He^+ beam. Two main emission bands can be discriminated at $2.46\,\text{eV}$ and $3.05\,\text{eV}$. We consider the small deviations from the fitted curve to be due to the spectrum correction for the system non-linear response.

Luminescence at about $2.4\text{-}2.45\,\text{eV}$ was previously observed, but its origin has not been exactly identified yet [115, 118–120]. The authors of Ref. [118] attribute it to possible water or oil vapor contamination in the chamber vacuum. The vacuum in their described experiments was in the 10^{-7} mbar range. This reasoning can be excluded in our experiments due to the UHV environment with a pressure in the low 10^{-9} mbar range in the main chamber and the absence of oil pumps. Ukai et al. [119] proposed a bi-exciton emission mechanism, which was later disproved by Chandler et al. [121]. The authors of Ref. [121] have also shown that the observed emission is an intrinsic process. Aguilar et al. [115] suggested that it is an M‑like emission, caused by the transition between high and low excited states of STEs. However, previous experimental and
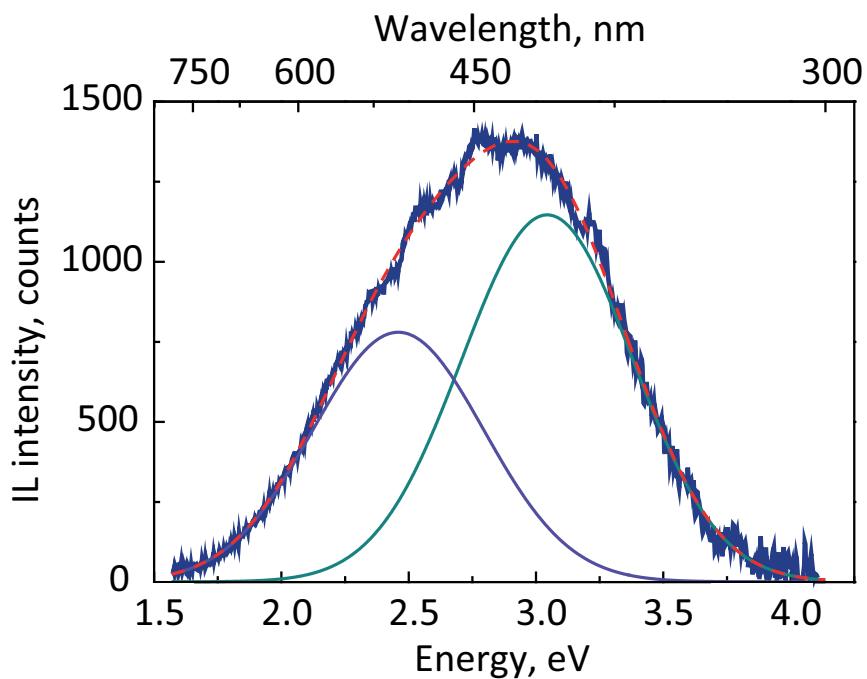
Figure 5.3: Ionoluminescence spectrum of a NaCl crystal (—), fitted with two Gaussian peaks. The peaks are centered at 2.46 eV and 3.05 eV.
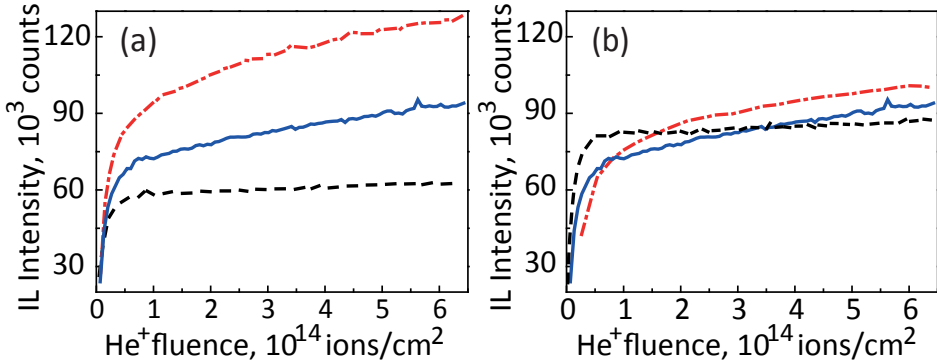
Figure 5.4: (a) IL signal intensity versus He$^+$ ion fluence at various currents, but at a fixed 36.7 nm pixel spacing. The He$^+$ beam currents are 1.9 pA (- - -), 2.5 pA (—), and 2.8 pA (-·-). (b) IL intensity versus ion fluence at various pixel spacings and at a fixed 2.5 pA beam current. The pixel spacings are 64.6 nm (---), 36.7 nm (—), and 18.5 nm (-·-). In all cases the He$^+$ beam energy is 35 keV.

theoretical work has revealed that this transition occurs non-radiatively within a few ps after excitation, even at cryogenic temperatures [122–124]. Gorobets et al. [125] ascribe the peak to recombination of an electron with a V_F-center (which is a hole next to a cation vacancy). We believe that the last assignment is the most plausible explanation of the observed peak. This is particularly supported by the fact that the ion beam irradiation will result in knocking out neutral Na atoms and leave V_F- centers behind.

In literature the band around 3.05 eV is referred to as α-emission [126–129]. This emission is attributed to the recombination of an F-center electron with a hole (a V_k- center in the end) [109, 125, 129, 130]. This process is equivalent to the recombination luminescence of an STE perturbed by a neighboring α- center [128–130].

To study the dynamics of defect creation, we recorded IL intensity changes as a function of ion fluence. Typical curves at various beam parameters are presented in Fig. 5.4. The curves can be divided in two parts. The first one is an initial fast increase. In the second part, the signal either stagnates or slowly increases. The details of both parts depend on how the ion dose is delivered to the sample. Figure 5.4(a) shows curves that were obtained at different beam currents, but with the pixel spacing fixed at 36.7 nm. For a current of 1.9 pA the IL signal shows
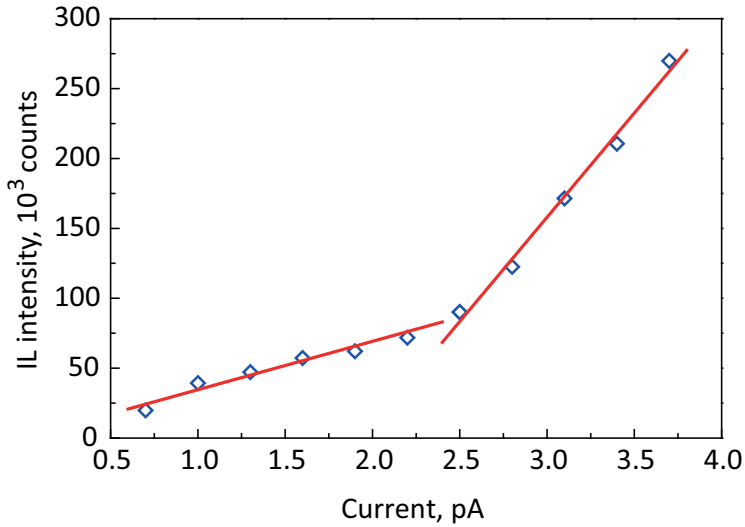
Figure 5.5: IL intensity versus the He$^+$ beam current at a fixed pixel spacing of 36.7 nm. The IL intensity values are all taken at the same He$^+$ fluence of 5×10^{14} cm^{-2}. The He$^+$ beam energy is 35 keV.

a fast stagnation behavior (- - - in Fig. 5.4(a)). At a higher current of 2.8 pA, after an initial rapid increase, the IL intensity increases slowly with increasing helium fluence (- ·- in Fig. 5.4(a)). A beam current of 2.5 pA yields a transition between the stagnating and creeping regimes discussed before (— in Fig. 5.4(a)). The IL signal as a function of fluence at various pixel spacings and at a fixed beam current of 2.5 pA, is shown in Fig. 5.4(b). For a large pixel spacing of 64.6 nm the IL signal rapidly stagnates (- - - in Fig. 5.4(b)). For the case of a small pixel separation of 18.5 nm, the intensity increases slower initially, but keeps on increasing for higher fluences (- ·- in Fig. 5.4(b)). At an intermediate pixel spacing of a 36.7 nm, transitional behavior is observed (— in Fig. 5.4(b)). Thus, in the case of a low current density, the signal stagnates fast, while at high current densities it continues to grow.

As can be seen from Fig. 5.4(a), the ultimate IL intensity level grows with increasing beam current. In Fig. 5.5 the IL intensity is plotted versus ion current for a fixed pixel spacing of 36.7 nm and a fluence of 5×10^{14} cm^{-2}. The data can be fitted with two linear functions. Initially the IL signal increases with beam current at a rate of 35×10^3 counts/pA. At a certain current the behavior changes and a more rapid increase

with a rate of 150×10^3 counts/pA occurs. This transition happens at approximately the same beam current value (~ 2.5 pA) where the fluence dependence switches its behavior in Fig. 5.4(a).

To verify which emission process is influenced by the variation of the scanning parameters, we recorded fluence dependencies with filters placed in the beam path. We used a "red" filter (600 - 700 nm) to track the intensity of the 2.46 eV band, and a "blue" filter (400 - 500 nm) to observe the changes in intensity of the 3.05 eV band. The curves were recorded at a fixed pixel separation of 46.2 nm and for two different currents: 2.2 pA and 5.9 pA, and are plotted in Fig. 5.6. Due to the difference in the transmittance of the filters and increase of the IL intensities with the beam current, the curves were normalized to the intensity value at a fluence of 5×10^{14} cm^{-2} to allow a clear comparison of the shapes. The general shape of the 2.46 eV band is not affected by the beam current (red solid and dashed lines in Fig. 5.6). That supports the assignment of V_F- centers as the source of the 2.46 eV emission. However, a clear change in the behavior of the IL signal is observed for the blue 3.05 eV band, which corresponds to α-emission. The fluence dependence switches from "stagnation" to "creep" with increasing beam current (blue solid and dashed lines in Fig. 5.6). Therefore, we conclude that α-emission is responsible for the changes in the behavior of the IL signal.

We assume that the intensity of the 3.05 eV band is proportional to the concentration of F- centers. During ion bombardment F - H Frenkel pairs are created as a result of both electronic and atomic excitations. These two processes can not be easily discriminated. The F- center can be created by direct displacement of a halide ion and the trapping of an electron in the formed vacancy. However, color-center production is more effective via electronic excitations [131, 132]. A model for the creation of F - H pairs due to electronic excitations was suggested by Hersh [104] and Pooley [107], and was extensively studied later [112, 122, 133, 134]. During irradiation a Cl$^-$ ion can lose an electron forming a free exciton. A free exciton rapidly transforms into a self-trapped exciton as a result of the bonding of the Cl atom to a neighboring Cl$^-$ ion. Subsequently, an STE in an off-center configuration acts as precursor for the F - H pair formation [112, 133]. The radiationless transition of an off-center STE from an excited state can provide sufficient energy for the displacement of a Cl$_2^-$ ion and the formation of a nearest-neighbor F - H pair. This process of STE conversion into an F - H pair is effective at room temperature [133, 135]. While H- centers are mobile in NaCl already above 80 K [136],
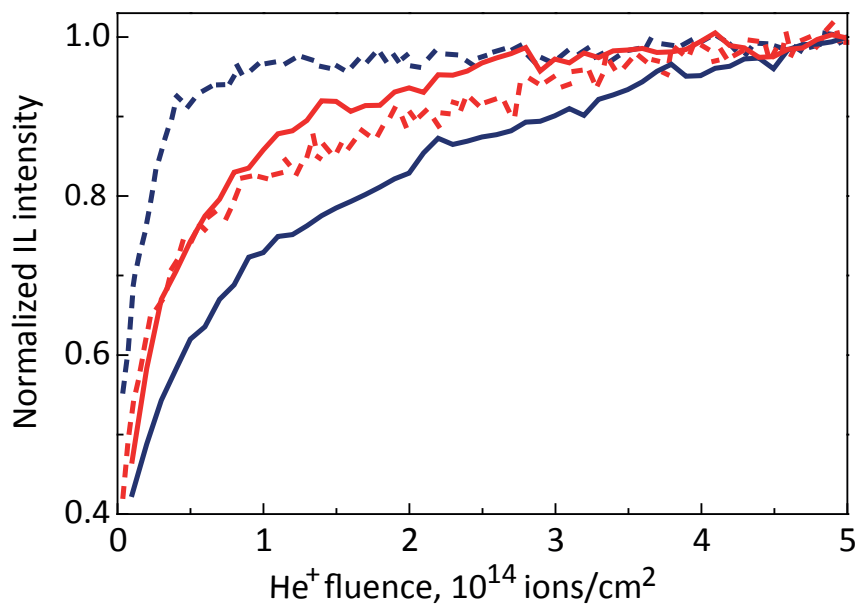
Figure 5.6: Normalized IL intensities of the 2.46 eV and 3.05 eV bands versus He$^+$ fluence at fixed pixel spacing of 46.2 nm. Blue dashed and solid lines are intensities of 3.05 eV band at 2.2 pA and 5.9 pA beam currents respectively. Red dashed and solid lines refer to a 2.46 eV band at 2.2 pA and 5.9 pA currents respectively.

F- centers are mobile only above $500\,\mathrm{K}$ [137]. Thus, the dynamics of H- centers is key in interpreting the observed results.

Both the ion fluence and current density were previously demonstrated to influence F- center production efficiency in experiments irradiating LiF with heavy swift ions [138, 139]. As long as the current density is low and the period between two arriving ions is relatively long, each cascade event can be considered individually. When the current density increases, the events temporally overlap, and the processes that occur are not independent anymore. When the cascade events start to overlap, the high H- center concentration, combined with the high mobility of such centers, increases the probability for the formation of a Cl_2 molecule [108, 140–142]. The recombination rate between an F- center and Cl_2 is much smaller than that between F- H centers. Due to the reduced concentration of H- centers that can recombine with F- centers, the concentration of F- centers is efficiently increased and we observe an enhancement of the IL signal. A similar effect of enhanced F- center creation was observed in the case of LiF [140, 141]. Dislocations are also effective traps for H- centers [126, 142] and are able to further enhance F- center formation. However, we do not expect the appearance of dislocations at the applied fluences [72].

A short distance between neighboring pixels gives an effective overlap of the volumes containing defects, and makes for a more complex situation. Defects created at the current pixel impact site interact with those from the previous one. H- centers from a previous pixel can diffuse into the interaction volume of the next pixel, thereby changing the balance between F- and H- centers and increasing their recombination rate. This suppresses the initial increase of the IL signal.

Figure 5.7 provides an overview of the different regimes at various beam currents and pixel separations. The experimental curves were fitted using the Weibull growth model [143]. The growth rate equal to 1 was chosen as a criterion for discrimination between the stagnation (large than 1) and creep (smaller than 1) regimes. The stagnation ($\triangle$) and creep ($\circ$) behaviors are indicated in the plot according to this criterion. Grey and red hashed areas indicate the corresponding regimes. The area corresponding to the transition between the regimes is marked by a blue cross pattern. It is clear that with an increase of the beam current, the transition between different regimes occurs at a larger pixel spacing. At higher currents the diameter of the interaction volume increases and ex-
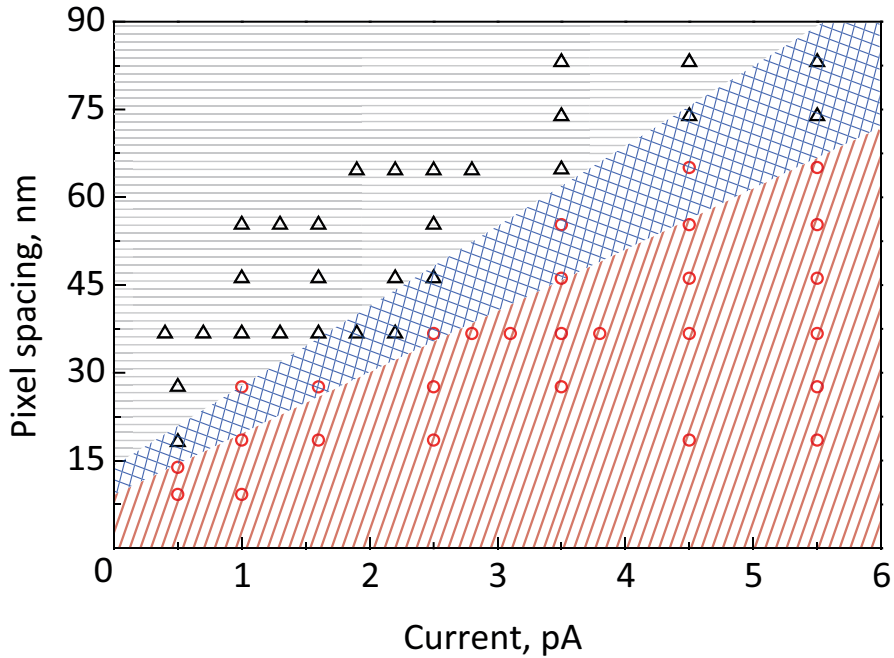
Figure 5.7: Diagram of the IL signal behavior as a function of the beam current and pixel spacing. Stagnation type behavior of the curve is indicated by $\triangle$, and creep is indicated with $\circ$. Grey and red hashed areas indicate the stagnation and regimes accordingly. Blue cross pattern indicates the area which corresponds to the transition between the regimes. The He$^+$ beam energy is 35 keV.

plains the overlapping of the interaction volumes that occurs at larger pixel separations.

5.4 Conclusions

In conclusion, we have demonstrated the possibility to use HIM for an optical investigation of irradiation induced damage in ionic crystals. The IL emission from NaCl that is induced by a focused He$^+$ beam consists of two bands at $2.46\,\text{eV}$ and $3.05\,\text{eV}$. The emission is a result of the recombination of the charge carriers with color-centers that are generated namely, F and V$_F$. The defect formation depends on beam scanning parameters such as pixel spacing and ion beam current. In particular, F- center formation is sensitive to the details of the irradiation conditions and is responsible for the luminescence. This is the result of an overlap of the interaction volumes of neighboring pixels in combination with a difference in mobility of the different types of crystal defects.

Creation and physical aspects of luminescent patterns

The helium ion microscope provides a sub-nanometer size He$^+$ ion beam which can be employed for materials modification. We demonstrate how material properties can be tuned in a helium ion microscope with very high precision using as an example the modification of the luminescence properties of a sodium chloride crystal. Although the beam size is extremely small, the actually affected sample volume is much bigger due to developing collision cascades. We have directly measured the diameter of the interaction volume of the 35 keV He$^+$ beam with a sodium chloride crystal using ionoluminescence. The experimental results are compared to SRIM simultions and calculations of the point spread function.

6.1 Introduction

Local modification of material properties is an interesting topic since it gives an opportunity to tune the material parameters for one's needs and by doing so design various devices. In this context the helium ion microscope (HIM) is an attractive tool. It provides a He$^+$ ion beam with a spot size of 0.4 nm [16]. HIM has been successfully employed for surface patterning and nanofabrication [67–71, 102, 144–148]. Here, we demonstrate how HIM can be applied for precise modification of bulk material properties.

Mainly secondary electrons (SEs) are used for imaging. We use SE throughout this chapter for those electrons, which are generated as a result of an ion impact, actually make it to the surface and are emitted into the vacuum. In addition to SEs and backscattered He signals typically used in HIM, also photon generation and detection is possible for certain materials [50, 103]. This phenomenon is called ionoluminescence (IL). The ion beam is able to not only induce light emission from the sample, but can also change the luminescence properties of the material. We employ both aspects for pattering of luminescent structures and direct visualization of the beam-matter interaction volume.

Irradiation of alkali halides with ionizing radiation causes defect formation and subsequent crystal coloration [104, 105]. The influence of a He$^+$ ion beam on NaCl in terms of ionoluminescence has been studied previously (see Chapter 5). Light emission under the influence of an ion beam is the result of recombination of the created color-centers (in particular F-centers) with charge carriers. In NaCl F-centers are chlorine ion vacancies filled with one electron. They are created both by direct nuclear collisions and via electronic excitations [131,132]. Generation of color-centers with an ion beam gives local control over the defect density.

6.2 Experimental

The experiments were performed in an ultra high vacuum (UHV) Orion Plus Helium Ion Microscope from Carl Zeiss NTS [53] at room temperature. In the standard HIM imaging mode, an image is created by collecting SEs with an Everhardt-Thornley (ET) detector. An IL image can be recorded simultaneously by collecting the emitted photons with a Gatan MonoCL4 Elite system. The system is equipped with a Hama-

matsu Photomultiplier tube (PMT) R943-02 utilized for panchromatic IL imaging, and a CCD detector PIXIS:100 from Princeton Instruments for parallel spectrum acquisition. Further details on the system configuration can be found in the Experimental chapter.

The primary energy of the He^+ ion beam was 35 keV, the beam was oriented perpendicularly to the surface. In the present experiments the beam current has been varied between 0.5 and 6.6 pA. All images were acquired simultaneously, using the ET and PMT detectors. The chamber pressure of the baked sample chamber was in the low 10^{-9} mbar range during all measurements.

Additional cathodoluminescence (CL) measurements were performed on a Zeiss ULTRA55 field-emission scanning electron microscope (SEM) equipped with a Gatan MonoCL3 system.

The samples were commercially available NaCl crystals with 99.99 % purity from Merck Millipore and NaCl cell windows from Sigma-Aldrich, which were cleaved and cut to the needed size.

6.3 Results and Discussion

We created a luminescent pattern on a NaCl crystal by implantation of roughly 6500 helium ions per pixel using a 20 nm pixel separation and irradiating only a predefined area. Later, the patterned area was imaged using ∼1600 ions per pixel (4.5 pA beam current and 58 μs dwell time) and the same pixel separation. The obtained panchromatic IL and SE images are shown in Fig. 6.1 (a) and (b) respectively. The IL image clearly shows the created pattern (Fig. 6.1 (a)). The SE image in Fig. 6.1 (b) does not show any surface damage. The vague contrast in the SE image is the result of charging effects.

The thus formed structures luminesce not only under ion irradiation. A similar pattern using identical irradiation conditions had been created in a cleaved NaCl cell window and was then investigated by CL using a SEM. A panchromatic CL image of the pattern is shown in Fig. 6.1(c). The bright spots in the image are small NaCl crystal fragments on the surface which are the result of poor crystal cleavage.

Although an energetic ion beam preserves its shape in the surface vicinity, the beam profile widens deeper in the material due to nuclear collisions [102]. Additionally, the actual interaction volume relevant for IL is not restricted by the size of the ion induced collision cascades. The gen-
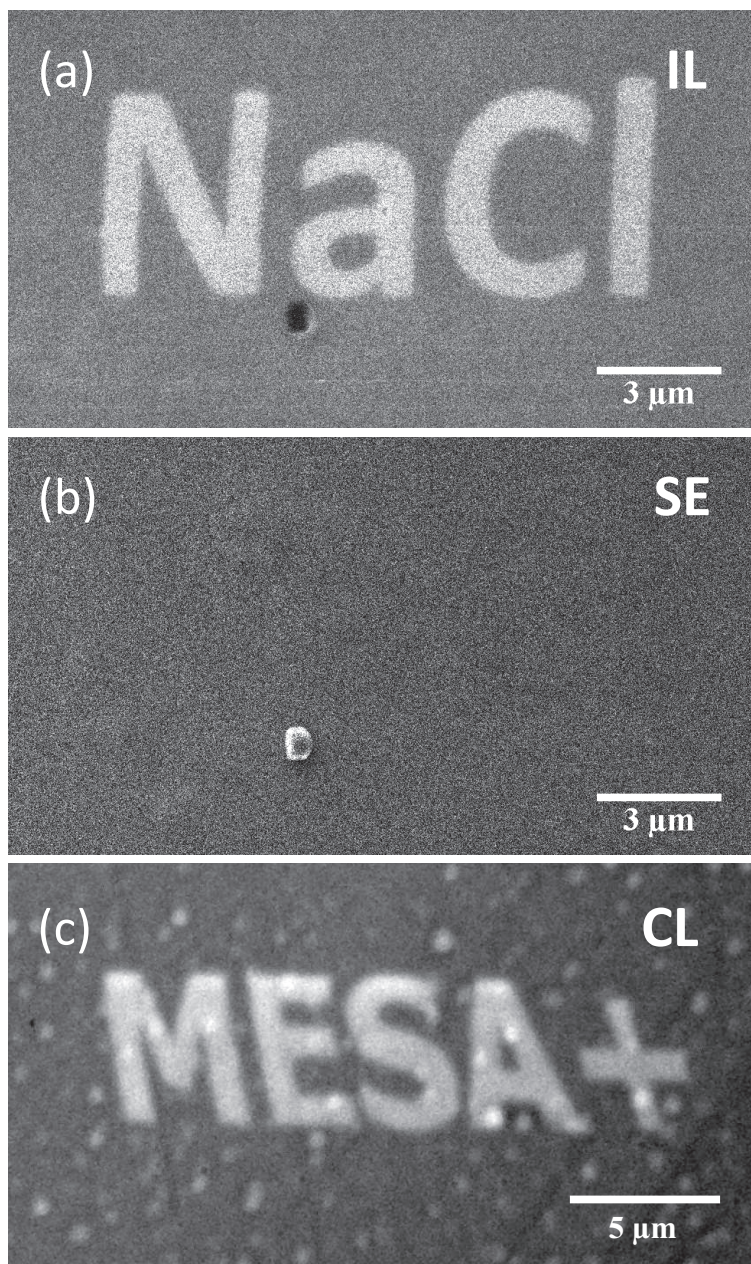
Figure 6.1: (a) and (b) IL and SE images of a pattern on a NaCl crystal. The He$^+$ beam energy is 35 keV. FOV is 18 μm×10 μm. (c) Panchromatic CL image of a pattern created on a cleaved NaCl crystal in HIM. FOV is 25 μm×14 μm.

eration of electrons also has to be taken into account. For example, the width of the letter "*l*" in the pattern in Fig. 6.1 (a) is ∼1.16 μm, whereas, the desired width was only 1.0 μm. The minimal possible lateral pattern size is limited by the beam interaction volume with the material. This gives rise to the discrepancy in the desired and actual line width of the pattern.

While SE images in HIM provide a high surface sensitivity due to the short electron escape depth [31], the IL signal contains bulk information. The IL images are a projection of the concentration of light emitting centers on the sample surface. Therefore, IL imaging allows the direct visualization of the beam interaction volume diameter. Since the ion beam diameter is below 0.5 nm we can neglect the actual beam profile and treat the situation as a single point impact. An example of the direct measurement of the lateral size of the interaction volume of the He^+ beam with the NaCl crystal is presented in Fig. 6.2 (a). We created an array of single pixel impacts applying different amounts of He^+ ions by varying the ion beam current and dwell time ranging from 0.8 pA to 6.6 pA and 100 μs to 4000 μs, respectively. Later the patterned areas were imaged with a resolution of 1024×1024 pixels, a beam current of 0.5 pA and a dwell time of 58 μs, corresponding to ∼200 He^+ ions per pixel. In Fig. 6.2 (a), each of the four bright spots in the IL image is a single pixel ion beam impact, but after different amounts of helium were implanted. In the shown example the doses were: 7340, 14680, 22020 and 29360 ions per pixel starting from the top left to the lower right corner. Using Fiji [149] the spot radii were extracted from the images for a deposited charge ranging from 0.2 fC ($1.2×10^3$ ions) to ∼20 fC ($1.2×10^5$ ions). The IL intensity profiles were radially averaged and could be fitted by Gaussian function with high accuracy (Fig. 6.3). The values of the spot radii were taken at the gray level equal to the mean noise level plus twice the standard deviation of the noise. The obtained dependence of the spot radius on the amount of incident ions is shown in Fig. 6.2 (b).

The central part of the IL spot is difficult to predict and describe due to the high defect concentration. The defects may interact and cluster and thereby affect the produced IL signal in a hard to predict way (see Chapter 5). The outer part of the IL profile corresponds to a low defect concentration and should show a linear response to the increase of the ion dose. We therefore assume, that the edge of the IL spot profiles can be described by a Gaussian function with the center at the point of
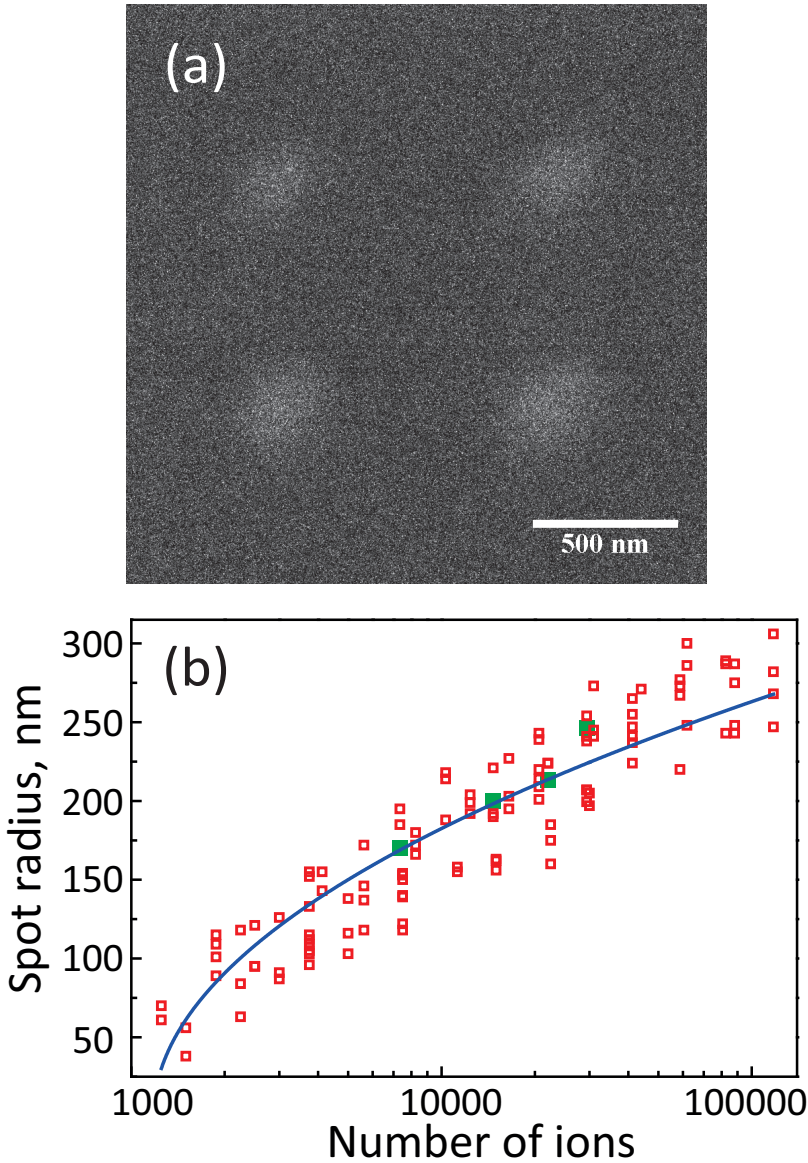
Figure 6.2: (a) Panchromatic IL image of a NaCl crystal surface after a "four-pixels" pattering with a $35\,keV$ focused He$^+$ beam. Beam current was $4.7\,pA$. Dwell times, moving by rows from top left corner to the lower right corner: $250\,\mu s$, $500\,\mu s$, $750\,\mu s$, and $1000\,\mu s$. For imaging current of $0.5\,pA$ and dwell time of $58\,\mu s$ were used. (b) Dependence of the radius of the luminescent area on the amount of the incident He$^+$ ions. The beam currents were $0.8\,pA$, $1.2\,pA$, $4.7\,pA$ and $6.6\,pA$. The dwell time was varied from $100\,\mu s$ to $4000\,\mu s$. Green squares correspond to the data points from the measurement presented in (a). The blue solid line is the fit by the function from Eq. (6.2)
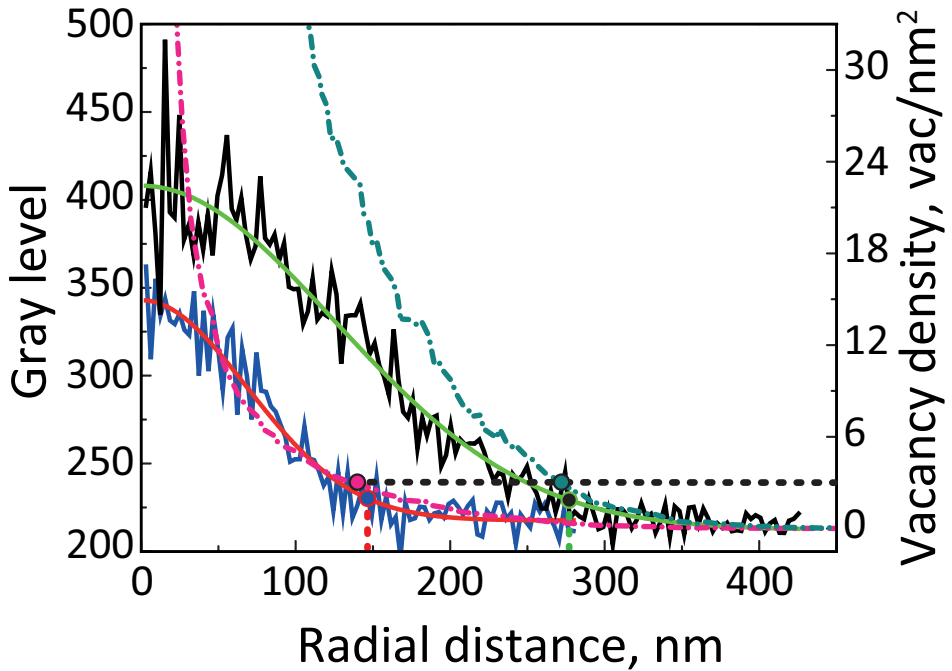
Figure 6.3: IL intensity radial profiles of single pixel impacts of a 35 keV focused He$^+$ beam into NaCl. Number of implanted He$^+$ ions: 7500 ions (blue line) and 58750 ions (black line). The experimental profiles are fitted with Gaussian curves. The dashed vertical lines indicate the spot radius at the gray level equal to the mean noise level plus twice its standard deviation. The pink and cyan dash-dotted lines are vacancy density profiles from the SRIM simulation for 7500 ions and 58750 ions respectively. The black dashed horizontal line indicates the radius which corresponds to 3 vac/nm^2.

incidence, and a common standard deviation. We can write the following expression:

$$\frac{\alpha I}{\sigma} exp(-\frac{r^2}{2\sigma^2}) = S \tag{6.1}$$

where I is the amount of incident ions, r is the spot radius, σ is the standart deviation, α is a scaling constant, S a threshold value to obtain a measurable IL signal. From this expression we arrive at the following dependence of the spot radius on the ion dose:

$$r = \sigma\sqrt{2lnI - B} \tag{6.2}$$

where $B = 2ln(\sigma S/\alpha)$.

The experimental data was fitted with Eq. (6.2). The obtained fit is presented in Fig. 6.2 (b) as a blue line. The σ value extracted from the fit is 88.3±1.5 nm. It reflects the distribution of the defects generated by the ion beam (or, to be more precise, of the emitting centers).

The interaction of ions with matter and the associated defect generation is typically simulated using SRIM [57]. According to SRIM the calculated radial range of 35 keV He$^+$ ions in NaCl is 175 nm. However, this is a fixed value which does not depend on the ion dose. To predict the dose dependence we simulated the vacancy distribution. The SRIM output in a form of the 3D vacancy distribution contains a projection of the vacancies on a plane which is perpendicular to the surface. However, we are interested in a cross-section of the projection on the sample surface. To extract this cross-section we processed the full collision data containing details about the generated recoils. The thus obtained vacancy profile differs from the experimental spot profile (Fig. 6.3). It has an extremely high defect concentration at the point of incidence which rapidly decreases with increasing radial distance.

We used the vacancy distribution profiles obtained from SRIM to estimate the minimal defect concentration needed for the generation of a measurable IL signal and to predict the spot radius dependence on the ion dose. The vacancy profiles were calculated for different ion doses. From these profiles we extracted the radial distances which correspond to a fixed amount of vacancies (Fig. 6.3). The thus obtained correlation between ion dose and spot radius is compared to the experimental data in Fig. 6.4 (green circles and line – SRIM simulation, and red squares – experiment). The SRIM simulation predicts the correct shape of the interaction volume radius dependence of the ion dose. The number of
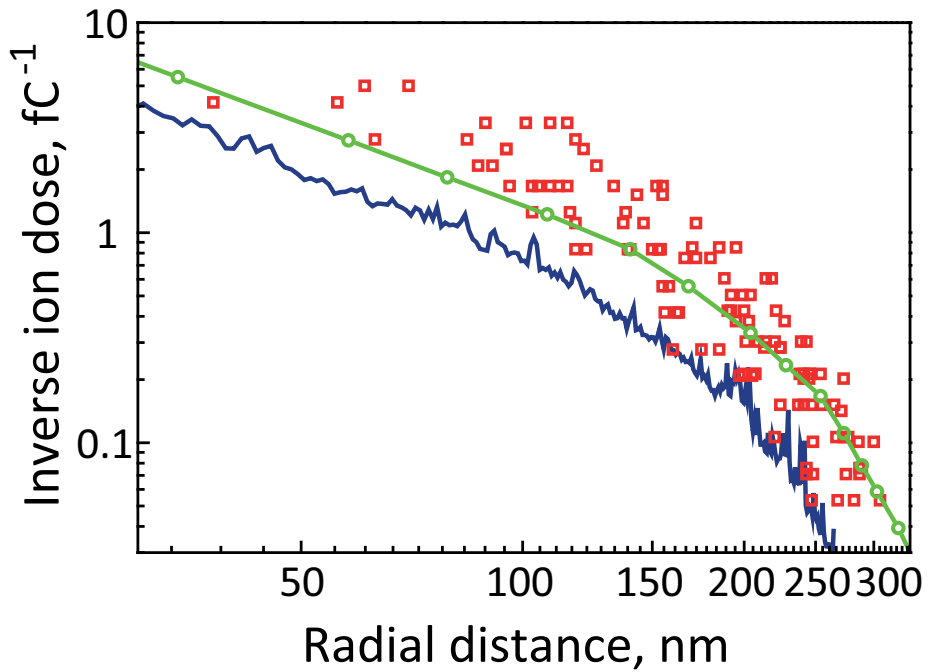
Figure 6.4: Comparison of the SRIM simulation (green circles and line) and calculated point spread function (solid blue line) with the experimentally measured radius of the interaction volume (red squares).

vacancies was varied to obtain the best fit to the experimental data. The best fit was obtained for $3\,\text{vac}/\text{nm}^2$, which corresponds to about 17 vacancies per pixel. Please note, that these vacancies are distributed in the direction perpendicular to the surface over the interaction volume. Also note that although we use a low ion dose for pattern imaging, in each pixel the IL signal is collected from a volume which is bigger than the defined pixel size. The experimentally measured profile is a convolution of the actual defect distribution profile with the probe profile. The influence of the non-zero size of the probe is more significant at low ion doses where the spot radii is small. Thus, the IL spot radius is overestimated at these doses (see Fig. 6.2 (b).) At high ion doses SRIM overestimates the radial distance since it does not take into account helium implantation. Implanted helium acts as efficient trap for incoming helium ions, and in this way affects and reduces the average ion range.

Winston et al. [150] have combined SRIM and electron generation using a Monte Carlo method for simulation of the point-spread function (PSF) in HIM. The PSF provides a spatial distribution of the energy dissipation for a single point impact [151, 152]. The software developed by Winston et al. was used to simulate the impact of a $35\,\text{keV}$ He^+ beam on a NaCl crystal. We used 10^5 helium ions and a $750\,\text{nm}$ thick NaCl slab for the simulation. The simulation describes the dissipated energy per volume unit and ion as a function of the radial distance from the impact point. To be able to compare the simulation with the experimental results, the units were converted into the inverse ion dose [fC^{-1}]. To do so we used the sum of the electronic and nuclear stopping powers which were extracted from the SRIM simulation at several depths and averaged within $25\,\text{nm}$ thick slabs. Due to the bulk nature of the IL signal we were interested in the dissipation of the energy over the whole slab. The PSFs for all $25\,\text{nm}$ slabs were then summed up to obtain the projection of the total dissipated energy on the surface. This is different from the simulation in [150] where the PSF was extracted only for a single thin sample layer in direct vicinity of the surface. The comparison of the simulated PSF with the experimental results is shown in Fig. 6.4 (blue solid line). Two Gaussians are the main contributions into the PSF [150, 151]. The first term smears out with increasing depth as a result of the increase in nuclear stopping power. The bigger importance of this term in our calculation for a bulk like sample is the reason for the difference in the shape of the present simulation and the one in Ref. [150]. The PSF function clearly underestimates the spot radius. This happens since the PSF cal-

culation does not take into account the generation of recoils. According to the SRIM simulation nearly half of the generated vacancies are created by the recoiling target atom. This influences the spatial distribution of the energy dissipation. Moreover, we do not observe a significant difference in shape between the PSF function and the curve obtained from SRIM. This is because of the short electron mean free path of only 1-2 nm in NaCl [153, 154]. Unfortunately, we do not have experimental data for radial distances smaller than 40 nm. For the corresponding small ion doses the IL signal becomes hardly distinguishable from the background. On the other hand, extremely high ion doses could also not be applied in order to avoid significant sample modifications due to material sputtering and helium implantation [155]. Additionally, the charging of the sample surface leads to the deflection of the beam at high ion doses.

6.4 Conclusions

We have directly visualized and measured the lateral size of the interaction volume of a 35 keV He$^+$ beam with NaCl. The characteristic length scale of the radius of the volume containing emission centers was found to be 88.3±1.5 nm. SRIM and PSF simulations were used to predict the dependence of the interaction volume radius on the ion dose. Although these are simplified models for the damage simulation and do not take into account defect interaction and diffusion, both lead to a good agreement with the experimental data. The SRIM simulation predicts a surface projected defect concentration of 3 vac/nm^2 at the edge of the luminescent spots visualized with IL. The PSF calculation underestimates the values of the spot radius since it does not consider generation of the recoils. Moreover, in the material of interest, the PSF calculation does not provide additional information due to the short electron mean free path. We have further demonstrated the possibility to locally change material properties with very high precision in HIM. In the current work we influenced the luminescence properties of the material, but possibly magnetic, electronic and other properties can be modified too.

7
Ionoluminescence of semiconductor materials

We have studied ionoluminescence of semiconductors induced by a subnanometer He$^+$ beam. Several types of semiconductor samples were investigated: bulk materials, nanowires and quantum dots. All samples were found to exhibit ionoluminescence. However, the ionoluminescence signal rapidly degrades under the ion irradiation. The signal degradation was found to depend not only on the sample's composition, but also on its size. The ionoluminescence emission spectra were recorded and emission peaks identified.

7.1 Introduction

Helium ion microscopy (HIM) is known for its high resolution imaging capabilities [15,102]. Several signals for sample analysis can be obtained in HIM: secondary electrons (SE), backscattered He and also photons. Upon entering a sample, the beam initially loses its energy mostly through inelastic collisions with the sample's electrons, without a significant change of the propagation direction. Thus, in the vicinity of the surface the shape and size of the focused beam is conserved, resulting in a narrow interaction volume. Since only the SEs that are generated in the first few nm are able to escape and be detected, the probe size remains small. This provides an ultimate lateral resolution and high surface sensitivity [156].

Ionoluminescence (IL) is the phenomenon of photon emission induced by ion irradiation. IL is similar to the cathodoluminescence (CL) technique which is widely used in mineralogy and is also applied to characterize semiconductor materials. The high resolution capabilities of HIM were expected to give a benefit in resolution of IL imaging over CL imaging. However, the ion beam irradiation introduces defects at a relatively high rate, significantly influencing the luminescent properties of the materials (see Chapter 5). Previous attempts to investigate IL from bulk semiconductors using HIM were not successful [50]. The authors of Ref. [50] report that no detectable signal was obtained from a series of direct band-gap semiconductor samples. However, later the same authors demonstrated IL of a GaN layer on sapphire [157]. The characteristic band-gap and yellow emission were observed.

In this chapter we describe the influence of the He$^+$ beam on the IL emission of semiconductor materials. Furthermore, we explore the possibility of employing IL for semiconductor samples characterization. For this purpose samples of various compositions and sizes were examined.

7.2 Experimental details

The experiments were performed in an ultra high vacuum (UHV) Orion Plus Helium Ion Microscope from Carl Zeiss NTS [53] at room temperature (RT). In the standard HIM imaging mode, an image is created by collecting SEs with an Everhart-Thornley (ET) detector. An image can also be simultaneously recorded by collecting the emitted photons with a Gatan MonoCL4 Elite system. The system is equipped with a Hama-

matsu Photomultiplier tube (PMT) R943-02 utilized for panchromatic IL imaging, and a CCD detector PIXIS:100 from Princeton Instruments for parallel spectrum acquisition. The IL spectra were corrected for the system optical response. In several cases spectra were not corrected because of the low intensity of the signal. In these cases, the non-linearity of the correction curve introduces additional noise to the signal and leads to the appearance of false peaks. If no correction for the instrument response was made it is noted in the text.

The measurements were done with a primary ion beam energy of 35 keV (if not specified otherwise). The beam was oriented perpendicular to the surface. In the present experiments we used beam currents from 0.5 to 290 pA. The images were acquired simultaneously, using the ET and PMT detectors. The total IL intensity as a function of He^+ fluence was measured by integrating the IL signal with the PMT detector for 1.5 s per data point, including 0.2 s dead time, while the beam was scanning the sample with a 5 μs dwell time and 512×512 pixel resolution. Thus, each data point corresponds to the signal collected during a single full image scan. The background of the signal was subtracted from the curves. The chamber pressure during the measurements was in the low 10^{-9} mbar range.

Several types of semiconductor materials were tested. Bulk semiconductor samples were a 4.5 μm thick Si-doped GaN film on sapphire, an InP wafer and an S-doped GaP wafer. Semiconductor nanowire (NW) samples were GaP-GaAs overgrown NWs [158,159] and GaP NWs with a silicon shell [160]. The NWs were transferred on a Cu TEM-grid. Semiconductor quantum dots (QDs) samples were Lumidot^{TM} CdSe core-type QDs from Sigma-Aldrich. Three different types of QDs with different emission peaks have been used. The QDs were deposited onto an Al substrate from a toluene solution.

7.3 Bulk semiconductors

Several bulk semiconductor samples were investigated: Si-doped GaN film on sapphire, InP and S-doped GaP wafers. The highest IL signal from all investigated bulk samples was obtained from the GaN film. A panchromatic IL image of the GaN film is shown in Fig. 7.1(a). The concentric squares in the IL image in Fig. 7.1(b) correspond to the areas irradiated with different ion fluences. The central square was exposed to
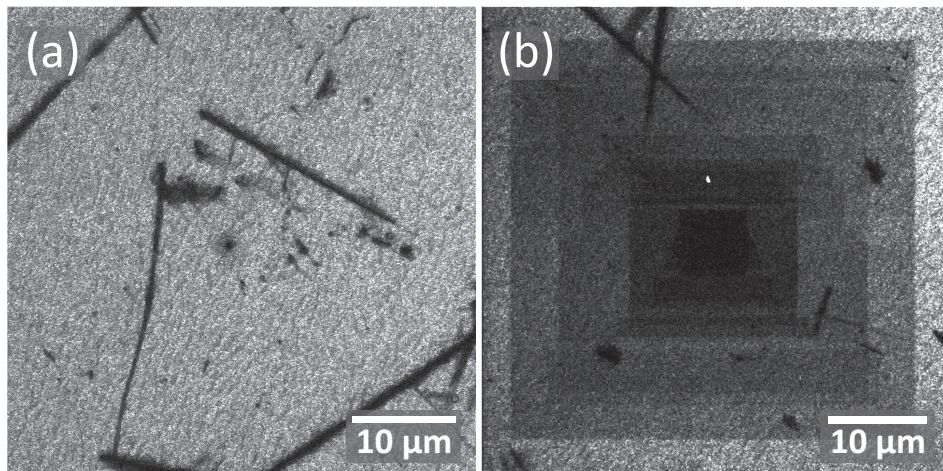
Figure 7.1: (a) IL image of a GaN surface. He$^+$ beam energy is $35\,$keV. Field of view (FOV): $45\,\mu$m. (b) IL image of GaN surface irradiated in steps by He$^+$ beam with energy of $35\,$keV. The central square was exposed to the fluence of 8×10^{13} ions/cm^2. FOV: $47\,\mu$m.

the highest fluence of approximately 8×10^{13} ions/cm^2. The dark lines in the image correspond to the dislocations which were originally present in the film. Line dislocations act as effective non-radiative recombination centers and quench the luminescence [161, 162].

Although the IL signal from the GaN film is rapidly quenched, we were able to record an emission spectrum. Typical IL spectra are shown in Fig. 7.2(a). The presented spectra were recorded at different beam energies of $10\,$keV (red line) and $35\,$keV He$^+$ (blue line), with the remainder of the acquisition parameters kept constant. Ultra violet emission at $360\,$nm ($3.4\,$eV), which corresponds to the band-gap transition in GaN, is absent in our measurements. Yellow emission around $560\,$nm ($2.2\,$eV) that is typical for GaN seems not to depend on the excitation beam energy (see inset in Fig. 7.2(a)) and is relatively weak compared to the observed $3\,$eV emission. The yellow emission has been extensively studied for several decades, but there is still no clear agreement on its exact nature (see Review [163]). It is usually attributed either to Ga vacancies, or to impurities such as C or O. We do not observe an increase of the yellow emission with increasing ion dose and subsequent increase of the crystal defects. This points towards impurities as the source of the $2.2\,$eV emission, rather than structural defects. Both spectra have a strong peak at
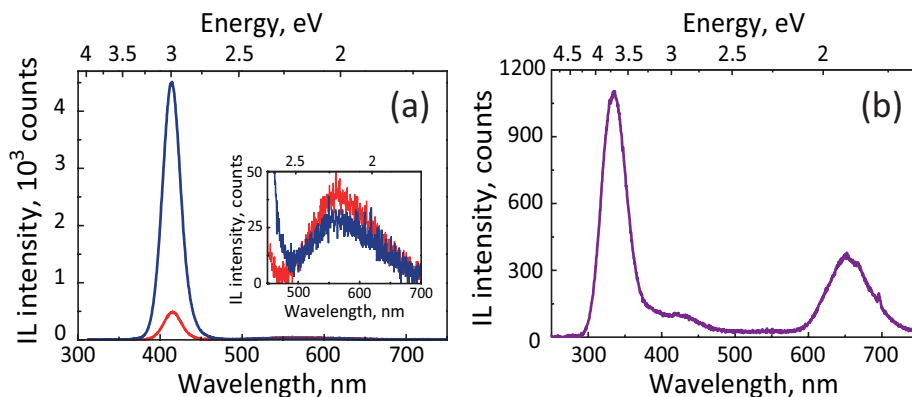
Figure 7.2: (a) IL spectra of n-type doped GaN obtained at a He$^+$ beam energy of $10\,\text{keV}$ (red line) and $35\,\text{keV}$ (blue line). The spectra are recorded at identical settings: $3\,\text{pA}$ beam current, $10\,\mu\text{s}$ dwell time, $10\,\text{s}$ acquisition time. (b) Raw IL spectrum of the sapphire substrate. He$^+$ beam energy is $35\,\text{keV}$.

$415\,\text{nm}$ (or $\sim 3\,\text{eV}$), which is enhanced by a factor of 9 at a beam energy of $35\,\text{keV}$ compared to the $10\,\text{keV}$ irradiation. It is unlikely to be related to band-gap emission (typically at $3.4\,\text{eV}$), since a shift of $0.4\,\text{eV}$ would require a significant modification of the material composition.

At first sight this strong peak at $415\,\text{nm}$ may be attributed to emission from the sapphire substrate, where emission at this wavelength corresponds to the emission from F- centers [164]. However, the thickness of the GaN layer is $4.5\,\mu\text{m}$, while the penetration depth of a $35\,\text{keV}$ He$^+$ beam in GaN is only $180\,\text{nm}$ according to SRIM simulations [57]. The penetration depth of a $10\,\text{keV}$ beam is only $60\,\text{nm}$. Thus, we do not expect the He$^+$ beam to be able to excite luminescence of the underlying substrate.

Additionally, we have measured the emission spectrum of the sapphire substrate from an area free of the GaN layer. It is shown in Fig. 7.2(b). As expected it exhibits luminescence around $415\,\text{nm}$. However, the by far strongest peak at $330\,\text{nm}$ corresponds to the emission of F$^+$- centers [164, 165]. An F-center in sapphire (Al$_2$O$_3$) consists of two electrons, which occupy an oxygen vacancy. Under irradiation an F- center can lose an electron and is converted into an F$^+$- center [164, 165]. A small sharp peak at $\sim 695\,\text{nm}$ originates from the impurity Cr^{3+} ions [165, 166]. The band at $660\,\text{nm}$ is a superposition of the Cr^{3+} N-lines and sidebands [166, 167] with the second-order peak of the $330\,\text{nm}$ emission. GaN is
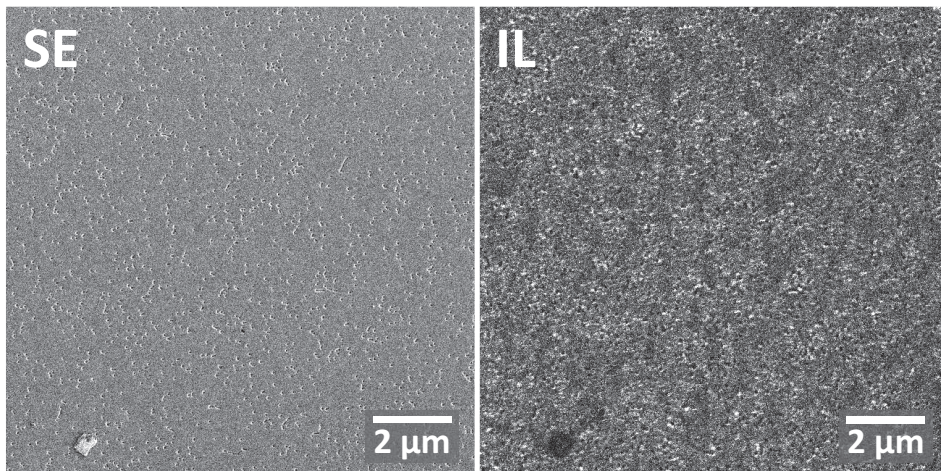
Figure 7.3: SE and panchromatic IL images of Si-doped GaN film. He$^+$ beam energy is $35\,\mathrm{keV}$. FOV is $12\,\mu\mathrm{m}$.

opaque for $330\,\mathrm{nm}$ light, but transparent for the Cr^{3+} associated emission. However, this band is absent in the spectra of the GaN film (Fig. 7.1(a)). This serves as an additional proof that the origin of the observed IL signal is from the GaN layer itself and not from the substrate.

More surface details of the GaN film can be distinguished in the SE image in Fig. 7.3 (left image). The holes in the surface are V-pits with diameters of 50-90 nm. These are V-shaped defects–open hexagonal inverted pyramids with $\{10\bar{1}1\}$ faceted walls–which are formed during film growth [168–171]. A simultaneously recorded panchromatic IL image (right in Fig. 7.3) shows the spatial distribution of the IL emission. The defect free areas provide a relatively low IL signal. The emission is enhanced in the vicinity of defect agglomerations and located close to the defects. Imaging with a blue filter (400-500 nm) has led to the same result, however, the images provided a weaker contrast due to the partial intensity cut-off by the filter. An enhancement of the CL signal at the V-pits was previously observed in GaN, AlInGaN and Si-doped AlGaN films [172–174] and was attributed to the enhancement of the free carrier recombination at the associated defect sites.

The origin of the $3\,\mathrm{eV}$ emission is not completely clear [163]. Several photoluminescence [163, 175, 176] and CL [176–178] studies show the presence of blue emission from undoped and Si-doped GaN layers. Authors in [176, 177] relate it to structural defects with a deep level [176].
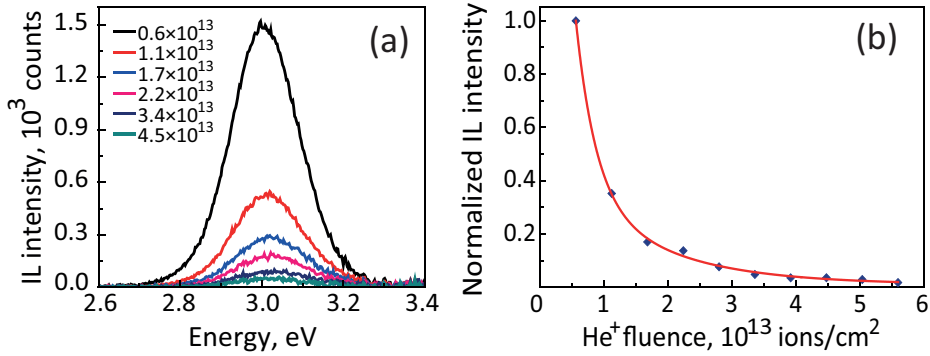
Figure 7.4: (a) Change of the 3 eV IL peak from Si-doped GaN with increasing He$^+$ fluence (in ions/cm^2). (b) Degradation of the total in 300-750 nm range IL signal from Si-doped GaN with increasing He$^+$ fluence. He$^+$ beam energy is 35 keV.

In addition, STM studies of the V-pit defects have shown that there are deep traps related to them [179]. Furthermore, we have followed the development of the 3 eV peak with increasing ion fluence at a beam energy of 35 keV at several different scanning parameters. We observed a blue shift of the position of the emission peaks from 2.98 eV at a fluence of 1.4×10^{12} ions/cm^2 to $\sim$3.03 eV after increasing the fluence by a factor of 30. One of the obtained results is presented in Fig. 7.4(a)). Each spectrum was acquired during irradiation of a 50 µm × 50 µm square for 10 s at a beam current of 1 pA. Fig. 7.4 (b) shows the degradation of the total IL signal with increasing ion fluence. The signal is quenched already at a fluence of several times 10^{13} ions/cm^2.

Another bulk semiconductor material examined was InP. A typical IL spectrum is shown in Fig. 7.5(a). The spectrum was recorded while scanning a 100 µm × 100 µm sample area for 100 s at a 50 pA beam current. Despite the low signal to noise ratio, the emission peak is clearly discernible. It is centered at 1.34 eV which corresponds to the InP band-gap at RT [180,181]. The degradation of the IL signal is shown in Fig. 7.5(b). The signal rapidly drops to zero.

The last tested bulk sample was a S-doped GaP wafer. The IL spectrum is shown in Fig. 7.6(a). It was obtained from an area of 50 µm × 50 µm at a beam current of 290 pA and spectrum collection time of a 50 s. The sample shows a broad band emission with a maximum at 1.9 eV. CL studies of defect generation by proton, neutron and gamma ray
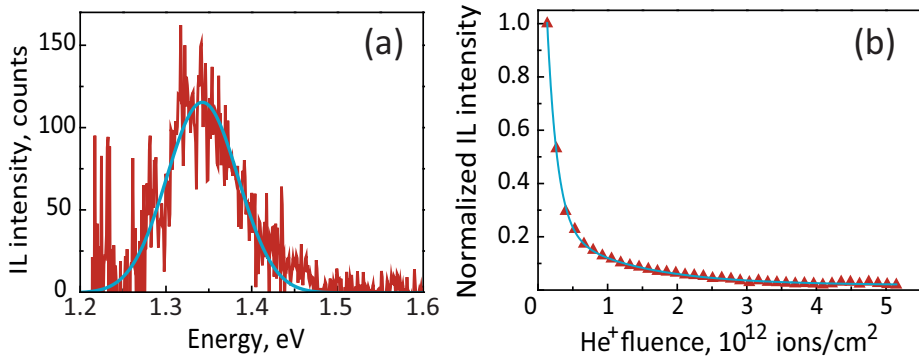
Figure 7.5: (a) IL spectrum of InP wafer. The peak is fitted by a Gasussian with a center at $1.34\,\text{eV}$. (b) Degradation of the IL signal from InP wafer with increasing He^+ fluence. The ion beam energy is $35\,\text{keV}$.
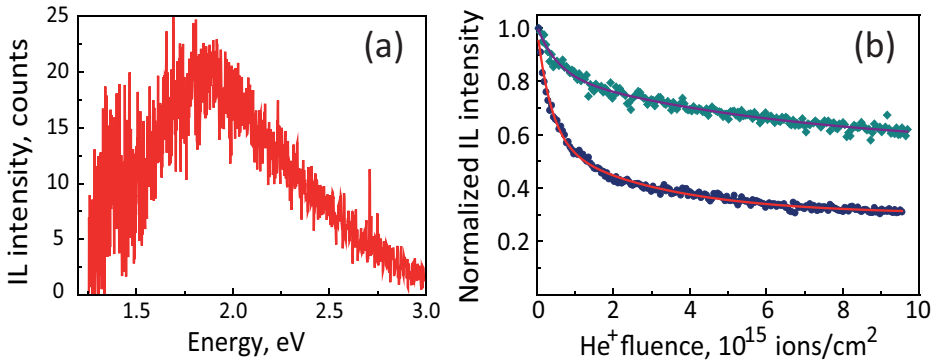

Figure 7.6: (a) Raw IL spectrum of S-doped GaP. (b) Degradation of the IL signal from GaP bulk sample (blue circles) and NWs (dark cyan diamonds) with increasing He^+ fluence. Ion beam energy is $35\,\text{keV}$.

irradiation in GaP crystals have shown similar results [182]. The band-gap emission (2.26 eV) and the near-band-edge emission (2.15-2.33 eV), associated with dopants and impurities, are suppressed and a new dominant peak at 1.9 eV develops. The degradation of the IL signal with increasing He$^+$ fluence is presented in Fig. 7.6(b) by blue circles. Although the IL signal is very low, it does not vanish completely as was the case for the previous two examples. The IL signal drops by 70 % after a fluence of 9.5×10^{15} ions/cm^2.

Mainly isolated point defects are created during the light ion irradiation of semiconductors [72, 183–185]. Point defects introduce shallow levels in the band gap, influencing the charge carrier lifetime and mobility [184, 185]. Additionally, the created defects can provide radiationless paths for electron de-excitation. With an increase of the ion fluence the damage may accumulate and transform into complex defect clusters [72, 183]. Swift heavy ion irradiation studies at RT showed that in the case of GaP the relative defect concentration does not exceed a certain level even at high ion fluences, whereas a continuous amorphous layer develops in InP [186]. This difference in response of materials to the ion irradiation may explain the different IL signal degradation with increasing fluence (compare Fig. 7.5(b) and Fig. 7.6(b)).

7.4 Semiconductor nanowires

Two types of semiconductor NWs were investigated: GaP and overgrown GaP-GaAs nanowires. In contrast to bulk semiconductors, the IL emission from NWs turned out to be remarkably stable under ion beam irradiation. Secondary electron and panchromatic IL images of overgrown GaP-GaAs NWs are presented in Figure 7.7. An arrow in the images points at a NW with a thickness of 17 nm. This very narrow wire is clearly resolved not only in the SE, but also in the IL image.

Simultaneously acquired SE and panchromatic IL images of GaP NWs are presented in Fig. 7.8. The initial state of the NWs is demonstrated in Figs. 7.8(a) (SE) and (c) (IL). The images were recorded using a dose of 1.4×10^{17} ions/cm^2 per scan. In the images in Figs. 7.8(b) and (d) the same sample area is shown, but after exposure to an ion fluence of 2.8×10^{17} ions/cm^2. That is a four orders of magnitude higher fluence than the one used for imaging the GaN film discussed previously (Fig. 7.1). As can clearly be seen from a comparison of Fig. 7.8 (a) and
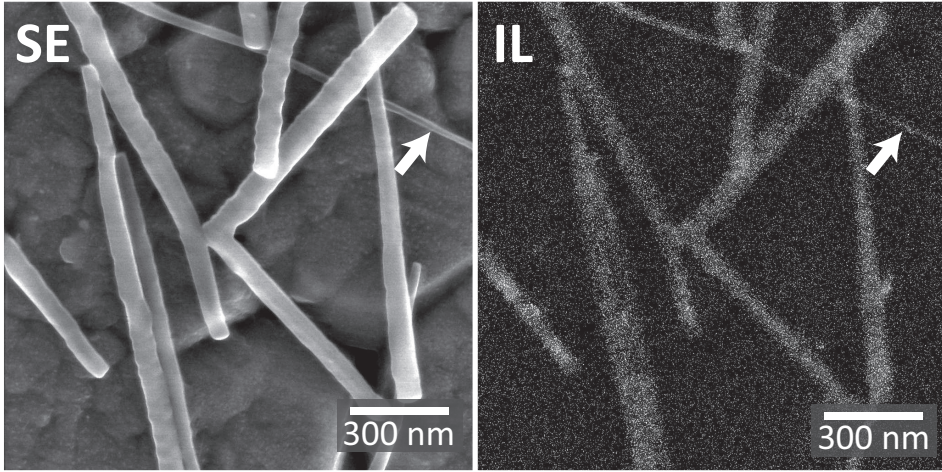
Figure 7.7: HIM SE and panchromatic IL image of overgrown GaP-GaAs nanowires. The arrow points at a nanowire with thickness of 17 nm, detectable by IL imaging. FOV is 1.42 μm.

7.8 (b), the NWs were substantially modified by the ion beam: they are deformed, bent or even swollen. However, despite all the modifications they continue to emit (IL images in Figs. 7.8 (c) and (d)).

The degradation of the IL from the GaP NWs is shown in Fig. 7.6(b) (dark cyan diamonds). The trend is similar to the one of the bulk GaP. However, after an applied fluence of $9.5{\times}10^{15}$ ions/cm^2 the IL signal decreased only by 30 %. The IL signal degradation curves for both bulk and NWs GaP samples were recorded under identical conditions.

Although the beam modifies the NWs, the main damage is produced deep in the substrate that the NWs are placed on. The first several tens of nanometers the He$^+$ ion beam dissipates its energy mostly via electronic excitations. The hard nuclear collisions occur deeper in the bulk when the ions have lost energy and nuclear stopping becomes more important. Additionally, most of the sample damage in the case of He$^+$ irradiation is caused by recoiling target atoms (see Chapter 4). However, due to their size this mechanism is not of importance for the discussed NWs. Therefore, we propose that the observed modifications of the NWs are caused by sample heating, while no helium is implanted nor a considerable amount of traps for the charge carriers is created. A similar result was observed in [50] where the authors were able to obtain IL signal from agglomerates of semiconductor QDs, but not from bulk samples.
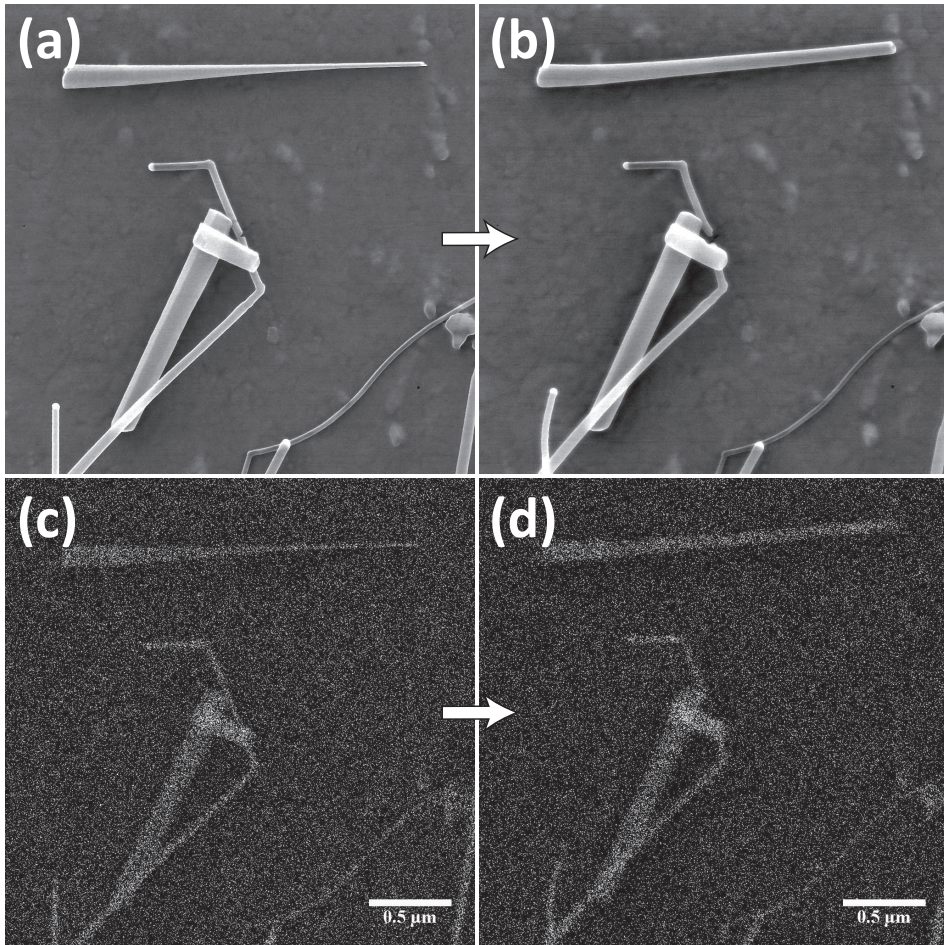
Figure 7.8: (a) and (c) are SE and IL images of the GaP NWs. (b) and (d) are repetitively recorded SE and IL images of the same NWs. The images were recorded an applying ion fluence of 1.4×10^{17} ions/cm^2. He$^+$ beam energy is 35 keV. FOV: 2.84 μm.
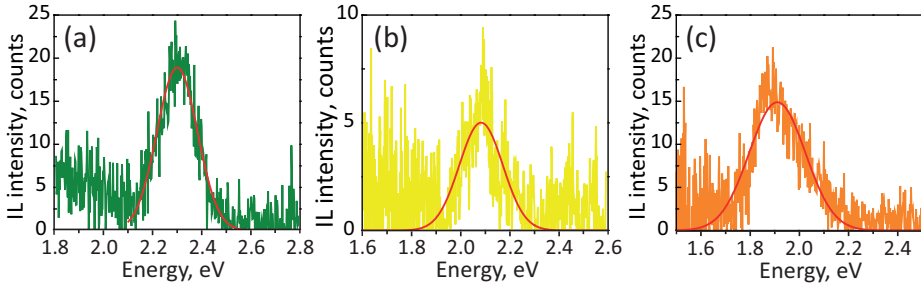
Figure 7.9: IL spectra of quantum dots. The expected peaks are: (a) 2.38 eV, (b) 2.1 eV, (c) 1.94 eV.

7.5 Semiconductor quantum dots

Quantum dots with three different emission peaks were tested: 520 nm (2.38 eV), 590 nm (2.1 eV), 640 nm (1.94 eV). The corresponding peak positions from the IL measurements are 2.3 eV, 2.08 eV, 1.91 eV. Since the peaks are systematically down-shifted, the slight discrepancy between the expected and experimentally measured values could be caused by calibration errors. However, the smallest QDs (2.3 eV ones) show a two times bigger shift of 0.08 eV compared to the two other samples. The variation in size of the smaller sized QDs leads to a bigger variation in the band-gap width [187]. Thus, this observed shift could be related to a slight discrepancy between the expected and actual sizes of the QDs.

Big agglomerations of 2.38 eV quantum dots (QDs) on an Al substrate were imaged with IL (Fig. 7.10). The images were recorded at a dose of 5×10^{12} ions/cm^2. Unfortunately, we were not able to resolve individual quantum dots.

Several reasons can be given for this. First, the QDs were deposited by simple evaporation of the solvent. The QDs are embedded in a relatively thick layer of the hydrocarbon residue from the toluene solution (see Fig. 7.10 (a)). Second, the diameter of the measured QDs varies between 2.6 nm (for 2.38 eV) and 6.5 nm (for 1.94 eV). Therefore, the volume available for the IL excitation is extremely small. Thus, high ion fluences are required for excitation of a measurable IL signal from a single QD, which in turn will lead to severe damage of the QD most likely before any IL signal could be detected.
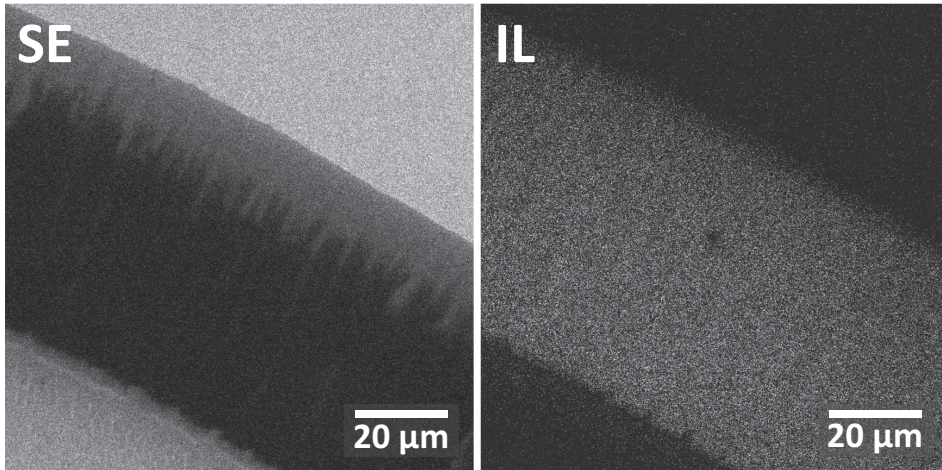
Figure 7.10: HIM SE and panchromatic IL images quantum dots deposited on Al substrate. FOV is 100 μm.

7.6 Conclusions

We have investigated the influence of the He$^+$ ion beam on the luminescence properties of the semiconductor materials applying the IL technique. All examined samples have yielded an IL signal, however the relative signal strength depended on the material composition. The obtained IL spectra consist of band-gap emission along with the transitions related to the various defects. The IL signal from all samples decreases with increasing ion dose as a result of defect generation. However, the IL signal stability turned out to depend not only on the composition, but also on the sample dimensions. In general, the IL signal from nanostructures is more stable than from bulk material due to the lower defect generation rate. Unfortunately, we can conclude that the IL technique is not suitable for the characterization of the electronic structure of bulk semiconductors due to its significant modification during ion irradiation. Nevertheless, the technique can be used for characterization of the irradiation damage. This can be done in a fluence and rate dependent manner for bulk, as well as nanostructured samples with very high spatial resolution. The high resolution capability of the instrument is a clear advantage here.

Summary

This thesis describes several approaches for material characterization using helium ion microscopy (HIM). Furthermore, it also demonstrates a possibility for in-situ observation and investigation of material modification and defect creation. This has been done using He^+ ions with an energy of several tens of keV. The influence of a sub-nanometer He^+ ion beam on different classes of materials, such as metals, semiconductors and insulators, was studied in the current work.

We start by exploring the capabilities of HIM to utilize ion channeling phenomena. Using a {111} textured polycrystalline Au film as an example we demonstrate in Chapter 3 how ion channeling contrast in secondary electron (SE) images can be used for crystal orientation mapping. A simple geometrical model was used to predict channeling minima and determine grain orientations. The ion doses, required for acquiring an SE image and a backscattered helium (BSHe) image with a similar signal to noise ratio, are much lower for the SE images. Therefore, using channeling contrast in SE images for analysis reduces sample damage and speeds up the measurements. Moreover, the short SE escape depth provides an opportunity to identify the crystal orientation of thin layers. Additionally, we demonstrate and describe the origin of an unexpected contrast in BSHe images of thin light layers on a heavy crystalline substrate. This de-channeling contrast is caused by a change in the backscatter yield due to the decrease of the channeling probability when low-index directions in the underlaying crystal are blocked by a thin adlayer. These results also emphasize the importance of the vacuum conditions for samples investigations in HIM.

Surface structure modifications were observed under prolonged exposure of the Au {111} sample to the He^+ beam. These changes of the surface morphology as a function of ion fluence and energy are discussed in Chapter 4. A periodic structure of ripples running along $\langle 1\bar{1}0 \rangle$ directions develops on the surface under beam irradiation at normal incidence. Initially, the pattern periodicity does not depend on the beam energy and has a power-law dependence on the ion fluence with an exponent of 0.26 ± 0.01. The pattern formation is governed by the diffusion

of gold adatoms and surface vacancies. The further evolution of the surface morphology after a critical ion fluence of $\approx 4.2 \times 10^{17}\,\mathrm{cm^{-2}}$ depends on the beam energy used. In the case of a low beam energy of $15\,\mathrm{keV}$ a porous structure develops. In contrast, when using a higher energy of $35\,\mathrm{keV}$, a sub-surface blister develops. This different behavior is a result of the variation of the helium implantation depth with change of the beam primary energy. Helium filled nanobubbles form in the bulk during ion irradiation. As estimated from the experimental data, the gas pressure inside these bubbles exceeds a few GPa. Depending on implantation depth, the evolving bubbles either break through the surface and form a porous structure, or – if formed deeper in the bulk – coalesce and create a blister. In addition, surface modifications are also observed outside of the irradiated areas. This indicates the importance of the gold recoils for the surface structuring process.

Defect generation in ionic crystals in HIM was investigated using iono-luminescence (IL). While SE imaging provides mainly surface information, the IL signal gives an insight in the processes occurring along the entire path of an ion in the bulk. In Chapter 5 we study the creation of color-centers in NaCl under He^+ ion beam irradiation by analyzing the generated IL signal. The emission that is observed results from the recombination of charge carriers with the beam induced color-centers, namely F- and V_F-centers. The rate of formation of the emitting centers was found to depend on beam scanning parameters such as pixel separation and beam current. The concentration of the emitting centers depends on the balance between the various types of crystal defects that are created. The observed effects are interpreted as a result of the overlapping of the interaction volumes of ions arriving within neighboring pixels. Highly mobile H-centers, created at a previous pixel, can quench initially created F-centers. In the case of high concentrations of H-centers at high beam currents, their clustering leads to the enhancement of F-center production.

The actual lateral size of the interaction volume of a sub-nanometer $35\,\mathrm{keV}$ He^+ beam with NaCl was directly visualized and measured. These results are discussed in Chapter 6. The characteristic length scale of the radial defect distribution was estimated to be $88.3 \pm 1.5\,\mathrm{nm}$. We have also used SRIM simulations to estimate the defect concentration required for the generation of a measurable IL signal. The obtained defect concentration is $3\,\mathrm{vac/nm^2}$. The generation of color-centers with a sub-nanometer He^+ beam allows to locally change luminescence properties

with a very high precision. In this chapter we have demonstrated a luminescent pattern created in a such way.

We have observed a significant influence of the ion irradiation on the luminescence properties of semiconductor samples. Various semiconductor materials with different geometries such as bulk samples, nanowires and quantum dots, have been examined. The results are described in Chapter 7. All tested samples exhibited IL. The light emission originates from band-gap transitions as well as from defect related transitions. However, the IL signal rapidly degraded under the influence of the ion irradiation due to the creation of the crystal defects. These can provide pathways for non-radiative electronic de-excitations. The quenching of IL with increasing ion fluence strongly depends not only on the chemical composition of the sample, but also on its dimensions. Bulk samples were found to be more sensitive to ion irradiation. We relate this to the depth distribution of ion induced defects and, therefore, a lower defect generation rate in thin samples. In general, IL was found not to be suitable for the characterization of the intrinsic properties of semiconductors. However, it can be applied for the investigation of the defect formation processes. In addition, opposite to the luminescence patterning described in Chapter 6, here ion irradiation can be used for negative patterning.

In conclusion, this work presents an extensive study of the defect generation induced by a He^+ ion beam and also introduces new ways for sample characterization in HIM. Helium implantation can be used for tuning the materials mechanical properties. Further investigations are required in this direction to precisely measure the modified material properties. For a better understanding of the processes which occur under ion irradiation, the IL technique should be combined with more established techniques such as cathodoluminescence or transmission electron microscopy. Finally, using the example of luminescence properties, we have demonstrated how a sub-nanometer He^+ beam can be used for the precise local modification of various physical properties.

Samenvatting

Dit proefschrift beschrijft verschillende benaderingen voor materialenonderzoek met heliumionenmicroscopie (HIM). Daarnaast demonstreert het ook de mogelijkheid voor in-situ modificatie van materialen en de vorming van defecten met heliumionen met een energie van enkele tientallen keV. De invloed van een sub-nanometer heliumionenbundel op verschillende klasses materialen, zoals metalen, halfgeleiders en isolatoren is onderzocht.

We beginnen het verkennen van de mogelijkheden van HIM met het gebruik van channeling. Met behulp van een {111}-getextureerd polykristallijne goudlaag laten we in hoofdstuk 3 zien hoe channelingcontrast in beelden, die gevormd zijn met secundaire elektronen (SE), gebruikt kan worden om de kristallijne orientatie van het preparaat te bepalen. Een eenvoudig geometrisch model is gebruikt om de omvang van het channeling contrast te voorspellen en de oriëntatie van de verschillende korrels te bepalen. De ionendoses, die nodig zijn voor het meten van een SE-afbeelding zijn veel lager dan die voor een afbeelding met een vergelijkbare signaal-ruis verhouding die gevormd is uit terugverstrooide heliumionen (BSHe). Channeling contrast in SE afbeeldingen kan daarom gebruikt worden voor een analyse met minimale sample schade en een verkorte meettijd. Bovendien biedt het gebruik van secundaire elektronen vanwege hun lage ontsnappingsdiepte, de mogelijkheid om de orientatie van dunne lagen vast te stellen. We laten tevens zien hoe een onverwachte vorm van contrast verschijnt in BSHe afbeeldingen van een dunne laag van een licht materiaal op een substraat van een zwaar materiaal. Dit "ontchannelingscontrast" wordt veroorzaakt door de verandering in het aantal terugverstrooide ionen ten gevolge van de zwakke wisselwerking van de bundel met de dunne laag en het (gedeeltelijk) blokkeren van channeling richtingen. Deze resultaten benadrukken tevens het belang van goed vacuum in HIM.

Bij lange blootstelling aan de bundel verandert de oppervlaktestructuur van Au{111} onder invloed van de heliumbundel. De veranderingen in morfologie worden in hoofdstuk 4 besproken als functie van de ionendosis en -energie. Een periodieke wasbordstructuur, die langs de

$\langle 1\bar{1}0\rangle$ richting loopt, ontwikkelt zich op het oppervlak tijdens bestraling met loodrecht invallend helium. Initieel hangt de periodiciteit van het patroon niet af van de energie en ontwikkelt het zich als functie van de dosis volgens een machtswet met een exponent van 0.26 ± 0.01. De vorming van het patroon wordt primair bepaald door de diffusie van goud adatomen en oppervlaktevacatures. Na een kritische dosis van ongeveer $\approx 4.2\times 10^{17}$ cm^{-2} hangt de verdere evolutie af van de primaire energie. Voor het geval van een lage primaire energie van 15 keV ontwikkelt zich een poreuze structuur. Voor een hoge energie van 35 keV ontwikkelt zich daarentegen onder het zichtbare oppervlak een zogeheten blaar. Dit verschillende gedrag is het gevolg van het verschil in de diepte waarop het helium geïmplanteerd wordt bij verschillende energieen. Kleine, met helium gevulde nanobelletjes vormen zich in het materiaal tijdens blootstelling aan de bundel. Uit de experimentele data schatten we de gasdruk in deze belletjes op enige GPa. Afhankelijk van de indringdiepte breken de bellen uiteindelijk door het oppervlak heen, vormen ze een poreuze structuur, of, bij een zeer grote indringdiepte, vormen de belletjes samen een blaar. De oppervlakteveranderingen zijn ook zichtbaar buiten het belichte gebied, wat het belang aangeeft van secundair gecreëerde snelle goudatomen.

De vorming van defecten met HIM in ionische kristallen is onderzocht met ionoluminescentie (IL). Waar afbeeldingen met secundaire elektronen vooral oppervlakteïnformatie leveren, geeft het IL signaal inzicht in de processen die plaatsvinden langs het gehele pad dat een invallend ion in de bulk van een preparaat aflegt. In hoofdstuk 5 bekijken we de vorming van kleurcentra in natriumchloride onder invloed van de heliumbundel en analyzeren we veranderingen in het IL signaal. Licht emissie is het gevolg van de recombinatie van ladingsdragers met kleurcentra die door de bundel geinduceerd zijn, namelijk F- en V_F- centra. De vormingssnelheid van de kleurcentra hangt af van parameters als pixelafstand en bundelstroom. De concentratie van de kleurcentra hangt af van de balans tussen de verschillende types defecten die gevormd worden. De effecten, die we hebben waargenomen, verklaren we uit een overlap tussen het interactievolume van ionen die voor verschillende, naburige pixels geprojecteerd worden op het preparaat. Zeer mobiele H- kleurcentra die in een voorgaande pixel gevormd zijn, kunnen de vorming van initieel gecreëerde F- centra onderdrukken. Voor zeer hoge concentraties aan H- centra bij hoge bundelstromen daarentegen, kan het clusteren van H- centra leiden tot een verhoogde productie van F- centra.

De fysieke afmeting van het wisselwerkingsvolume van een sub-nanometer 35 keV heliumbundel met natriumchloride is direct in beeld gebracht. Deze resultaten worden schreven in hoofdstuk 6. De karakteristieke lengteschaal van de defectverdeling is geschat op 88.3 ± 1.5 nm. We hebben ook SRIM simulaties gebruikt om de defectconcentratie die nodig is voor een minimaal meetbaar IL signaal bepaald. Die concentratie is gelijk aan drie vacatures per vierkante nanometer. De vorming van kleurcentra onder invloed van de heliumbundel stelt ons daarnaast in staat om de luminescentie-eigenschappen van het materiaal met hoge precisie te wijzigen. We laten in dit hoofdstuk voorbeelden zien van patronen die op deze wijze gemaakt zijn.

We hebben tevens een substantiële invloed waargenomen van de bundel op halfgeleider preparaten. Verschillende halfgeleiders met verschillende geometrieen zoals bulk samples, nanodraden en quatum dots, zijn onderzocht. De resultaten zijn beschreven in hoofdstuk 7. De uitzending van fotonen is in dit geval het gevolg van elektronische overgangen rond de bandgap, als mede van overgangen in defecten. Het meetbare IL signaal loopt onder invloed van de bundel echter zeer snel terug vanwege de vorming van kristaldefecten. Die defecten openen nieuwe mogelijkheden voor verval van energetische elektronen zonder uitzending van licht. De onderdrukking van het IL signaal met toenemende blootstelling hangt aan ionen niet enkel van de chemische samenstelling van het preparaat af, maar ook van de afmetingen. Bulk preparaten zijn gevoeliger voor bestraling. We verklaren dit uit de diepteverdeling waarin defecten geïnduceerd worden, wat leidt tot een lagere defectconcentratie in preparaten met een afmeting kleiner dan het interactievolume. In het algemeen is IL ongeschikt voor de karakterisatie van de intrinsieke eigenschappen van halfgeleiders, het kan echter uitstekend toegepast worden voor het bestuderen van defecten en de vorming van defecten. In tegenstelling tot wat beschreven is in hoofdstuk 6, kunnen de optische eigenschappen van preparaten hier negatief gepatroneerd worden.

Samenvattend biedt het in dit proefschrift beschreven werk een uitgebreid overzicht van de wisselwerking en defectvorming van een heliumbundel op verschillende preparaten en laat het zien hoe preparaten gekarakteriseerd kunnen worden met HIM. Implantatie van helium kan gebruikt worden om materiaaleigenschappen op een plaatsopgeloste manier te wijzigen. Verder onderzoek is nodig om de gewijzigde eigenschappen exact te bepalen. Voor een beter begrip van de processen die plaatsvinden bij bestraling van een preparaat met heliumionen moet

IL gecombineerd worden met andere, meer gevestigde technieken zoals katodholuminescentie en transmissie elektronen microscopie. Tenslotte hebben we laten zien dat de sub-nanometer heliumbundel gebruikt kan worden voor een precieze, lokale verandering van verschillende fysische eigenschappen.

Bibliography

[1] A. Zewail, *Phil. T. Roy. Soc. A* **368**, 1191 (2010).

[2] T. Zhang and I. Yamaguchi, *Opt. Lett.* **23**, 1221 (1998).

[3] M. Knoll and E. Ruska, *Z. Phy.* **78**, 318 (1932).

[4] E. Müller, *Z. Phys.* **131**, 136 (1951).

[5] A. Melmed, *Appl. Surf. Sci.* **94-95**, 17 (1996).

[6] J. Orloff and L. Swanson, *J. Appl. Phys.* **50**, 6026 (1979).

[7] K. Horiuchi, T. Itakura, and H. Ishikawa, *J. Vac. Sci. Technol. B* **6**, 937 (1988).

[8] M. Sato, *Jpn. J. Appl. Phys.* **31**, L291 (1992).

[9] V. N. Tondare, *J. Vac. Sci. Technol. A* **23**, 1498 (2005).

[10] W. Escovitz, T. Fox, and R. Levi-Setti, *Proc. Natl. Acad. Sci. USA* **72**, 1826 (1975).

[11] J. Orloff and L. Swanson, *J. Vac. Sci. Technol.* **12**, 1209 (1975).

[12] T. Itakura, K. Horiuchi, and S. Yamamoto, *Microelectron. Eng.* **3**, 153 (1985).

[13] K. Horiuchi, T. Itakura, and H. Ishikawa, *J. Vac. Sci. Technol. B* **6**, 241 (1988).

[14] H. Rose, Springer Series in Optical Sciences, in *Geometrical Charged-Particle Optics*, volume 142, Springer, 2009.

[15] B. Ward, J. Notte, and N. Economou, *J. Vac. Sci. Technol. B* **24**, 2871 (2006).

[16] R. Hill and F. Rahman, *Nucl. Instrum. Meth. A* **645**, 96 (2011).

[17] G. Lloyd, *Mineral. Mag.* **51**, 3 (1987).

[18] D. Prior, A. Boyle, F. Brenker, M. Cheadle, A. Day, G. Lopez, L. Peruzzo, G. Potts, S. Reddy, R. Spiess, N. Timms, P. Trimby, J. Wheeler, and L. Zetterström, *Am. Mineral.* **84**, 1741 (1999).

[19] M. Phaneuf, *Micron* **30**, 277 (1999).

[20] S. Canovic, T. Jonsson, and M. Halvarsson, *J. Phys. Conf. Ser.* **126**, 012054 (2008).

[21] R. Stewart, *Phys. Rev.* **45**, 488 (1934).

[22] A. Pimpin and W. Srituravanich, *Eng. J.* **16**, 37 (2012).

[23] J. Orloff, M. Utlaut, and L. Swanson, *High Resolution Focused Ion Beams: FIB and its Applications*, Springer US, 2003.

[24] C. White, *Nucl. Instrum. Methods* **149**, 497 (1978).

[25] P. Townsend, *Nucl. Instrum. Meth. B* **286**, 35 (2012).

[26] J. Mogran, J. Notte, R. Hill, and B. Ward, *Microscopy Today* **14**, 24 (2006).

[27] N. Ernst, G. Bozdech, H. Schmidt, W. Schmidt, and G. L. Larkins, *Appl. Surf. Sci.* **67**, 111 (1993).

[28] R. Hill, J. Notte, and B. Ward, *Physics Procedia* **1**, 135 (2008).

[29] H. Bethe, *Phys. Rev.* **59**, 913 (1941).

[30] K. Ohya, K. Inai, A. Nisawa, and A. Itoh, *Nucl. Instrum. Meth. B* **266**, 541 (2008).

[31] R. Ramachandra, B. Griffin, and D. Joy, *Ultramicroscopy* **109**, 748 (2009).

[32] Y. Lin and D. Joy, *Surf. Interface Anal.* **37**, 895 (2005).

[33] H. Salow, *Phys. Zeit.* **41**, 434 (1940).

[34] J. Notte, B. Ward, N. Economou, R. Hill, R. Percival, L. Farkas, S. McVey, D. Seiler, A. Diebold, R. McDonald, C. M. Garner, D. Herr, R. Khosla, and E. Secula, An Introduction to the Helium Ion Microscope, in *AIP Conference Proceedings*, edited by D. G. Seiler, A. C. Diebold, R. McDonald, C. M. Garner, D. Herr, R. P. Khosla, and E. M. Secula, volume 931, pp. 489–496, AIP, 2007.

[35] D. Bell, *Microsc. Microanal.* **15**, 147 (2009).

[36] G. Behan, D. Zhou, M. Boese, R. Wang, and H. Zhang, *J. Nanosci. Nanotechnol.* **12**, 1094 (2012).

[37] D. Fox, Y. Zhou, A. O'Neill, S. Kumar, J. Wang, J. Coleman, G. Duesberg, J. Donegan, and H. Zhang, *Nanotechnology* **24**, 335702 (2013).

[38] G. Behan, J. Feng, H. Zhang, P. Nirmalraj, and J. Boland, *J. Vac. Sci. Technol. A* **28**, 1377 (2010).

[39] L. Scipioni, C. Sanford, J. Notte, B. Thompson, and S. McVey, *J. Vac. Sci. Technol. B* **27**, 3250 (2009).

[40] A. Marfunin, Luminescence, in *Spectroscopy, Luminescence and Radiation Centers in Minerals*, chapter 5, pp. 141–222, Springer, Berlin, Heidelberg, 1979.

[41] C. Kerkdijk and E. Thomas, *Physica* **63**, 577 (1973).

[42] W. Baird, M. Zivitz, and E. Thomas, *Phys. Rev. A* **12**, 876 (1975).

[43] W. van der Weg and P. Rol, *Nucl. Instrum. Methods* **38**, 274 (1965).

[44] N. Tolk, I. Tsong, and C. White, *Anal. Chem.* **49**, 16A (1977).

[45] D. Ghose and R. Hippler, Ionoluminescence, in *Luminescence of Solids*, edited by D. R. Vij, pp. 189–220, Springer US, 1998.

[46] U. Scherz, Grundlagen der Festkörperphysik, in *Lehrbuch der Experimentalphysik*, pp. 1–107, 1992.

[47] R. Williams and K. Song, *J. Phys. Chem. Solids* **51**, 679 (1990).

[48] M. Doherty, N. Manson, P. Delaney, F. Jelezko, J. Wrachtrup, and L. Hollenberg, *Phys. Rep.* **528**, 1 (2013).

[49] K. Schwartz, Excitons and radiation damage in alkali halides, in *Atomic Physics Methods in Modern Research*, edited by K. P. Jungmann, J. Kowalski, I. Reinhard, and F. Träger, volume 1 of *Lecture Notes in Physics*, pp. 351–366, Springer, Berlin, 1997.

[50] S. Boden, T. Franklin, L. Scipioni, D. Bagnall, and H. Rutt, *Microsc. Microanal.* **18**, 1253 (2012).

[51] T. Everhart and R. Thornley, *J. Sci. Instrum.* **37**, 246 (1960).

[52] J. Ladislas Wiza, *Nucl. Instrum. Methods* **162**, 587 (1979).

[53] R. van Gastel, L. Barriss, C. Sanford, G. Hlawacek, L. Scipioni, A. Merkle, D. Voci, C. Fenner, H. Zandvliet, and B. Poelsema, *Microsc. Microanal.* **17**, 928 (2011).

[54] A. George, M. Knez, G. Hlawacek, D. Hagedoorn, H. Verputten, R. van Gastel, and J. ten Elshof, *Langmuir.* **28**, 3045 (2012).

[55] G. Hlawacek, P. Puschnig, P. Frank, A. Winkler, C. Ambrosch-Draxl, and C. Teichert, *Science* **321**, 108 (2008).

[56] S. Lorbek, G. Hlawacek, and C. Teichert, *Eur. Phys. J. Appl. Phys.* **55**, 23902 (2011).

[57] J. Ziegler, M. Ziegler, and J. Biersack, *Nucl. Instrum. Meth. B* **268**, 1818 (2010).

[58] G. Kinchin and R. Pease, *Rep. Prog. Phys.* **18**, 1 (1955).

[59] J. Lindhard, *Mat.-Fys. Medd. Dan. Vid. Selsk.* **34** (1965).

[60] H. Feijen, L. Verhey, A. Boers, and E. Suurmeijer, *J. Phys. E Sci. Instrum.* **6**, 1174 (1973).

[61] R. Franklin, E. Kirk, J. Cleaver, and H. Ahmed, *J. Mater. Sci. Lett.* **7**, 39 (1988).

[62] R. Levi-Setti, T. Fox, and K. Lam, *Nucl. Instrum. Methods* **205**, 299 (1983).

[63] MEIS - fcc(111) stereographic projection., 2012, [Online; accessed 19-April-2012].

[64] E. Preuss, B. Krahl-Urban, and R. Butz, *Laue-Atlas : plotted Laue back-reflection patterns of the elements, the compounds RX and RX2*, Bertelsmann, 1974.

[65] J. Singh and J. Whitten, *J. Phys. Chem. C* , 19088 (2008).

[66] K.-Y. Wu, S.-Y. Yu, and Y.-T. Tao, *Langmuir* **25**, 6232 (2009).

[67] D. Bell, M. Lemme, L. Stern, J. Williams, and C. Marcus, *Nanotechnology* **20**, 455301 (2009).

[68] D. Maas, E. van Veldhoven, C. Ping, V. Sidorkin, H. Salemink, E. van der Drift, and P. Alkemade, Nanofabrication with a Helium Ion Microscope., in *Proceedings of the SPIE - The International Society for Optical Engineering*, p. 763814, 2010.

[69] L. Scipioni, D. Ferranti, V. Smentkowski, and R. Potyrailo, *J. Vac. Sci. Technol. B* **28**, 6 (2010).

[70] M. Annamalai, S. Mathew, V. Viswanathan, C. Fang, D. Pickard, and M. Palaniapan, Design, fabrication and Helium Ion Microscope patterning of suspended nanomechanical graphene structures for NEMS applications., in *2011 16th International Solid-State Sensors, Actuators and Microsystems Conference*, pp. 2578–2581, IEEE, 2011.

[71] S. Boden, Z. Moktadir, D. Bagnall, H. Mizuta, and H. Rutt, *Microelectron. Eng.* **88**, 2452 (2011).

[72] R. Livengood, S. Tan, Y. Greenzweig, J. Notte, and S. McVey, *J. Vac. Sci. Technol. B* **27**, 3244 (2009).

[73] S. Tan, R. Livengood, D. Shima, J. Notte, and S. McVey, *J. Vac. Sci. Technol. B* **28**, C6F15 (2010).

[74] D. Cohen-Tanugi and Y. Nan, *J. Appl. Phys.* **104**, 063504 (2008).

[75] D. Fox, Y. Chen, C. Faulkner, and H. Zhang, *Beilstein J. Nanotechnol.* **3**, 579 (2012).

[76] S. Donnelly, V. Vishnyakov, D. Taylor, R. Valizadeh, I. Ballard, and D. Goddard, *Appl. Surf. Sci.* **74**, 81 (1994).

[77] M. Ramana Murty, T. Curcic, A. Judy, B. Cooper, A. Woll, J. Brock, S. Kycia, and R. Headrick, *Phys. Rev. Lett.* **80**, 4713 (1998).

[78] D. Lau, A. Hughes, T. Muster, T. Davis, and A. Glenn, *Microsc. Microanal.* **16**, 13 (2010).

[79] S. Rusponi, G. Costantini, C. Boragno, and U. Valbusa, *Phys. Low Dimens. Str.* , 95 (1999).

[80] M. Siegert and M. Plischke, *Phys. Rev. Lett.* **73**, 1517 (1994).

[81] U. Littmark and S. Fedder, *Nucl. Instrum. Methods* **194**, 607 (1982).

[82] M. Vicanek and H. Urbassek, *Nucl. Instrum. Meth. B* **B48**, 549 (1990).

[83] T. Michely, M. Kalff, G. Comsa, M. Strobel, and K.-H. Heinig, *J. Phys: Condens. Mat.* **14**, 4177 .

[84] U. Valbusa, C. Boragno, and F. Buatier de Mongeot, *J. Phys: Condens. Mat.* **14**, 8153 (2002).

[85] F. Everts, H. Wormeester, and B. Poelsema, *Phys. Rev. B* **82**, 081415 (2010).

[86] F. Rabbering, H. Wormeester, F. Everts, and B. Poelsema, *Phys. Rev. B* **79**, 075402 (2009).

[87] L. Jorritsma, M. Bijnagte, G. Rosenfeld, and B. Poelsema, *Phys. Rev. Lett.* **78**, 911 (1997).

[88] P. Stoltze, *J. Phys: Condens. Mat.* **6**, 9495 (1994).

[89] S. Donnelly, *Radiat. Eff.* **90**, 1 (1985).

[90] B. Terreault, G. Ross, R. G. St.-Jacques, and G. Veilleux, *J. Appl. Phys.* **51**, 1491 (1980).

[91] W. Primak and L. J., *J. Appl. Phys.* **37**, 2287 (1966).

[92] R. Yadava, *J. Nucl. Mater.* **98**, 47 (1981).

[93] W. Jager, R. Manzke, H. Trinkaus, G. Crecelius, R. Zeller, J. Fink, and H. Bay, *J. Nucl. Mater.* **111-112**, 674 (1982).

[94] J. Laakmann, P. Jung, and W. Uelhoff, *Acta Metallurgica* **35**, 2063 (1987).

[95] H. Rajainmaki, S. Linderoth, H. Hansen, R. Nieminen, and M. Bentzon, *Phys. Rev. B* **38**, 1087 (1988).

[96] G. Greenwood, A. Foreman, and D. Rimmer, *J. Nucl. Mater.* **4**, 305 (1959).

[97] J. Evans, *J. Nucl. Mater.* **76-77**, 228 (1978).

[98] J. Evans, *J. Nucl. Mater.* **68**, 129 (1977).

[99] J. Hurly and J. Mehl, *J. Res. Natl. Inst. Stan.* **112**, 75 (2007).

[100] G. Garberoglio, M. Moldover, and A. Harvey, *J. Res. Natl. Inst. Stan.* **116**, 729 (2011).

[101] J. Rowlinson, *Mol. Phys.* **7**, 349 (1964).

[102] G. Hlawacek, V. Veligura, R. van Gastel, and B. Poelsema, *J. Vac. Sci. Technol. B* **32** (2014).

[103] S. Ogawa, T. Iijima, S. Awata, R. Sugie, N. Kawasaki, and Y. Ot-suka, *Microsc. Microanal.* **18**, 814 (2012).

[104] H. Hersh, *Phys. Rev.* **148**, 928 (1966).

[105] H. Pick, *Il Nuovo Cimento* **7**, 498 (1958).

[106] J. J. Markham, *F-Centers in Alkali Halides*, Academic Press, 1966.

[107] D. Pooley, *Proc. Phys. Soc.* **87**, 245 (1966).

[108] C. R. A. Catlow, K. M. Diller, and L. W. Hobbs, *Philos. Mag. A* **42**, 123 (1980).

[109] A. Onaka, I. Fujita, and A. Fukuda, *J. Phys. Soc. Jpn* **18**, 263 (1963).

[110] T. Castner and W. Känzig, *J. Phys. Chem. Sol.* **3**, 178 (1957).

[111] V. Puchin, A. Shluger, and N. Itoh, *Phys. Rev. B* **52**, 6254 (1995).

[112] A. Shluger and K. Tanimura, *Phys. Rev. B* **61**, 5392 (2000).

[113] M. Kabler, *Phys. Rev.* **136**, A1296 (1964).

[114] R. Murray and F. Keller, *Phys. Rev.* **137**, A942 (1965).

[115] M. Aguilar, P. Chandler, and P. Townsends, *Radiation Effects* **40**, 1 (1979).

[116] P. Townsend, *Rep. Prog. Phys.* **50**, 501 (1987).

[117] A. Bazhin, E. Rausch, and E. Thomas, *Phys. Rev. B* **14**, 2583 (1976).

[118] M. Suchańska, A. Bazhin, and E. Konopelko, *Phys. Status Solidi B* **182**, 231 (1994).

[119] T. Ukai, N. Matsunami, K. Morita, and N. Itoh, *Phys. Lett. A* **56**, 127 (1976).

[120] Y. Kawaguchi, M. Dawes, S. Langford, and J. Dickinson, *J. Appl. Phys.* **89**, 2370 (2001).

[121] P. Chandler and P. Townsend, *Rad. Effects* **42**, 65 (1979).

[122] Y. Suzuki, H. Abe, and M. Hirai, *J. Phys. Soc. Jpn.* **61**, 2964 (1992).

[123] K. Song and C. Leung, *Solid State Commun.* **32**, 565 (1979).

[124] K. Soda and N. Itoh, *J. Phys. Soc. Jpn* **50**, 3988 (1981).

[125] B. Gorobets and A. Rogojine, *Luminescent spectra of minerals*, Ed. WIMS, 2002.

[126] R. Webb, L. Jensen, S. Langford, and J. Dickinson, *J. Appl. Phys.* **74**, 2338 (1993).

[127] N. Nesmelov, *Sov. Phys. J.* **22**, 1306 (1979).

[128] T. Timusk, *J. Phys. Chem. Solids* **26**, 849 (1965).

[129] T. Timusk and W. Martienssen, *Phys. Rev.* **128**, 1656 (1962).

[130] Z. Egemberdiev, A. Elango, and S. Zazubovich, *Phys. Status Solidi B* **97**, 449 (1980).

[131] A. Lushchik, C. Lushchik, K. Schwartz, F. Savikhin, E. Shablonin, A. Shugai, and E. Vasilchenko, *Nucl. Instrum. Meth. B* **277**, 40 (2012).

[132] A. Quaranta, F. Gramegna, V. Kravchuk, and C. Scian, *Nucl. Instrum. Meth. B* **266**, 2723 (2008).

[133] R. Williams, K. Song, W. Faust, and C. Leung, *Phys. Rev. B* **33**, 7232 (1986).

[134] C. Lushchik, *Physics of Radiation Effects in Crystals*, Elsevier sci., 1986.

[135] E. Balanzat, S. Bouffard, A. Cassimi, E. Doorhyee, L. Protin, J. Grandin, J. Doualan, and J. Margerie, *Nucl. Instrum. Meth. B* **91**, 134 (1994).

[136] E. Sonder, *J. Physique.* **34**, C9 (1973).

[137] W. Soppe, *J. Phys: Condens. Mat.* **5**, 3519 (1993).

[138] A. Lushchik, C. Lushchik, K. Schwartz, E. Vasilchenko, R. Papaleo, M. Sorokin, A. Volkov, R. Neumann, and C. Trautmann, *Phys. Rev. B* **76**, 054114 (2007).

[139] A. Perez, E. Balanzat, and J. Dural, *Phys. Rev. B* **41**, 3943 (1990).

[140] A. Dauletbekova, A. Akilbekov, M. Zdorovets, A. Vassileva, and D. Akilbekova, *Nucl. Instrum. Meth. B* **268**, 3005 (2010).

[141] K. Schwartz, M. Sorokin, A. Lushchik, C. Lushchik, E. Vasilchenko, R. Papaleo, D. de Souza, A. Volkov, K. Voss, R. Neumann, and C. Trautmann, *Nucl. Instrum. Meth. B* **266**, 2736 (2008).

[142] W. Soppe, H. Donker, A. García Celma, and J. Prij, *J. Nucl. Mater.* **217**, 1 (1994).

[143] M. Panik, *Growth Curve Modeling*, John Wiley & Sons, Inc, 2014.

[144] J. Melngailis, *Nucl. Instrum. Meth. B* **80**, 1271 (1993).

[145] D. Winston, B. M. Cord, B. Ming, D. C. Bell, W. F. DiNatale, L. A. Stern, A. E. Vladar, M. T. Postek, M. K. Mondol, J. K. W. Yang, and K. K. Berggren, *J. Vac. Sci. Technol. B* **27**, 2702 (2009).

[146] C. Sanford, L. Stern, L. Barriss, L. Farkas, M. DiManna, R. Mello, D. Maas, and P. Alkemade, *J. Vac. Sci. Technol. B* **27**, 2660 (2009).

[147] K. Kohama, T. Iijima, M. Hayashida, and S. Ogawa, *J. Vac. Sci. Technol. B* **31**, 031802 (2013).

[148] J. Yang, D. Ferranti, L. Stern, C. Sanford, J. Huang, Z. Ren, L.-C. Qin, and A. Hall, *Nanotechnology* **22**, 285310 (2011).

[149] J. Schindelin, I. Arganda-Carreras, E. Frise, V. Kaynig, M. Longair, T. Pietzsch, S. Preibisch, C. Rueden, S. Saalfeld, B. Schmid, J.-Y. Tinevez, D. White, V. Hartenstein, K. Eliceiri, P. Tomancak, and A. Cardona, *Nat. Methods* **9**, 676 (2012).

[150] D. Winston, J. Ferrera, L. Battistella, A. Vladár, and K. Berggren, *Scanning* **34**, 121 (2012).

[151] T. Chang, *J. Vac. Sci. Technol.* **12**, 1271 (1975).

[152] M. Parikh, *J. Appl. Phys.* **50**, 4371 (1979).

[153] F. Battye, J. Liesegang, R. Leckey, and J. Jenkin, *J. Phys. C Solid State* **7**, L390 (1974).

[154] T. Boutboul, A. Akkerman, A. Breskin, and R. Chechik, *J. Appl. Phys.* **79**, 6714 (1996).

[155] V. Veligura, G. Hlawacek, R. Berkelaar, R. van Gastel, H. Zandvliet, and B. Poelsema, *Beilstein J. Nanotechnol.* **4**, 453 (2013).

[156] G. Hlawacek, I. Ahmad, M. Smithers, and E. Kooij, *Ultramicroscopy* **135**, 89 (2013).

[157] T. Franklin, *Scanning Ionoluminescence Microscopy with a Helium Ion Microscope*, PhD thesis, University of Southampton, 2012.

[158] M. Borgström, M. Verheijen, G. Immink, T. de Smet, and E. Bakkers, *Nanotechnology* **17**, 4010 (2006).

[159] M. Verheijen, R. Algra, M. Borgström, G. Immink, E. Sourty, W. van Enckevort, E. Vlieg, and E. Bakkers, *Nano Lett.* **7**, 3051 (2007).

[160] R. Algra, M. Hocevar, M. Verheijen, I. Zardo, G. Immink, W. van Enckevort, G. Abstreiter, L. Kouwenhoven, E. Vlieg, and E. Bakkers, *Nano Lett.* **11**, 1690 (2011).

[161] T. Sugahara, H. Sato, M. Hao, Y. Naoi, S. Kurai, S. Tottori, K. Yamashita, K. Nishino, L. Romano, and S. Sakai, *Jpn. J. Appl. Phys.* **37**, L398 (1998).

[162] S. Rosner, G. Girolami, H. Marchand, P. Fini, J. Ibbetson, L. Zhao, S. Keller, U. Mishra, S. DenBaars, and J. Speck, *Appl. Phys. Lett.* **74**, 2035 (1999).

[163] M. Reshchikov and M. H., *J. Appl. Phys.* **97**, 061301 (2005).

[164] K. Lee and J. Crawford, *Phys. Rev. B* **19**, 3217 (1979).

[165] C. Jardin, B. Canut, and S. Ramos, *J. Phys. D Appl. Phys.* **29**, 2066 (1996).

[166] D. Nelson and M. Sturge, *Phys. Rev.* **137**, A1117 (1965).

[167] C. Guguschev, J. Gotze, and M. Gobbels, *Am. Mineral.* **95**, 449 (2010).

[168] Z. Liliental-Weber, Y. Chen, S. Ruvimov, and J. Washburn, *Phys. Rev. Lett.* **79**, 2835 (1997).

[169] Y. Chen, T. Takeuchi, H. Amano, I. Akasaki, N. Yamada, Y. Kaneko, and S. Wang, *Appl. Phys. Lett.* **72**, 710 (1998).

[170] N. Cherkashin, N. Bert, Y. Musikhin, S. Novikov, T. Cheng, and C. Foxon, *Semiconductors* **34**, 867 (2000).

[171] H. Cho, J. Lee, G. Yang, and C. Kim, *Appl. Phys. Lett.* **79**, 215 (2001).

[172] W. Lee, H. Lee, S. Park, K. Watanabe, K. Kumagai, T. Yao, J. Chang, and T. Sekiguchi, *J. Cryst. Growth* **351**, 83 (2012).

[173] M. Herrera, A. Cremades, J. Piqueras, M. Stutzmann, and O. Ambacher, *J. Appl. Phys.* **95**, 5305 (2004).

[174] A. Kakanakova-Georgieva, D. Nilsson, X. Trinh, U. Forsberg, N. Son, and E. Janzén, *Appl. Phys. Lett.* **102**, 132113 (2013).

[175] S. Brown, R. Reeves, C. Haase, R. Cheung, C. Kirchner, and M. Kamp, *Appl. Phys. Lett.* **75**, 3285 (1999).

[176] A. Cremades, J. Piqueras, C. Xavier, T. Monteiro, E. Pereira, B. Meyer, D. Hofmann, and S. Fischer, *Mater. Sci. Eng. B* **42**, 230 (1996).

[177] M. Herrera Zaldivar, P. Fernández, and J. Piqueras, *J. Appl. Phys.* **83**, 2796 (1998).

[178] M. Herrera Zaldivar, P. Fernández, and J. Piqueras, *J. Appl. Phys.* **83**, 462 (1998).

[179] P. Weidlich, M. Schnedler, H. Eisele, U. Strauß, R. Dunin-Borkowski, and P. Ebert, *Appl. Phys. Lett.* **103**, 062101 (2013).

[180] L. Pavesi, F. Piazza, A. Rudra, J. Carlin, and M. Ilegems, *Phys. Rev. B* **44**, 9052 (1991).

[181] R. Chanson, A. Martin, M. Avella, J. Jiménez, F. Pommereau, J. Landesman, and A. Rhallabi, *J. Electron. Mater.* **39**, 688 (2010).

[182] V. Vil'kotskii and V. Pivovarov, *J. Appl. Spectrosc.* **19**, 1604 (1973).

[183] T. Zhang, R. Elliman, and G. Carter, *Nucl. Instrum. Methods* **209-210**, 761 (1983).

[184] L. Joulaud, J. Mangeney, N. Chimot, P. Crozat, G. Fishman, and J. Bourgoin, *J. Appl. Phys.* **97**, 063515 (2005).

[185] H. Němec, L. Fekete, F. Kadlec, P. Kužel, M. Martin, J. Mangeney, J. Delagnes, and P. Mounaix, *Phys. Rev. B* **78**, 235206 (2008).

[186] A. Kamarou, W. Wesch, E. Wendler, A. Undisz, and M. Rettenmayr, *Phys. Rev. B* **78**, 054111 (2008).

[187] W. Yu, L. Qu, W. Guo, and X. Peng, *Chem. Mater.* **15**, 2854 (2003).

List of Publications

1. O. Bliznyuk, **V. Veligura**, E.S. Kooij, H.J.W. Zandvliet and B. Poelsema, "Metastable droplets on shallow-grooved hydrophobic surfaces", *Phys. Rev. E* **83**, 041607 (2011).

2. O. Bliznyuk, J.R.T. Seddon, **V. Veligura**, E.S. Kooij, H.J.W. Zandvliet and B. Poelsema, "Directional liquid spreading over chemically defined radial wettability gradients", *ACS Appl. Mater. Interfaces* **4**, 4141–8 (2012).

3. **V. Veligura**, G. Hlawacek, R. van Gastel, H.J.W. Zandvliet and B. Poelsema, "Channeling in helium ion microscopy: Mapping of crystal orientation", *Beilstein J. Nanotechnol.* **3**, 501–506 (2012).

4. G. Hlawacek, **V. Veligura**, S. Lorbek, T.F. Mocking, A. George, R. van Gastel, H.J.W. Zandvliet and B. Poelsema, "Imaging ultra thin layers with helium ion microscopy: Utilizing the channeling contrast mechanism", *Beilstein J. Nanotechnol.* **3**, 507–512 (2012).

5. **V. Veligura**, G. Hlawacek, R. van Gastel, H.J.W. Zandvliet and B. Poelsema, "Het voordeel van UHV in een helium-ionenmicroscoop", *Nevacblad* **51**, 6–9 (2013).

6. **V. Veligura**, G. Hlawacek, R.P. Berkelaar, R. van Gastel, H.J.W. Zandvliet and B. Poelsema, "Digging gold: keV He$^+$ ion interaction with Au", *Beilstein J. Nanotechnol.* **4**, 453–460 (2013).

7. G. Hlawacek, **V. Veligura**, R. van Gastel and B. Poelsema, "Helium ion microscopy", *J. Vac. Sci. Technol.* **32**, (2014)

8. **V. Veligura**, G. Hlawacek, R. van Gastel, H.J.W. Zandvliet and B. Poelsema, "High resolution ionoluminescence study of defect creation and interaction", accepted to *J. Phys. Condens. Mat.*

9. **V. Veligura**, G. Hlawacek, U. Jahn, R. van Gastel, H.J.W. Zandvliet and B. Poelsema, "Creation and physical aspects of luminescent patterns using helium ion microscopy", submitted.

10. **V. Veligura**, G. Hlawacek, R. van Gastel, H.J.W. Zandvliet and B. Poelsema, "Ionoluminescence of semiconductor materials", in preparation.

Acknowledgements

I cannot believe that I am already writing this last part of my thesis! The four years I spent in the Netherlands have passed extremely fast, but I loved my stay here. Although the weather in Holland is usually not welcoming, the country itself is! The path to a complete thesis was not particularly simple, but luckily there were plenty of people who made it easier. Thus, there will be a lot "thanks" on these two pages.

First of all I want to express my gratitude to my promotor Prof. Bene Poelsema. Bene, thank you for replying to my email 5 years ago and giving me an opportunity to do an internship in the Solid State Physics group, and thank you for accepting me as a PhD student later. I appreciate a lot your time you have spent with me discussing the results, your support and guidance.

I also thank Prof. Harold Zandvliet for his encouragement, for the friendly and motivating atmosphere he creates in the group.

Raoul, thank you for welcoming me into the "HIM group". I appreciate your help with preparing the manuscripts and your patience with moving all my *the*s and *a*s into their right positions in sentences. Thank you for the perfectionism with which you do your work.

I cannot fully express my gratitude to my daily supervisor Gregor. You have been always ready to help in any situation both at and outside the university. Thank you for your patience, advices, support and guidance. I have been always amazed by the amount of your ideas, the speed with which your generate them, by the breadth of your knowledge and your attitude towards science and your work. I wish you and your wonderful family all the best.

I would like to thank Stefan and Herbert for their useful comments and remarks during the work discussions, and their good company during lunch time. I am also thankful to the group's secretaries, Rianne and Simone later, for their help with managing all paperwork. Thanks to Herman and Hans for their technical assistance. Zeiss technicians have made a significant contribution to this thesis. Thanks to Ed and Ed, Frank, Bill, Daniel, Stefan and Nico for fighting with "the beast". All your affords have provided enough HIM working time to be able to com-

plete my work. Thanks to David for giving me training at HIM. The cover image was taken during this training!

Thanks a lot to Mark Smithers for the EDX analysis at SEM and other occasional help. I also thank Dr. Uwe Jahn for the collaboration and the help with the cathodoluminescence measurements in Berlin.

I want to thank all former and present colleagues for a pleasing, welcoming atmosphere in the group! I am grateful to all my roommates for the nice company and not complaining about me playing Russian radio. Thanks to Kai for cheering me up, it was never boring in the office with you. Thanks to Robin for his help with the AFM measurements. Thanks to Ali, Chris, Erik, Hairong, Imtiaz, Tijs, Patrick, Pantelis, Rene for a pleasant company and well spent time at different occasions. All the best to all of you! Special thanks to Avijit for your help at the STM student practicum and a lot of nice conversations. Maciej, it was always nice to chat with you. Your knowledge in physics and other disciplines is impressive. Thanks to you and Anna for the enjoyable meetings we had, and I wish your family happiness and health to your coming child!

A lot of thanks to Olesya! You have helped a lot to me, especially in the beginning when I needed it most. I wish your family to grow and be always happy!

Finally, I want to thank my dear friends: Alex, Anna, Atryom, Ida, Kate, Kristina, Maria, Pasha, Tanya. Thank you for staying my friends and supporting me even from a distance of a few thousands kilometers. Thanks to the modern technologies which help to stay always in touch with you! I am very thankful to my parents and grandparents, my sister and all my family for raising me as I am and for believing in me. I always feel your support and am grateful for that! Thank you Daniel for being always with me, taking care of me, for your help and advices. Without you I would have given up somewhere in the beginning, run home, and never finished this work.

Curriculum Vitae

Vasilisa Veligura

Date of Birth: 18$^{\text{th}}$ of July 1987
Place: Uralsk, USSR

Education

2010 − present: PhD candidate at the group of Physics of Interfaces and Nanomaterials, University of Twente. Research topic: *He ion nanoscopy of three-dimensional structures*

2004 − 2010: Master Degree with honors. M. V. Lomonosov Moscow State University, Faculty of Physics, Chair of General Physics and Molecular Electronics. Thesis: *Research of structural and optical properties of biocompatible silicon nanocrystals obtained by mechanical grinding of monocrystalline and porous silicon*

1997 − 2004: Secondary education, Moscow, Russia

Interships

2009: Solid State Physics group, University of Twente, The Neatherlands

Prizes

2013: Student Award at 9$^{\text{th}}$ International Symposium on Atomic Level Characterization, Hawaii, US

2010: R.V. Khokhlov Award for the best scientific student work in 2009-2010 academic year